Czech Technical University In Prague

Faculty of Electrical Engineering

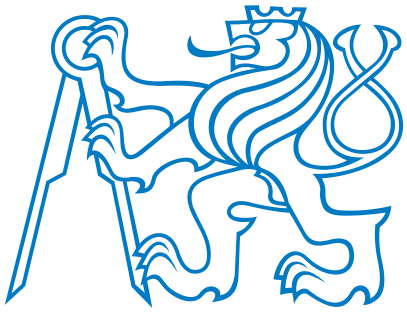

Master Thesis

Spectroscopic High Dose Rate Gamma-Ray Detector

Author:
Marek Hudec

Supervisor:
Antonín Platil

May 11, 2015

Thesis
Abstract

The master thesis studies a possibility of energy spectrum measurement at high dose rates (HD) of gamma radiation in the field of environmental radiation monitoring. Recent disasters and state of the art show lack of preparedness for emergency situations by means of spectrometers (i. e. the possibility of nuclide identification). This work presents a core development of a HD spectrometer for gamma-rays from 30 keV to 3 MeV by carefully selecting the detector's material, size and considering its suitability for long-term monitoring in a temperature range from −40 °C to 60 °C. The small cadmium zinc telluride (CdZnTe) and cerium bromide ($CeBr_3$) detectors selected based on Monte-Carlo simulations in Geant4 yield satisfactory results in terms of their spectrum shape (e. g. Peak-To-Compton ratio), achieved HD limit and temperature stability. The exploited limitations of the detectors, including the electronics and the 16 MHz MCA used, are further analyzed and show a possibility of improvement and achievement of even higher dose rates (>250 mSv h^{-1}).

Keywords: *high dose rate, gamma-ray spectrometer, energy spectrum, environmental radiation monitoring*

Překlad názvu diplomové práce: Spektroskopický detektor gama záření vysokých dávkových příkonů

Anotace: Diplomová práce zkoumá možnosti spektroskopického měření vysokých dávkových příkonů (HD) gama záření pro obor radiačního monitoringu. Nedávné nehody a aktuální stav ve vědě a výzkumu ukazují nedostatečnou připravenost na krizové situace ve smyslu spektrometrické identifikace jednotlivých vyzařujících nuklidů. Tato práce prezentuje vývoj základu HD spektrometru pro gama záření v rozsahu od 30 keV do 3 MeV, který je podložen pečlivým výběrem vhodného detekčního materiálu, velikostí detektoru a bere v potaz nároky na své použití, tj. dlouhodobé monitorování v teplotním rozsahu od −40 °C do 60 °C. Dva typy detektorů malých rozměrů z materiálů CdZnTe a $CeBr_3$, které byly vybrány na základě simulací Monte-Carlo v programu Geant4, poskytují uspokojivé výsledky jak z hlediska výsledného tvaru spektra, tak z hlediska dosažitelných dávkových příkonů a teplotní stability. V práci jsou analyzována dosažená omezení detektorů (včetně použité elektroniky a 16MHz MCA). Z této analýzy vyplývá možnost vylepšení, zejména možnost dosažení ještě vyšších dávkových příkonů (>250 mSv h^{-1}).

Klíčová slova: *vysoký dávkový příkon, spektrometr gama záření, energetické spektrum, monitorování radiace*

Thesis
Acknowledgement

I would like to express my deepest gratitude to my supervisor, Antonín Platil, for his support and to Sascha Reinhardt from the company ENVINET GmbH for guidance throughout the research. I would also like to extend my appreciation to the the whole team of ENVINET, who provided me the very interesting topic and assistance and support of my experiments with the presented detectors. My sincere appreciation is extended to the company Ritec from Latvia, especially to Mr. Victor Ivanov, who provided two detectors for testing purposes free of charge. I would also like to extend my deepest gratitude to my family. Without their encouragement, I would not have a chance to be at my alma mater, the Czech Technical University in Prague.

Thesis
Declaration

I declare that the work presented here is, to the best of my knowledge and belief, original and the result of my own investigations, except as acknowledged. Formulations and ideas taken from other sources are cited as such.

Prague
May 11, 2015

Marek Hudec

Thesis
Contents

Chapter 1
Introduction

The thesis studies a possibility of spectroscopic measurement of high gamma dose rates (HD). The study is especially focused on long-term measurement with gamma-ray detectors usually deployed within nationwide or local monitoring networks for in-situ environmental monitoring. The complete motivation for this topic is presented in detail in chapter 2, where lack of HD spectrometers suitable for environmental monitoring is emphasized. Presented plots of measurements recorded after recent nuclear disasters in Chernobyl and Fukushima are presented as an alerting fact further supporting the motivation of developing a spectrometer capable of measuring dose rates of up to hundreds of $\mathrm{mSv\,h^{-1}}$ (in a H*(10) norm as defined in section 2.3).

For the purpose of HD spectroscopy, a development based on elementary physical understanding of interaction of gamma-rays with matter has to be done. The theoretical background is summarized in chapter 3. The thesis focuses only on the three elementary interaction mechanisms and confronts them with the size of a detector (section 3.2.4.1) and the quality of an energy spectrum (section 3.2.4). The different interaction mechanisms, mostly the Compton scattering, pose a limitation in terms of spectrum quality and make the peak corresponding to the correct gamma-emission energy small in comparison to the area of the scattered particles. Moreover, the development of the detector takes following restrictions into account: low temperature dependence (spectrum drift, expansion/shrinkage), operating temperature from $-40\,^{\circ}\mathrm{C}$ to $60\,^{\circ}\mathrm{C}$, no cooling, resolution not worse than NaI(Tl) and the already-mentioned quality of the spectrum in the range of 30 keV to 3 MeV in terms of Peak-To-Compton ratio (as well as other parameters defined in section 3.8), sufficient for quantitative nuclide-specific analysis. The application of environmental monitoring requires special material properties including long-term stability (over 10 years), robustness and insensitivity with regard to mechanical vibration and shocks. The complete detector based on the core studied in this thesis shall be maintenance free and have low power consumption (important for battery powered applications). Two groups of solutions were found to be suitable, one with scintillators and the other with semiconductors.

Taking all the listed parameters into account, a search for the best solution considering material and electrical properties was conducted and presented in chapter 4. This task took the most important parameters with regards to HD spectroscopy into consideration: the material speed in terms fall and rise times of the output electrical pulses and the standard resolution obtained with the material. The material speed shall be maximized in order to prevent saturation of the detector at high dose rates (resulting in high count rates). The saturation happens in the electrical output signal of the detector, where individual pulses overlap each other and cause inability to recognize their individual amplitudes. The amplitudes are important for spectroscopy, since they carry information about the incident gamma-ray energy. Fast materials suitable for this work include some of the new inorganic scintillation materials like $LaBr_3$, $CeBr_3$ (section 4.1.2) and room-temperature semiconductors presented by standard detector materials CdTe and CdZnTe (CZT) in section 4.3.2.

A number of Monte-Carlo simulations using the software package Geant4 were done in order to select the best material and size of the detector (chapter 5). The raw output was then convolved using standard peak shape analytic functions dependent on the electronics and material properties (e. g. charge trapping in CdZnTe) and compared to real measurements.

Based on the mentioned chapters, the final selection of a solution suitable for the HD spectrometer was made. Two types were selected, one semiconductor (CdZnTe) and one scintillator ($CeBr_3$). A more detailed discussion about the aspects of selection as well as detectors available on the market is provided in chapter 6. The same chapter also deals with the development from a practical point of view, describing the used electronics including the multi-channel analyzer and preamplifiers. In order to test the detectors performance, measurements in a radiation chamber in Munich (Helmholtz Zentrum facility) and tests in a climatic chamber were done. The experiment setup and procedure is also summarized in the same chapter, particularly in sections 6.6 and 6.7.

The results of measurements made are presented in the last chapter 7. The chapter focuses on the measurements at high doses, presenting spectra containing pile-up effects, peak shifts, peak extension and other phenomena occurring at high dose rates (results from high dose rate tests are presented in section 7.2). The results also consider count rate corrections needed due to MCA speed limitations. For the purpose of HD tests, a cesium source was used. Other sources (cobalt, europium) were used as well in order to compare detectors at low dose rates (section 7.5). The different types of detectors result in different shapes of peaks, which had to be fitted with an analytic function in order to calculate the peaks area, resolution and other properties. The peak shape fitting comprises three models listed in section 7.1.1. The outcome of temperature tests are presented in section 7.3, where results are presented as well as compared to other publications and similar studies. Short note on background and intrinsic self-activity of detectors is made in section 7.4.

The thesis presents a core development of a HD spectrometer and mentions several issues that can be encountered during such development. The limitations of electronics as well as detector material properties are discussed throughout the thesis and can be used for further development and study of the high dose gamma-ray spectroscopic detector.

Chapter 2
Motivation

2.1 Introduction to gamma spectrometry

Before starting detailed discussions regarding the thesis motivation and achievable goals, a small number of comments has to be made so that the reader is familiar with terminology used throughout the text and a misunderstanding is avoided. The presented thesis will study the area of gamma radiation monitoring. The term monitoring does not mean the same as its detection. Monitoring is rather a long-term detection, where stability is required on the first place. Gamma radiation, which originates in gamma emissions during radioactive decay of radioactive nuclides, can be detected using various methods based on physical understanding of its properties and interaction with matter. This interaction usually takes place in a detector made of a special material. The main purpose of such detector is to convert incident radiation into an electrical signal.

Since spectroscopic detector is sought, this electrical signal has to be qualitatively analyzed and as a result, an energy spectrum of the measured gamma radiation is provided. The energy spectrum is the intensity of detected gamma radiation (vertical scale) at individual energies (horizontal scale). Spectrometers are never ideal devices, they are not able to measure intensity of the incident radiation and they only measure the detected part of it – therefore a calibration is needed. Moreover, ideal spectrometers would provide perfect energy resolution – an ideal spectrum would contain infinitely thin peaks of incident gamma rays, which are due to quantum physics exactly emitted at a specific energy. However, real spectrometers experience a large number of imperfections and thus, an application-dependent compromise has to be considered. The same has to be done for the purpose of measuring at high radiation fluxes for which motivation is provided in the following text.

2.2 Environmental radiation monitoring

The main application of the spectroscopic high dose rate detector to be developed is environmental radiation monitoring. Recent disasters where dose rate safety limits were broken on several different sites showed lack of preparedness for such situations. Spectrometers currently used for monitoring (monitoring rings around nuclear power plants, nationwide networks, water probes, etc.) cannot cope with high dose rates. Simple counters are used instead, preventing sophisticated algorithms and protection planning systems from their proper deployment. The information about nuclide vectors present in environment is vital for calculating and projecting future behavior and development of a radioactive release (cloud of decaying nuclides with different half-life) in such an emergency situation. Planning methods based on this information can only then prevent vast impacts on areas close to nuclear reactors or other sites handling radioactive materials where such a disaster can happen.

Currently there are 438 reactors operated in more than 30 countries around the world (see figures 2.1, 2.2), according to International Atomic Energy Agency (IAEA) in its *Power Reactor Information System* (PRIS). Another 71 are being built, whereas 149 are already out-of-service and in a permanent shutdown mode. All these sites have to be monitored and prepared for an emergency situation. The task of the environmental monitoring is to protect environment, in which safety and human protection is the top priority. It is thus intolerable to discard and/or not use the information about spectrum, when it could actually be measured and included in the recognition of nuclides, their decay chain and half-time in order to evacuate humans or prevent the worst case scenarios.

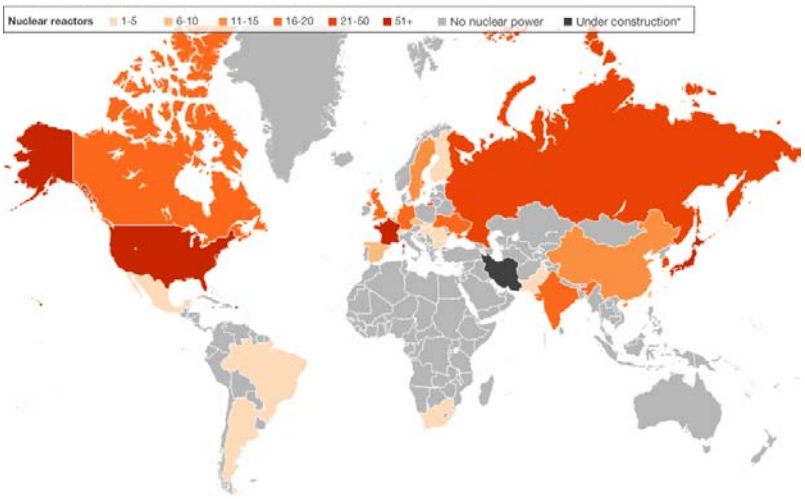

Figure 2.1: Operating reactors worldwide in 2011, data from IAEA PRIS [1] (*Under construction only represents countries currently building nuclear power plants that previously had none).

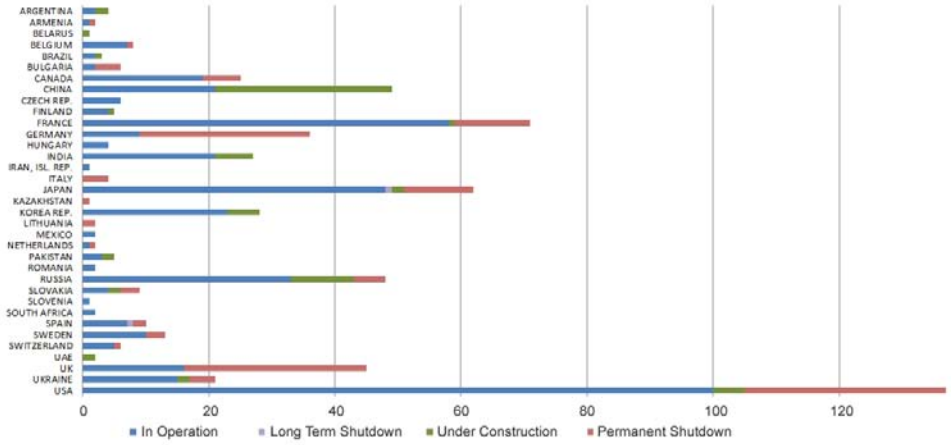

Figure 2.2: Number of reactors by country and status (2014), taken from IAEA PRIS [1].

2.3 Biological impact of ionizing radiation

The absorbed dose of radiation can be expressed in two different ways. The first is as a physical quantity – an integral of absorbed incident radiation over time D, expressed in Grays ($1\,\mathrm{Gy} = 1\,\mathrm{J\,kg^{-1}}$). Due to the fact that biological impact of such absorbed dose strongly depends on the radiation properties, another way of expressing the absorbed dose is by its biological impact on tissues, because of the fact that the same dose in Grays can lead to different biological effects. The quantity is usually called dose equivalent and it is actually an energy-scaled physical absorbed dose. It can be calculated as a weighted sum of the physical absorbed dose D, weighted by a factor $w(E)$, which depends on the energy E,

$$H = \mathbf{W} \cdot \mathbf{D} = \sum_{i=1}^{n} w(E_i) D_{E_i}, \tag{2.1}$$

where $\mathbf{W}$ is a vector of weights $w(E_i)$ at energies E_i and $\mathbf{D}$ a vector absorbed dose at these energies, D_{E_i}. The equivalent dose H is expressed in Sievert ($1\,\mathrm{Sv} = 1\,\mathrm{J\,kg^{-1}}$). Equivalent dose rate is then the equivalent dose absorbed per unit time, mostly expressed in Sv/h.

Choice of the biological impact factor $\mathbf{W}$ is dependent on a convention. These are published and maintained by ICRP (International Commission on Radiological Protection). The most important standard for environmental monitoring is a quantity called *ambient dose rate equivalent*, defined by ICRP as:

The ambient dose equivalent, H(10), at a point of interest in the real radiation field, is the dose equivalent that would be produced by the corresponding aligned and expanded radiation field, in the ICRU sphere at a depth of 10 mm, on the radius vector opposing the direction of radiation incidence.* [34]

In other words, the ICRP defines it as dose rate equivalent related to radiation absorbed in tissue at 10 mm depth.

The standard usually provides manufacturers way (in form of tables or lists of factors) to calculate dose rate equivalents from incident radiations. Typically, fluence-to-dose rate (fluence is the incoming radiation flux per unit time) conversion factors are provided. This dependence for H*(10) is shown in figure 2.3. From now on, the H*(10) convention will only be used throughout the text, whenever mentioning dose or dose rate.

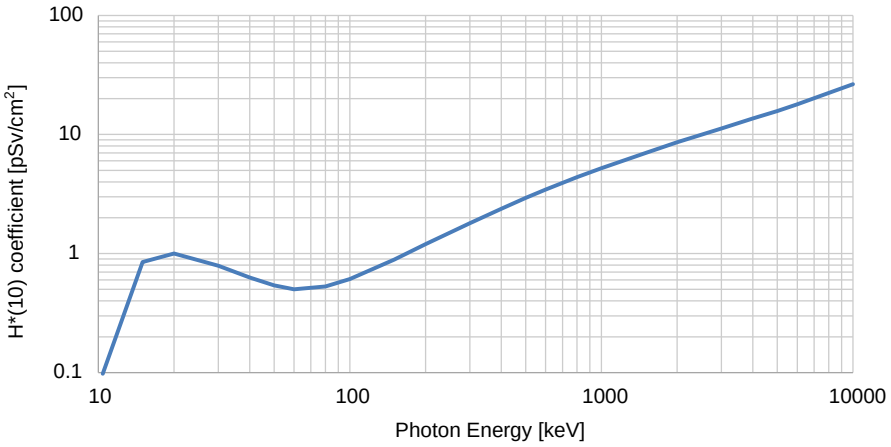

Figure 2.3: Conversion coefficients for the calculation of equivalent dose based on the incident gamma radiation fluence. Please note the logarithmic scale on both axes. The data were taken from ICRP [33].

When a tissue is exposed to radiation, the biological impact is summarized by the total equivalent dose (accumulated over time). The higher the equivalent dose, the more severe the impact is. A graphical representation of the dosage causes and effects are shown in figure 2.4.

2.4 Recent disasters

Recent disasters in Fukushima (2011) and Chernobyl (1986) clearly demonstrate the need of such a new detector, considering the fact that current spectrometers cannot cope with dose rates over 1 $\mathrm{mSv\,h^{-1}}$ (see a list y available solutions in section 2.5). Picture 2.5 shows a situation after the disaster in Chernobyl, on the first sight it is evident that currently available spectrometers do not suffice. As a second example, Fukushima measurements of dose rate over time on several different locations (as marked in a map shown in figure 2.6) are plotted in figure 2.6. It is important to realize that such extremely high spectrometric-unidentifiable dose rates were measured over a long-time period, slowly decaying over a range of days. This is a strongly motivating fact for the research and must be taken into consideration and improvement of protection of areas with such potential risks. Moreover from a political and ethical point of view, the question of whether to keep using nuclear reactors as a source for energy for mankind has risen attention and has lately been a hot topic across developed countries.

The development of a spectroscopic detector capable of high dose rate measurement is motivated by several facts. As already noted, one of them is the need of such detector for environmental monitoring. Another fact is the current state of science and the commercial market, where lack of such technology is apparent. All this gives rise to a great challenge of developing a detector for spectroscopy under high radiation fluxes of up to 1 $\mathrm{Sv\,h^{-1}}$ (equivalent dose rate H*(10)).

Before proposing a solution with all technical aspects and details, current state of the art on one hand and market situation on the other will be provided with emphasis on limitations and availability of a solution.

2.5 Current state of the art

Detection techniques of high dose rate pose a great challenge in general. Quantum physics behind the techniques is the main limiting factor for the whole problem. In order to measure high doses and not to "saturate" the measuring medium (where interaction of the radiation with matter takes place and is actually detected), the medium has to be of small size. Many papers deal with high flux measurements of X- or Gamma-Rays (mostly in astronomical and medical applications), but only few mention measuring of spectra under such conditions ([17], [37]).

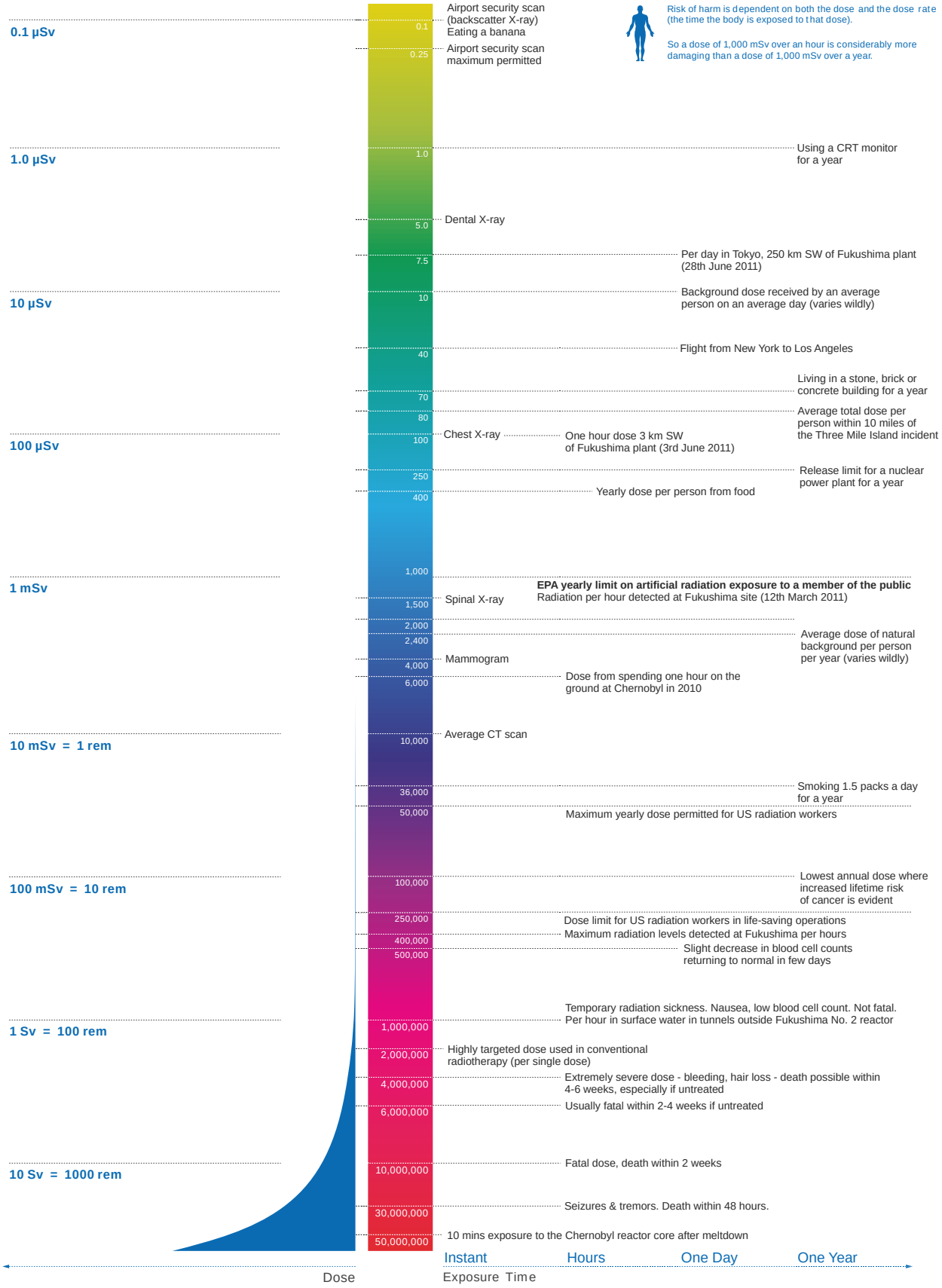

Figure 2.4: Radiation dosage chart displaying effects of the equivalent absorbed dose. The dose is shown in a logarithmic scale, the doses shown are averages. Data table is available online [www.bit.ly/RadiationChart] and its sources are BBC, Guardian Datablog, Mayo Clinic, XKCD.

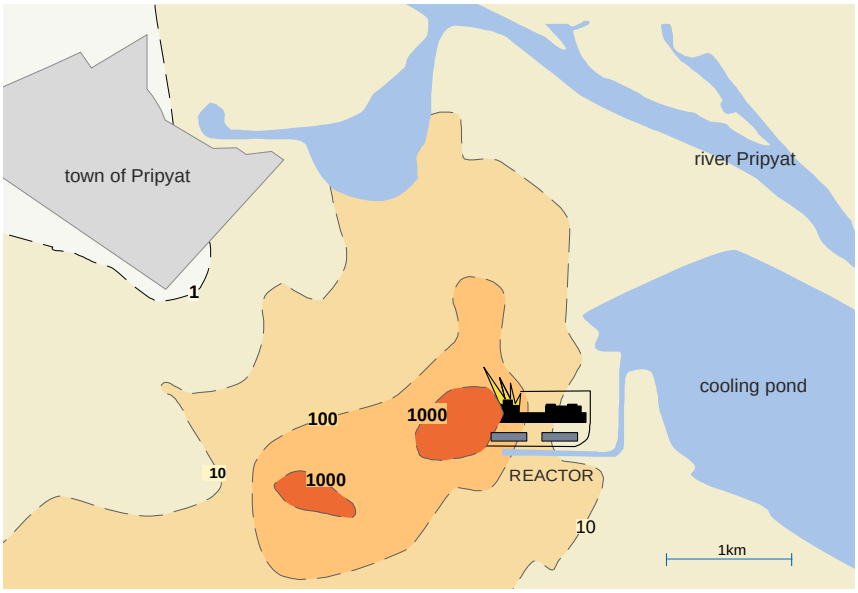

Figure 2.5: Measured dose rates in air around Chernobyl on 26 April 1986 in mSv h^{-1}, taken from [4].

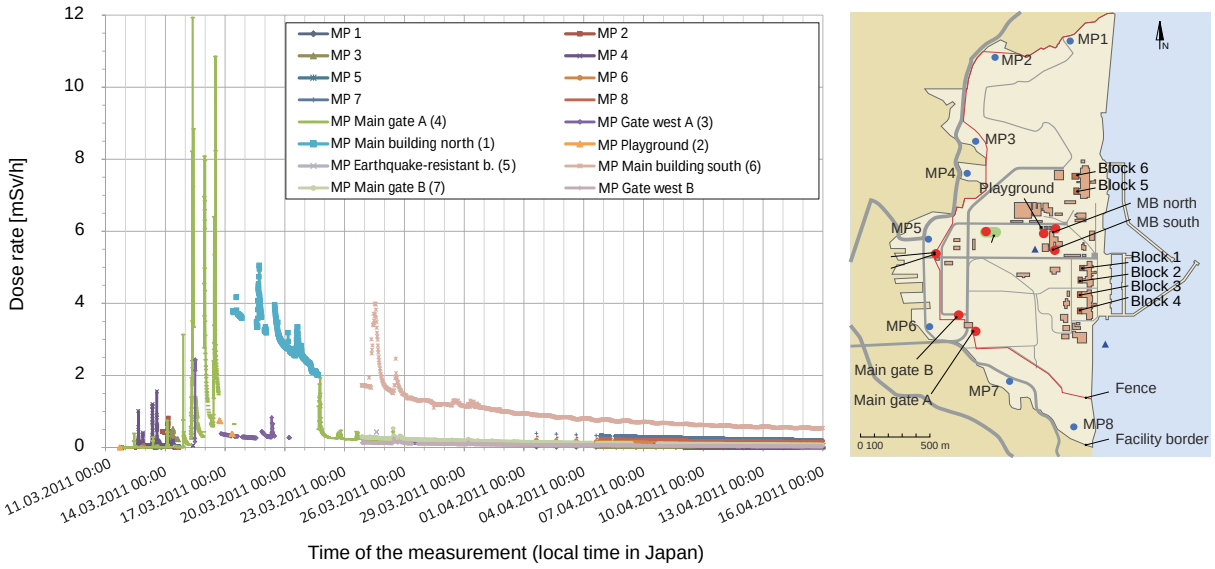

Figure 2.6: Measured dose rates in air around Fukushima (different measurement points (MPs)) between 11 March and 16 April 2011 in µSv h^{-1}, taken from [15].

Currently, sufficiently small detectors are available on the market, but they rarely provide spectroscopic information. And when they do, the radiation flux is of rather lower intensity than the goal of this thesis. The top-range products in this category of spectrometers found from various suppliers all over the world were limited by maximum dose rates of several mSv h^{-1}. Others, mostly oriented for science purposes, use collimators to achieve a similar range (e. g. with high purity germanium detectors (HPGe) [40] or silicon-drift detectors (SDD) in astronomy).

Commercially available products for spectroscopic monitoring are for example *FLIR RadHunter* (utilizing NaI(Tl) with 10 µSv h^{-1}), *Envinet SARA* (NaI(Tl) 100 µSv h^{-1} or LaBr3(Ce) with 400 µSv h^{-1}), *Polimaster PM1410* (NaI(Tl) with 900 µSv h^{-1}), *RadCom MSpec* (CsI(Na) 10 mSv h^{-1}) and *Kromek GR05* (CdZnTe with 8 mSv h^{-1}). Out of these, most of the devices are hand-held and not meant for long-term environmental monitoring. A special attention deserves the MSpec with a 1/2-inch crystal, smaller than crystals used in the other listed devices. Some of the typical monitoring devices are shown in figure 2.7.

Other small detectors can measure up to 10 Sv h^{-1}, but they do not measure and provide spectra. This is simply because the spectroscopic information is lost either by filtering the output of the detector or by the nature of measuring the incident radiation. The incident radiation produces too many pulses

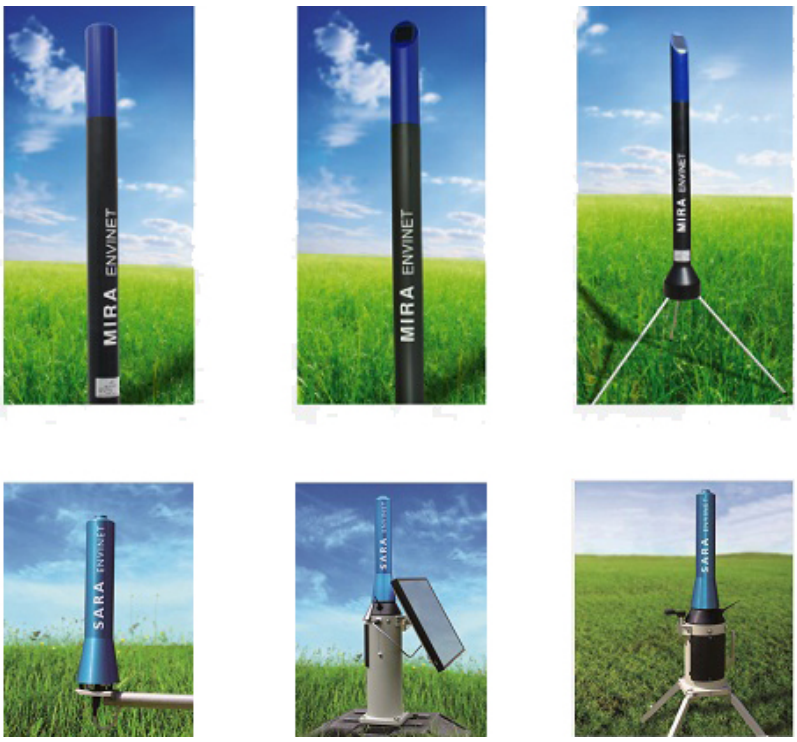

Figure 2.7: *Envinet* MIRA (upper images) for gamma dose rate measurement and *Envinet* SARA (bottom) for spectroscopy, taken from `www.envinet.com`.

and when these are filtered (more accurately integrated by low-pass filters), slow and relatively cheap filtering electronics suffices for translating the integrated signal into information about the flux. For non-spectroscopic measurements usually *Geiger-Müller tubes* (GM) are used. The available finished products are for example *Polimaster PM1610B / B-01* (up to $10\,\mathrm{Sv\,h^{-1}}$), *Envinet MIRA* (up to 10 Sv/h). Proportional counters include solutions with ionization chambers, e. g. *LB 6701 from Berthold* (with up to 1000 Sv/h). Scintillator materials and semiconductors are used as well, but in all the three cases the spectroscopic information is lost by the nature of processing the raw signal. Products that fit into this category are for example *Canberra STHF-R* (Si detector, $1000\,\mathrm{Sv\,h^{-1}}$). The use of scintillators in non-spectroscopic monitoring is rare due to its higher cost compared to GM tubes.

Another class are Germanium detectors. Such solutions always come with cryogenic cooling (to be described in part 4.3.1) and are difficult to maintain. Portable monitors with Ge detectors are offered on the market by several manufacturers, e. g. *ORTEC, Radtech, Baltic Instruments* and others. The standard maximal dose rate for such detectors is in order of hundreds of $\mu\mathrm{Sv\,h^{-1}}$.

There is a special class called *Silicon Drift Detectors* (SDDs), not suitable for measuring in the whole energy range (suitable for X-Rays only) and other detectors like Si, which are suitable for high fluxes, but again require cooling.

2.6 Spectroscopy at high doses

As already shown above by the current state of the market, such detectors are very hard to get and the upper limit of commercially available products is around several $\mathrm{mSv\,h^{-1}}$. The challenge of achieving high-flux capability results not only in small detector sizes, degrading the spectrum (as described in 3.2.4), but also the requirement of fast readout and prompt calculations. The limits are therefore given by the medium's material speed (due to the time scale of the involved physical processes), the electronics used in order to process pulses coming from it and the medium size itself.

Several articles examine the area of high flux measurements. Design of a complex system with two scintillation media proposes use of a special Compton suppression technique to reduce small-size effects of the medium [17]. Another paper studies scintillator response and develops a method to resolve multiple pulses piling up over each other [92], count rates of more than 1 MHz are reported as achievable. Today, fully digital acquisition is preferred over the analog. It can achieve higher speeds and overall a better performance [20]. The transition to digital techniques came with the boom of transistor technology. Furthermore, modern FPGAs are frequently used as fast alternatives to standard processors [13].

More papers on the topic of high flux detectors are published in the area of X-Ray detectors used in astronomy and for medical applications. The higher fluxes are usually obtained with help of attenuators or collimators, which serve as attenuators of the flux intensity. This is however a non-trivial task due to the collimators energy sensitivity and production of scattered photons at higher rates. Pixel detectors (2D imaging) are very popular with the use of CdZnTe (CZT) material. A similar material CdTe is used for the same applications [14]. It was shown that these detectors can cope with count rates of up to $15\,\mathrm{MHz\,mm^{-2}}$ [84].

No publications were found in the area of the thesis assignment. Unfortunately, all papers found either contribute to the topic only partially (by studying one part of the whole measurement chain) or provide cost-ineffective bulky solutions (large cooling systems, several detection techniques combined, etc.) not applicable in the field of environmental monitoring.

Chapter 3
Detection techniques

Detection principles of all available radiation detectors are based on underlying quantum physics of ionizing radiation interacting with matter. In the following text, gamma rays will be assumed as the only incoming radiation. Other types will not be studied for now as they are not relevant for the thesis.

3.1 Gamma rays in question

Gamma rays can come from various sources, from which the most important for our application is radioactive decay of a nuclide. Other sources include annihilation, nuclear reactions and bremsstrahlung [43]. The gamma rays coming from gamma decays are emitted at an exact single one energy having a precisely determined frequency (=energy). This energy directly depends on the measured nuclide. One nuclide can undergo several emissions during its decay and thus produce more lines in the spectrum. In table 3.1 the most important nuclides according to ANSI N42.34 standard [78] are listed. These include radioactive materials used in industrial applications, medical applications, special (including environmental monitoring) and normally occurring radioactive material (NORM). The nuclides including their daughters are plotted in figure 3.1. Following phenomenon can be observed: from all the important nuclides, every nuclide lies either under 1.5 MeV or it has an important peak of its decay component located at lower energies. Thus, for nuclide identification the range up to 1.5 MeV shall be sufficient (assuming the nuclides listed in table 3.1). This observation is quite important for the upcoming chapters of this thesis.

Special nuclear materials:	^{233}U, ^{235}U, ^{237}Np, Pu (all nuclides)
NORM:	^{40}K, ^{226}Ra, ^{232}Th, ^{238}U
Industrial radionuclides:	^{57}Co, ^{60}Co, ^{133}Ba, ^{137}Cs, ^{192}Ir, ^{204}Tl, ^{226}Ra, ^{241}Am
Medical radionuclides:	^{18}F, ^{67}Ga, ^{51}Cr, ^{75}Se, ^{89}Sr, ^{99}Mo, ^{99m}Te, ^{103}Pd, ^{111}In, ^{123}I, ^{125}I, ^{131}I, ^{153}Sm, ^{201}Tl, ^{133}Xe

Table 3.1: List of important nuclides (should not be considered all-inclusive) from ANSI standard [78].

3.2 Interaction of particles with matter

For gamma rays incident on a detection medium and interacting through it, several interaction possibilities exist. The quantum phenomena behind determine the type of interaction and the probability of this interaction type is given by many parameters. From these parameters, the most dominant is the energy of the incident radiation. A short review of the underlying quantum theory will now be presented in the following sections. This basic theory was taken from a standard literature on the topic of gamma radiation detection like [43].

There are many interaction mechanisms known, but only three play a significant role in the range of energies between 30 keV and 3 MeV. These are *photoelectric absorption, Compton scattering* and *pair production*. In all three cases, the interaction results in either partial or full deposit of energy of the incident photon. In the following text, these three main interaction mechanisms of gamma rays within the detecting medium will be discussed. The ratio between the probabilities of interaction can be seen in a plot of absorption coefficients of $CeBr_3$ and CdTe materials (figure 3.6), as these were found to be top candidates for the detector to be designed.

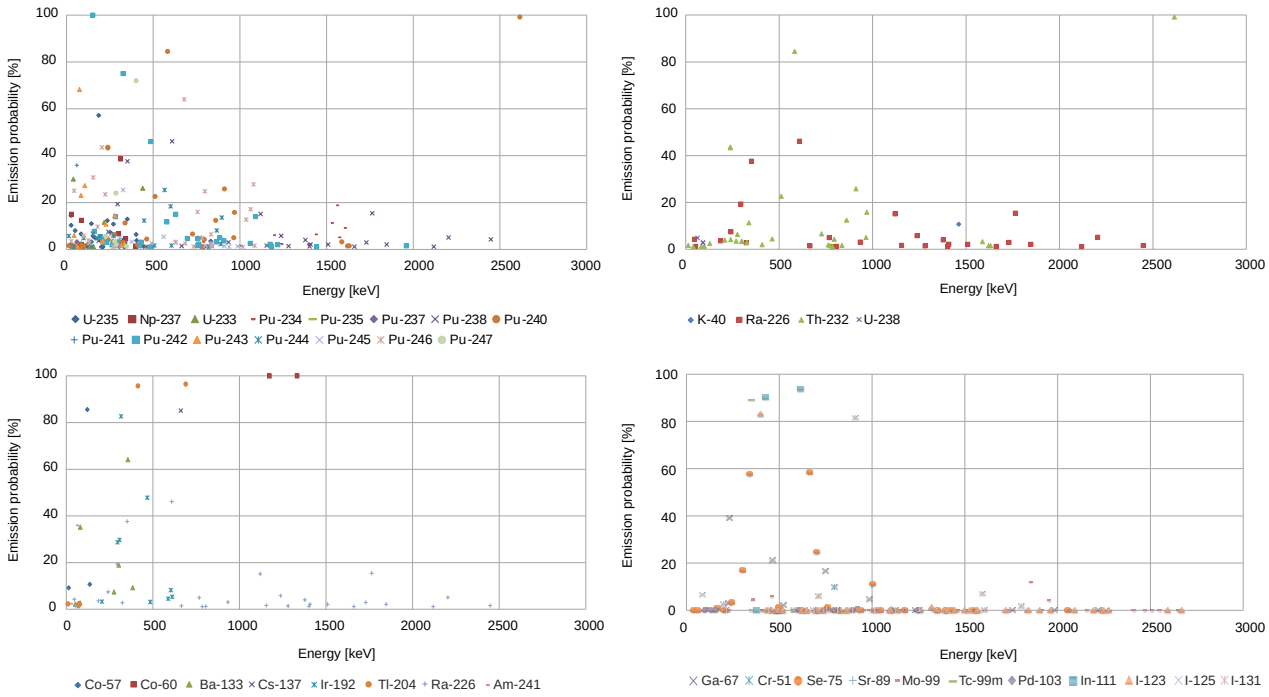

Figure 3.1: Nuclides scope of the detector to be developed. There are four important categories: special nuclear materials with its daughters (top left), NORM nuclides with its daughters (top right), industrial nuclides with its daughters (bottom left) and medical nuclides with its daughters (bottom right).

3.2.1 Photoelectric absorption

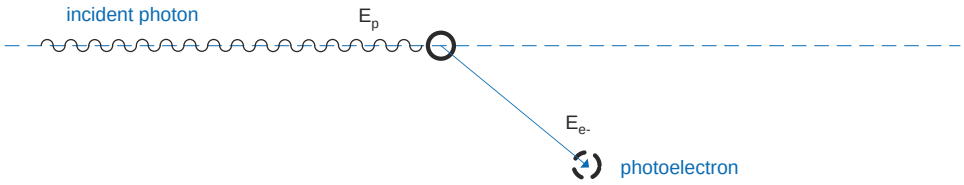

Figure 3.2: Schematic illustration of photoelectric absorption.

The photoelectric effect for an incident photon of an energy E_p results in a produced photoelectron in the material and the incident original photon is completely absorbed (figure 3.2). The generated electron fully carries the energy of the incident photon,

$$E_{e-} = E_p - E_b = h\nu - E_b, \tag{3.1}$$

where h denotes the Planck's constant and ν the frequency of the incident photon. The energy E_b is a binding energy of the electron that became the so-called *photoelectron*. For gamma rays with energies over a few hundreds of keV, the binding energy becomes negligible and the photoelectron energy is almost that of the incident photon. But as the energy of incident radiation increases, so does the probability that different mechanisms of interaction apply (scattering, pair production).

3.2.2 Compton scattering

When an incident photon undergoes the interaction called Compton scattering, the incident photon does not get absorbed completely. The incident particle undergoes an interaction with an electron in the medium and then it is deflected in an angle that by its probability depends on the particle's energy. The so-called *recoil electron* in the material receives part of the photon's energy and this electron then carries energy deposited in the material by the incident photon. The deflected photon, so-called *scattered photon*, with a lower than its original energy might then interact again or escape the medium.

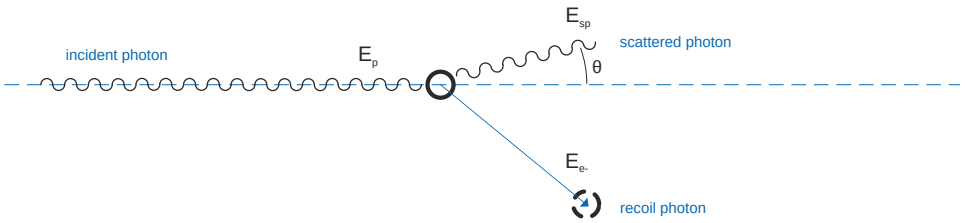

Figure 3.3: Schematic illustration of Compton scattering.

The interaction through Compton scattering is illustrated in figure 3.3, where $E_p = h\nu$ is the energy of the incoming gamma ray and $E_{sp} = h\nu'$ is an energy of the scattered photon, described by the formula incorporating the original energy and the angle of interaction θ,

$$E_{sp} = h\nu' = \frac{h\nu}{1 + \frac{h\nu}{m_0 c^2}(1 - \cos\theta)}, \tag{3.2}$$

where

$$m_0 c^2 = 0.511\,\mathrm{MeV} \tag{3.3}$$

is the rest mass energy of electron. When substituting small values for θ, one can immediately see the denominator goes to one and therefore for small angles, the energy of the scattered photon is approximately the same as that of the incoming gamma ray. The other extreme case is when substituting $\theta = \pi$, when the photon is so-called back-scattered. The energy deposited in the recoil electron is maximal, whereas the scattered photon leaves the interaction with minimal, but non-zero energy.

The probability of back-scattered photons is different from the probability for small deflections. This angular distribution ($\frac{\mathrm{d}\sigma}{\mathrm{d}\Omega}$ denotes the differential scattering cross section) is described by the Klein-Nishina formula,

$$\frac{\mathrm{d}\sigma}{\mathrm{d}\Omega} = Z r_0^2 \left(\frac{1}{1 + \alpha(1 - \cos\theta)}\right)\left(\frac{1 + \cos^2\theta}{2}\right)\left(1 + \frac{\alpha^2 (1 - \cos\theta)^2}{(1 - \cos^2\theta)(1 + \alpha(1 - \cos\theta))}\right) \tag{3.4}$$

with

$$\alpha = \frac{h\nu}{m_0 c^2}. \tag{3.5}$$

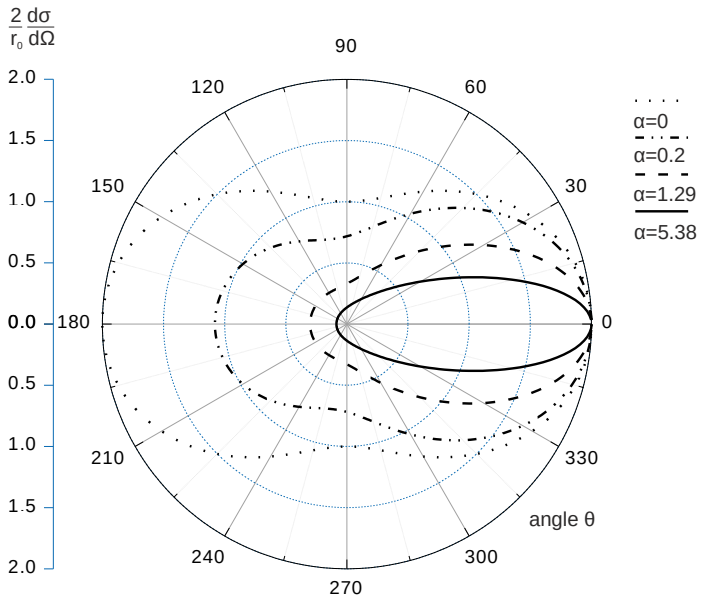

Figure 3.4: Angular distribution of scattered photons according to the Klein-Nishina formula (3.4).

For illustration, a simple plot of angle dependence on the energy is provided in 3.4. The higher the energy of the incident gamma rays, the higher is the probability of forward scattering (small angles θ). The formula shows a direct dependence on atomic number Z and electron radius r_0^2.

The energy of the recoil electron is then simply the rest

$$E_{e-} = E_p - E_{sp}. \tag{3.6}$$

3.2.3 Pair production

Probability that an incident particle results in pair production is strictly zero for low energies. The limit is posed by the fact that in order to generate a pair, a minimum energy of twice the rest-mass energy of an electron is needed (1.02 MeV). The probability is then higher with increasing energy of the incoming gamma ray.

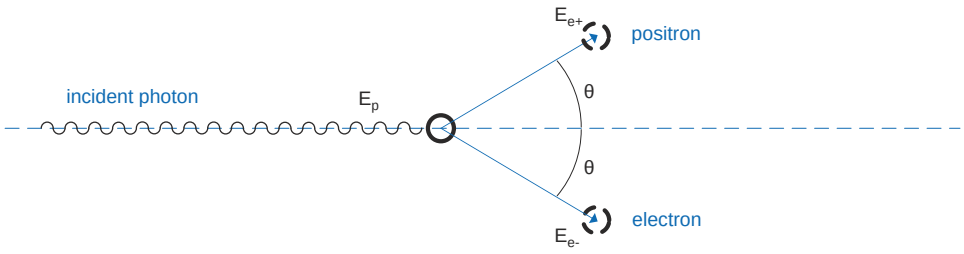

Figure 3.5: Schematic illustration of pair production (positron and electron).

The pair production is a phenomenon, where similarly to the photoelectric absorption, the original photon is absorbed in the material. In this case though, a whole new pair of particles instead of one photoelectron is generated. This pair is composed of particles of an opposite polarity, an electron and a positron (see figure 3.5). The energy above the mentioned 1.02 MeV is then shared into the positron E_{e+} and electron E_{e-} as kinetic energy

$$E_{e+} + E_{e-} = h\nu - 2m_0c^2. \tag{3.7}$$

The generated positron is not a stable particle and when losing its kinetic energy traveling through the absorption medium, it eventually annihilates. This positron annihilation results in two emitted photons with an energy of $m_0c^2 = 0.511$ MeV. The probabilities of pair production and corresponding effects are controlled by very complex equations that are not relevant for this thesis.

3.2.4 Energy spectrum

Whereas photoelectric absorption results in full deposit of the original photons energy into the detecting medium, Compton scattering and pair production might for finite medium sizes result in incomplete energy conversion. Energy leaking from the detector medium is caused by escaping scattered photons or one or both particles in case of pair generation. The interaction can be even more complex, in the sense that more interaction events can be chained. A Compton scattered photon can result in a new photon that can be scattered and eventually the deposited energy varies and an initial Compton scattering can result in full energy deposit. In other words, when no particle escapes from the medium, then the energy deposited is always equal to the incident photon energy.

The reason for pointing out the full deposit of energy is the process how the energy spectrum is obtained afterwards. The events (all the possible interaction processes above) in the material – ionizing detection medium and that way creating a small charge Q – result in a small current when voltage is applied across the medium. In order to make such events detectable, usually steep potential gradient is needed and thus high voltage. The charge Q and thus the amplitude of the current produced directly corresponds to the deposited energy. A spectrum can be then obtained using the amplitude information and is therefore often call the *pulse-height spectrum*. Due to the counting nature of the problem, a finite number of particles is obtained, resulting in discrete spectrum. Therefore, so-called bins are usually used for energy ranges and if a pulse amplitude fits into the energy range of some bin, its count integer is simply incremented, denoting the fact that there was an event depositing energy covered by the bin.

A typical spectrum is a composition of collected energy amounts (converted into electrical charge) resulting from the photoelectric absorption, Compton scattering and pair production. The contributions of individual interaction mechanisms within media are strongly dependent on the incident radiation energy and are described by varying absorption coefficients. The absorption coefficients (for photoabsorption, all

types of scattering and pair production) of basic elements can be found in a database like NIST (National Institute of Standards and Technology) [32]. A simple plot (figure 3.6) for CdTe and $CeBr_3$ was prepared using the database for energies in scope of this work.

The pulses coming from full energy absorption add up to the so-called *photopeak*, which is located at the emission energy of the source.

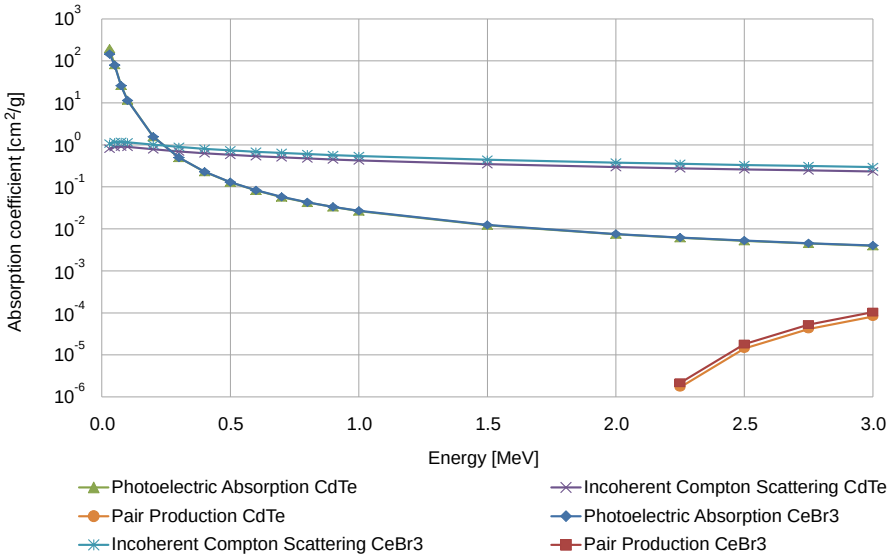

Figure 3.6: Comparison of individual interaction mechanisms absorption coefficients of CdTe and $CeBr_3$ for energies in scope of this work.

The fact that we are not able to measure the spectrum precisely (ideally it would be a number of lines – infinitely thin photopeaks – located directly at the emission energies since the emission of gamma is a deterministic process from a wavelength point of view) comes from different parts of the whole measurement chain. Neglecting the influence of electronics and all higher signal processing levels placed above the raw physics, the basic resolution-affecting cause is the interaction itself. The incident radiation causes a train of interaction events. In general there are three options from the spectroscopic point of view. The first one is that the radiation directly deposits its full energy in terms of photoelectric absorption of all possibly scattered photons, that way this event contributes to the photopeak. The other option is that some of the scattered photons escape the interaction medium and cause a loss of energy that could have been depositing by full absorption. This case produces lower energies in the spectrum called Compton continuum (resulting from direct Compton interaction, not from a train of events). The so-called Compton edge is where the Compton continuum ends in the spectrum. The (deposited) energy where this edge is located according to equation (3.6) is at

$$E_c = h\nu - E_{e-}\Big|_{\theta=\pi}, \tag{3.8}$$

when the recoil electron is back-scattered and the energy of it is maximized, whereas that of the scattered photon is minimized.

Even a more special case comes into play at higher energies, where positron-electron pairs are generated. This will again either result in an absorption of both annihilation photons, incrementing the photopeak, or in an absorption of one of the two photons whereas the other escapes the medium, or both escaping the material. These phenomena are called *single and double escape peaks* respectively. The energy of these peaks depends on the energy deposited in the medium,

$$E_{sp} = h\nu - E_{e-} = h\nu - 0.511 \tag{3.9}$$

for the single escape peak and

$$E_{dp} = h\nu - 2E_{e-} = h\nu - 1.022 \tag{3.10}$$

for the double escape peak.

A typical spectrum featuring all the mentioned effects is shown in figure 3.7.

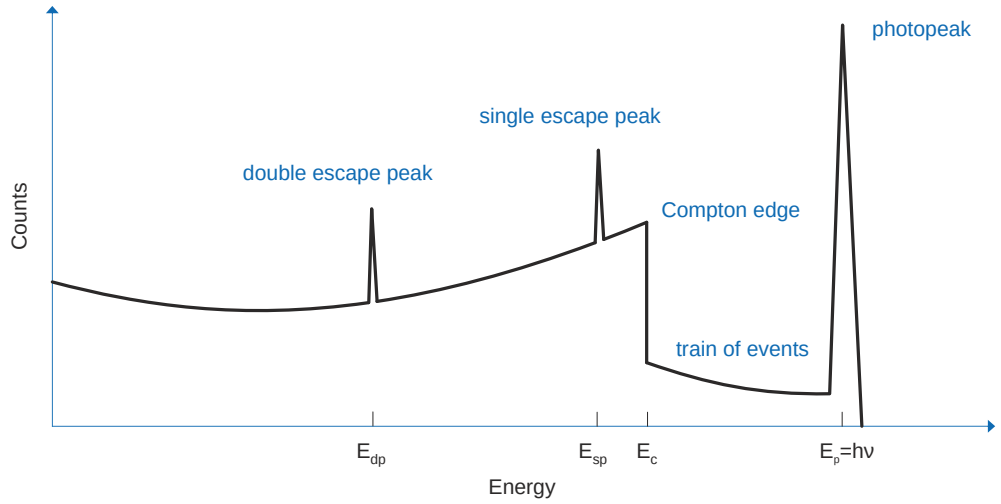

Figure 3.7: Typical spectrum of a gamma detector.

3.2.4.1 Size of the medium

The size of the detection medium directly influences several factors. At first, it is the nature of how spectra are "collected". A typical spectrum is a record of history of interactions in the detection medium. The recorded statistics depends on the number of events at energies in scope of the measurement. The number of events is dependent on the absorption at different energies. For higher energies, the absorption in a medium that is not infinitely large will be lower than for lower energies (total absorption expressed as a sum of the curves in figure 3.6). Thus, typically lower energies in spectra are recorded in a "better quality" in terms of statistics (statistically significant sample) than higher energies. In order to maintain larger number of events and thus better spectrum from a statistical point of view, the recording time window and medium (crystal) size shall be large enough.

Another factor that is directly influenced by the size of the medium is the general composition of Compton continua, escape peaks and photopeaks (characterized by their ratio, relative height, etc.). The above mentioned leakage of energy results in apparent Compton continua, escape peaks and reduced photopeaks. Their amplitude relative to photopeak directly depends on the crystal size. Apparently, for smaller medium size, gamma radiation penetrates easier (deeper) and its absorption is low and if it eventually gets absorbed, there is a significant probability that part of the original energy brought in escape in subsequent events (Compton scattering, pair production).

For higher count rates smaller sizes are preferred, leading to worse spectrum quality (in terms of Peak-To-Compton, Peak-To-Total ratios defined in 3.8). For a better spectrum quality, large (ideally infinitely) detector is needed. Therefore, to design a detector that shall meet requirements on spectrum quality and specified count rate, is always a task of finding a compromise between the two.

There are several interaction media used for detecting incoming gamma rays. These will now be covered in following three sections. The first two will describe detectors used for spectroscopic applications, the last section will summarize other available techniques available to date.

3.3 Indirect conversion with scintillators

The first large area of detectors of gamma rays are those that incorporate scintillation materials. These materials do not convert incident radiation directly into electric charge as described in 3.2.4, but generate light proportional to energy of the gamma ray. The light is emitted in a form of secondary photons, which are generated during valence electron state decay (the nature of light emission depends on the type of material). The light outputted from a scintillation material must be collected and converted into an electrical signal, in order to further process and quantize the information about incoming radiation. Although the way of collecting signal is quite different in this case, the mechanisms the particles undergo, statistics and thus the recorded spectra are the same.

3.3.1 Scintillators

There are hundreds of scintillation materials available today. The history of scintillation is now more than a century old, the first scintillation counter was built by Sir William Crookes in 1903 [22]. Nevertheless,

new materials are still being discovered today thanks to thousands of scientist on a rather challenging quest, search for an ideal scintillator. An ideal scintillator should have very high light yield per unit incoming photon energy, sufficiently fast response in order to prevent subsequent pulses overlaying each other and other important characteristics like stability, ideal emission wavelength and index of refraction in order to make a good coupling to a light detecting device with minimum losses.

Scintillation wavelength depends on the material and the crystal itself shall be transparent for it. In other words, the light photons must not be absorbed before even exiting the crystal. Another aspect for wavelength is the maximum efficiency point of a subsequent light-collecting device.

Suitable scintillation materials will be summarized in section 4.

3.3.2 Light detection

Several different light detectors are used for collecting and converting the light outputted from a scintillation crystal. The most frequently used are photomultiplier tubes (PMTs).

3.3.2.1 Photomultiplier tubes

Photomultiplier tubes are devices that convert photons with a wavelength dependent on the PMT design into a flow of electrons. Moreover, the total number electrons is multiplied, yielding in total more electrons than the number of detected photons. The typical number of electrons per scintillation even on the output of the PMT is $10^7 - 10^{10}$ [43].

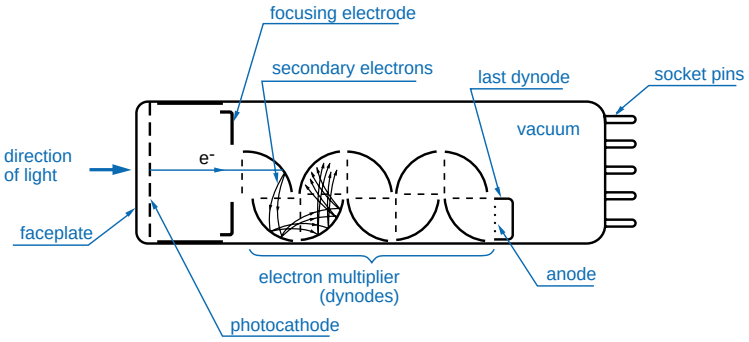

Figure 3.8: Layout of a standard PMT (taken from [29]).

PMT is composed of several components as shown in figure 3.8. The first component that the light encounters after exiting the scintillation crystal, is its photocathode.

Photocathode

Photocathode serves as a converter of incident light into an electron flux similarly to old video recording vidicon, in the opposite way than it was used in old televisions. Not every incident photon results in the emission of an electron. The probability of emission depends on the material and its thickness. The photocathode poses a barrier and it must be assured that an incident and absorbed photon not only generates an electron to be emitted, but that the electron actually escapes the photocathode. The barrier that the photocathode poses to escaping electrons depends on the combination of its thickness and material. While this potential barrier is for metals greater than 3-4 eV comparable with the energy of 3 eV for a usual incoming photon from the scintillator, there are semiconductors that can be modified to result in barriers as low as 1-2 eV. Due to this low limit of a barrier (>1 eV), absorbed light photons with energy $E_p = h\nu$ do not generate escaping electrons for low ν (long wavelength). This phenomenon results in a usual cutoff frequency in the red or infra-red range of the spectrum.

The photocathode thickness and its material is always a compromise between semi-transparency (thick enough in order to stop most of the light) and potential barrier for electrons. Whereas semiconductors pose a smaller potential barrier compared to metals, their stopping power (in terms of absorption of incident photons) is also smaller. For that reasons, compounds of semiconductors which consist of alkali metals with low potential barrier for the electrons are used. Manufactured PMTs are usually coated with compounds like CsI, CsTe, SbCs, SbRbCs, SbKCs, GaAs(Cs), AgOCs and other materials [29]. The most popular material with two alkali metals like SbRbCs and SbKCs is called bi-alkali. The bi-alkali photocathodes feature high sensitivity and low noise. It is most sensitive in the range of emission wavelengths of NaI(Tl) and other popular scintillators (see figure 3.9).

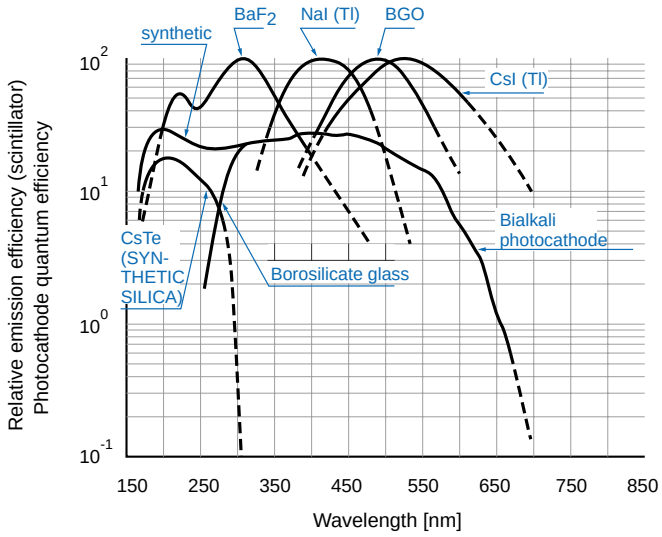

Figure 3.9: Photocathode quantum efficiency and emission spectra of major scintillators (taken from [29]).

The sensitivity of the photocathode is measured in terms of its quantum efficiency,

$$\eta = \frac{n_e}{n_p} \tag{3.11}$$

with n_p being the number of incoming photons and n_e the number of emitted photoelectrons. The quantum efficiency of commercial PMTs at their sensitivity maximum is up to 37 % (CsTe at 220 nm [29]). The common efficiency for bi-alkali and multi-alkali photocathodes is about 25-30 %. For comparison, modern technologies for silicon photodiodes commonly offer a quantum efficiency of more than 70 % [30].

Noise in photocathodes disturbing the final proportionality of emitted electrons to the number of incident photons comes from more sources, where the most critical is thermal electron generation. These electrons, when they escape the material, are unfortunately multiplied by the following multiplier. When counting, these dark currents influence the resulting spectra at low pulse heights (see figure 3.10).

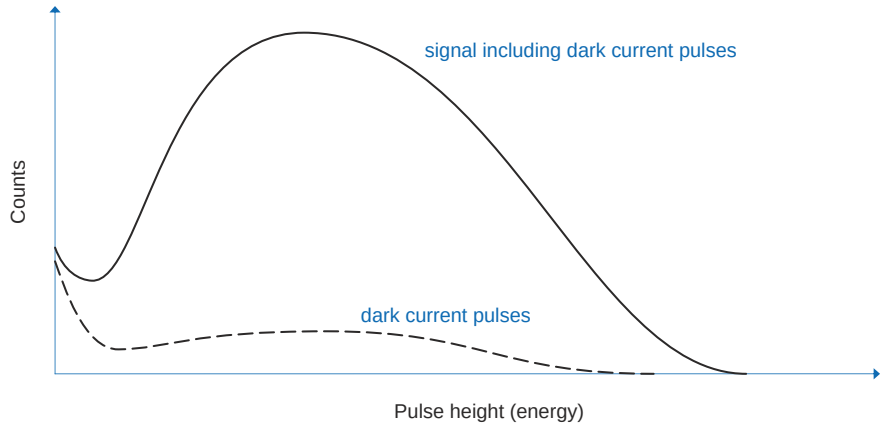

Figure 3.10: Pulse height spectrum showing the PMT dark influence on the resulting signal spectrum. The dashed line shows a typical spectrum of a PMT (taken from [29]).

Electron multiplier

The number of electrons emitted from the photocathode is small and thus, the weak signal does not suffice for satisfactory detection in terms of high resolution and low noise. Electrons are multiplied by a number of subsequent elements called *dynodes*. Dynode is an electrode coated with a material that is able to generate secondary electron emission. Incident electrons on the dynode are not only re-emitted, but their number is multiplied. The common multiplication factor δ is around 4-10, strongly depending

on the voltage bias of the PMT. Dynodes in a sequential manner amplify the electron flux and thanks to secondary electron emissions exponentially increase the initial number of electrons. The overall gain is then

$$K = \alpha\delta^N \tag{3.12}$$

for N consequent dynodes with a fraction of α photoelectrons entering the multiplication process.

As the secondary emission depends on the incident electron energy, usually high voltage is applied to boost this electron energy. The inter-dynode voltage is distributed using a passive voltage divider. In case of high electron fluxes, voltage regulation becomes unstable with passive resistor and therefore active elements are preferred.

Noise in electron multiplication originates from two major sources. The first is, as in case of the photocathode, the thermal electron generation. The second resolution-limiting factor is the fact that the multiplication factor δ is not constant. Its value is a function of statistics and fluctuates around its average. The process of multiplication is from a statistical point of view a product of random variables with Poisson distribution. In literature this is known as Galton-Watson branching process. It can be shown [87] that the mean value of the total gain K for independent dynode emissions is

$$\mu_{el} = \delta^N \tag{3.13}$$

and its variance is

$$\sigma_{el}^2 = \frac{\delta^N(\delta^N - 1)}{\delta - 1}. \tag{3.14}$$

The equation can be further treated and the mean can be incorporated (squared due to rules for incorporating constants into variance),

$$\sigma_{el}^2 = \frac{\mu_{el}^2}{\delta^N}\left(1 + \delta + \delta^2 + ... + \delta^{N-1}\right) = \mu_{el}^2\left(\frac{1}{\delta} + \frac{1}{\delta^2} + ... + \frac{1}{\delta^N}\right), \tag{3.15}$$

which can be for $\delta >> 1$ approximated by

$$\sigma_{el}^2 = \mu_{el}^2\frac{1}{\delta - 1}. \tag{3.16}$$

Equation (3.15) shows the largest influence on total fluctuation coming from first dynodes (these fluctuations get amplified by following dynodes). The term coming from the first dynode (photocathode) $\frac{1}{\delta}$ is the most dominant. Therefore, the comment above that the major source of noise is the thermal generation of electrons in the photocathode is true.

The equation (3.16) can be used to obtain the total gain fluctuation factor

$$L^2 = \frac{\sigma_{el}^2}{\mu_{el}^2} = \frac{1}{\delta - 1}, \tag{3.17}$$

which can then be used to calculate deviation of fluctuating electrons. For a number of m output electrons on the anode, the standard deviation is then simply

$$\sigma_m = Lm. \tag{3.18}$$

Anode

The generated electron flux eventually hits the anode. Anode is the last element of the PMT, where electrons are collected and outputted from the PMT. The shape of anode is optimized for electron collection from the preceding dynodes.

The whole assembly is usually enclosed in glass to make it air-tight. Vacuum is required for the electron multiplication as it enables low energy loses and high influence of applied electric potential on the momentum of electrons. Photomultipliers are manufactured in various sizes and configurations, suitable for different sizes of scintillation crystals. PMTs are typically very fast compared to semiconductors. The typical rise time is 1-3 ns and transit time (not relevant for spectroscopy) in order of tens of nanoseconds.

3.3.2.2 Semiconductors

Another method of detecting scintillation light is using semiconductors. These can be simple photodiodes with a disadvantage of no amplification of the signal, although they provide higher quantum efficiency than photocathodes. More promising detectors are *avalanche photodiodes* (APDs). Thanks to the strongly non-linear I-V characteristics of a diode (see figure 3.11), signals can be amplified using the reverse bias region where voltage changes slightly, whereas current rises to high values (through an avalanche). This effect can be used for photon detection in the APD. In order to maintain a regime where output current is proportional to input light yield, high bias voltage has to be used. The voltage must not be too high to avoid an unending avalanche and thus losing the amplitude information. Such an exaggerated avalanche mode is used in Geiger-Müller detectors and is called the *Geiger mode* of an APD. One flaw of the large amplification of the signal is that APDs are very sensitive to noise. Thermal generated electrons pose a real issue and generate non-negligible dark currents. Moreover the gain is temperature dependent as well (decreases with temperate at a rate of about 2 % per °C) [43]. One of the large advantages as opposed to PMTs is the insensitivity to magnetic field.

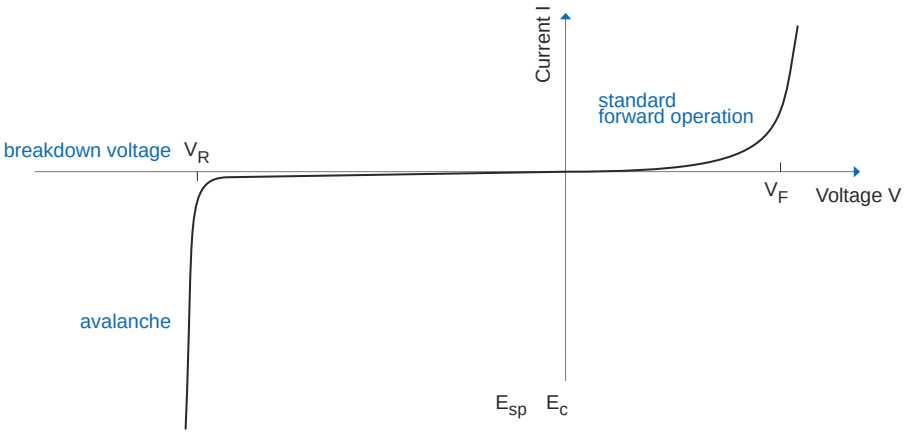

Figure 3.11: Avalanche region illustration by an IV plot of a diode. This effect is used in APDs.

3.3.2.3 Other detectors

Avalanche photodiodes in Geiger mode can be used in a special configuration and that way retain the energy information. Such configuration is an array of tiny pixels (which are much easier to manufacture than large blocks and are also faster) and such a detector is then called a *silicon photomultiplier* (SiPM). If the pixels are sufficiently small, the probability that a photon generated by scintillation will hit the pixel is very small and increases with higher light yield. Then, simply by taking a ratio of the number of pixels that detected a photon to the number of pixels in total, information about the collected amount ot light can be retained.

Other group of silicon detectors are so called *silicon drift detectors* (SDDs). These detectors can be used either directly as radiation detectors or can be coupled to a scintillation crystal to read the light output [24]. SDD is made of high purity silicon with improved characteristics. They offer compensated electron/hole lifetimes and improved impurities in the crystal. But as such, SDDs are semiconductor detectors made of silicon listed in table 4.4.

3.4 Direct conversion with semiconductors

Similar to the principle of conventional photodiodes for light (visible radiation) detection, semiconductors can serve as detectors of gamma radiation. Compared to light, gamma radiation penetrate though material to much greater depths. Absorption of high energy gamma rays is possible only with a thick *high-Z material* (Z as the atomic number implies high density), that is why it can be so lethal due to hardly being absorbed by a standard shielding.

When a photon undergoes an interaction in the semiconductor material, a small charge is induced. This charge, which is represented by both electrons and holes in the semiconductor material, corresponds to the energy of the incident radiation. In order to prevent the charge from recombination and in order to speed up the readout of the charge to allow new events occur without any influence on the previous event, high voltage bias has to be applied. The voltage is applied in a reverse manner. That way a very

small current flows between the adjacent electrodes of the crystal. The amplitude of it carries then an information about the incident radiation energy. The speed of the charge collection strongly depends on the conditions – the voltage field, carrier lifetime and mobility, size of the detector (way to be traveled) and its geometry.

There are several different materials used. Selection of a material is always a compromise of several limiting factors like temperature noise, resolution, speed and similar. Many materials exhibit induced charge collection problems and other issues related to the way of collecting signal from the semiconductor. These problems are to be discussed in the section about materials, particularly in subsection 4.3.2.

3.5 Other techniques of gamma radiation detection

Other techniques not commonly used for spectroscopy include detectors with gas interaction media. Detectors where interaction in gas takes place are Geiger-Müller tubes and ionization chambers. More on these types of radiation detectors can be found in a standard literature like [43]. Such detectors are mostly used as simple counters, working in the saturated mode ("infinite" amplification) where probability of missing an event is small, but at the expense of losing the pulse amplitude information carrying the information about the gamma ray energy.

A special technique that fits under the category of semiconductors are silicon drift detectors (SDDs). These were already mentioned as light-collecting devices where they are used as well – see part 3.3.2.3. High purity Silicon, usually drifted with Lithium form the SDD. Detected charges are then drifted to a central FET used for the detection. The drift is accomplished using a carefully distributed voltage potential in the material. More on SDDs and its applications in X-ray spectrometry can be found in articles [47] and [79].

3.6 Electronics

The raw output of the core detector is a signal with low amplitude and fast decay times. In order to process the pulses and their amplitudes to get the count spectrum, the signal has to be modified. The modification usually consists of charge sensing (current-voltage converter), its amplification, filtering (limiting its bandwidth) and pulse shaping (slowing the pulses down to make them suitable for subsequent pulse analysis). The subsequent analysis is then done in a circuit called MCA, a *multi-channel analyzer*. The output of MCA is a pulse-height spectrum.

The main reason for the use of shaping amplifier is limiting noise coming from preceding components. This is done by limiting the frequency bandwidth of the signal, reducing its fast-decay components in the time-domain. The noise can be greatly suppressed at low count rates. At higher count rates, the decay of pulses has to be fast enough to prevent the *pulse pile-up*. By the nature of the problem, the ability of processing high pulse count rates comes at the expense of increased noise in the system.

With the evolution of transistor circuits, digital acquisition and processing has become a dominant solution substituting analog circuits. A typical analog circuit for pulse-height spectrum acquisition contains a charge-sensitive preamplifier, pulse-shaping amplifier and MCA. The design can be done using basic electronic blocks like RC/CR elements. In order to prevent undesired phenomena occurring at higher count rates, more complex designs have to be used. Moreover, there is hardly any possibility for user-controlled parameter settings. Once the circuit is designed, it can hardly be changed.

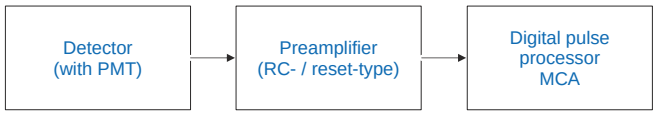

Figure 3.12: Block diagram of a typical measurement chain for digital acquisition.

On contrary, digital circuits can offer users many parameters they can configure. A typical digital acquisition is composed just from a preamplifier and a digital unit (DPP – digital pulse processor) that samples the output of the preamplifier and calculates the energy spectrum (MCA part). This is shown in figure 3.12. A typical computing unit is based on a digital signal processor (DSP) and/or an FPGA. Different configurable pulse-shaping and pulse-filtering algorithms can be used, for example for pile-up rejection. As long as the the unit manages to keep up with the incoming pulses, it can employ any modern feature the user configures. The speed is not only limited by the real-time computations. In fact, off-line

algorithm are often used in a second branch, taking batches of samples and processing them independent of the main branch.

In the table 3.2 summary of advantages of digital processing versus analog processing is shown.

Processing unit	Analog	Digital
Noise at high counts	moderate	low (true trapezoid filter)
Linearity	very high	high (ADC non-linearity)
Stability	sufficient (component temp. drifts)	high (oscillator and reference drifts)
Nature of filtering	IIR (infinite response)	favorable FIR (finite response)
Power consumption	moderate	high (fast clock)
On-line configuration	impossible	very broad
Off-line configuration	difficult	very broad
Pile-up rejection	hardly possible	many algorithms
Baseline shift	large	small

Table 3.2: Comparison of analog and digital pulse processors, taken from [67], [26]

3.6.1 Preamplifier

The *preamplifier* is a key element in converting the induced charge from the detection medium to a voltage signal. Usually, an *RC-type* (or sometimes called *resistive feedback*) *preamplifier* is used. It amplifies pulses and stretches them to a step-like signal. In order to produce ideal pulse-induced steps, its rise time shall be the lowest possible, whereas its fall time should be slow. With a longer fall time, pile-up increases and this might result in saturating the amplifier. Such a case is shown in figure 3.13, taken from one of the presented measurements done in the radiation chamber with a strong ^{137}Cs source (resulting in a dose rate of 111 mSv h^{-1}). The maximum number of bits for the amplitude was in this case 1024, so it can be seen that there is still room, but at this dose rate, the signal was found nearly to being out-of-range several times. For a rail-to-rail amplifier, the maximum output is limited by its supply voltage level. Different designs must be used to prevent saturation, like a *reset-type preamplifier* [70]. A reset-type amplifier does not wait until its output saturates, but does a cyclic reset. That introduces a dead time (during which the amplifier output goes to zero), but prevents saturation.

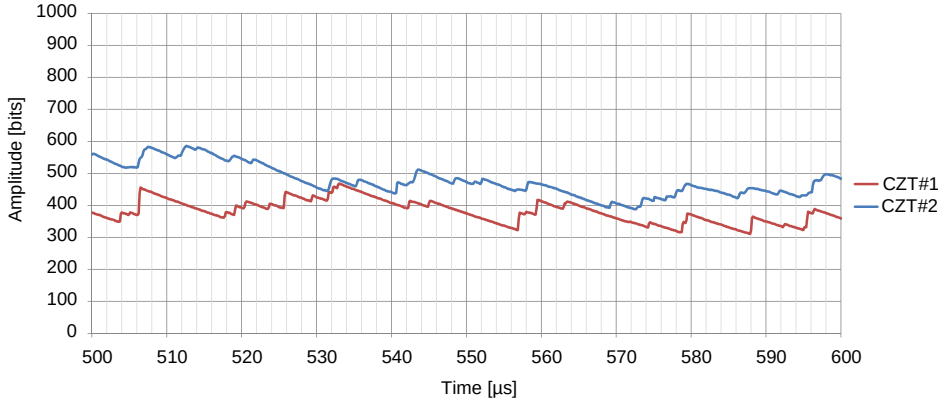

Figure 3.13: An RC-Type preamplifier. Measured with a CdZnTe detector at a dose rate of 111 mSv h^{-1}.

A typical charge-sensitive amplifier is a fast operational amplifier with a negative feedback. In its negative feedback, a capacitance and a resistance (and therefore it is of RC type) is present. However, a different, but similar design was used in my case (to be discussed later in section 6.4.2 and shown in figure 6.5). The capacitive load of the preamplifier input must be as low as possible for the highest signal-to-noise ratio. In order to keep the capacitance low, the input shall be as close as possible (short or no cable) to the detector itself. The preamplifier input should ideally pose no impedance to the detector, acting as short circuit.

3.6.2 Digital pulse processor – MCA

As already mentioned in the previous section, digital or analog signal processing can be used for pulse analysis. As in our case a digital option was used, analog design will not be described. The MCA used is purely digital, digitizing the input and then processing the digitized signal through the standard steps like pulse amplification, shaping, filtering, pile-up inspection and more. Since various manufacturers offer very different designs, no general description can be provided. The way of digital processing is often an unpublished know-how of manufacturers.

More on the DPP used is described from a user point of view in section 6.4.1.

3.7 Noise in the measurement chain

There are several factors in the whole system causing noise in the resulting spectrum. Eventually, this noise results flattening of peaks and additional background counts in the spectrum. The factors are listed sequentially as they come on after each other in the complete measurement chain:

- interaction of gamma-rays with matter (crystal) – different types of scattering (not understood as noise), scattered photons from the crystal's surrounding, background contamination (the crystal material itself is radioactive producing background counts), thermal noise and temperature shifts, charge trapping (in case of semiconductors);
- photomultiplier (in case of scintillation systems) – thermal noise, statistical gain fluctuation (generation of secondary electrons), dark current, high voltage instability, radioactive impurities in materials PMTs are made from;
- preamplifier – noise of the electronics, limited speed of the electronics (parasitic capacitance), thermal noise in semiconductors (resulting in gain variation), Johnson noise (resistor), baseline shift;
- digital pulse processor – ADC non-linearity, limited dynamic range and resolution, thermal noise of the electronics, clock instability and other factors.

3.8 Glossary of important parameters in gamma spectroscopy

There are many qualitative parameters that can be used for spectrum description. The most important used throughout the thesis are listed below. These parameters can be used for spectrum comparison without a need of comparing whole recorded spectra. Most of the parameters are related to a photopeak – and providing a quality measure of its shape.

- FWHM (full width at half maximum) – Used to describe the ratio of the width of a spectral emission at the 50% amplitude points and the position of the peak. In other words it describes how thick (high FWHM values) or thin (low values) the peak in spectrum is, compared to its height.
- Peak-To-Compton ratio – This ratio is used to describe the performance in terms of the photopeak height relative to the Compton continuum height. It is defined as a ratio of the highest number of counts in the peak divided by a count from a Compton continuum region where it is relatively flat [35].
- Peak-To-Total ratio – It is a ratio of two areas in the spectrum, the photopeak area (sum of counts belonging to photopeak) and the total area (sum of counts over all energy bins).
- Peak sensitivity – Expressed in counts per minutes or seconds per measured dose rate this parameter is a conversion factor between the peak's area and incoming dose rate (H*(10)).
- Total sensitivity – Similar to peak sensitivity, total sensitivity expresses total counts per unit time per incident dose rate. It expresses conversion of dose rate into counts in spectrum.

Chapter 4
Materials

4.1 Inorganic scintillators

Scintillation materials are characterized by many physical aspects. The key characteristics in scope of this work are its decay time (how fast the amplitude of a generated pulse decays in time) and light yield (generated photons per incident 1 MeV particle). Among others, emitted light wavelength is important as well as the crystal transparency to this wavelength. Apparently crystals that damp its own outputted light cannot be used. In figure 4.1 scintillator materials evolving in time are shown (taken from [90]). The standard wide-spread materials are discussed first, after that some fast-spreading new promising materials follow.

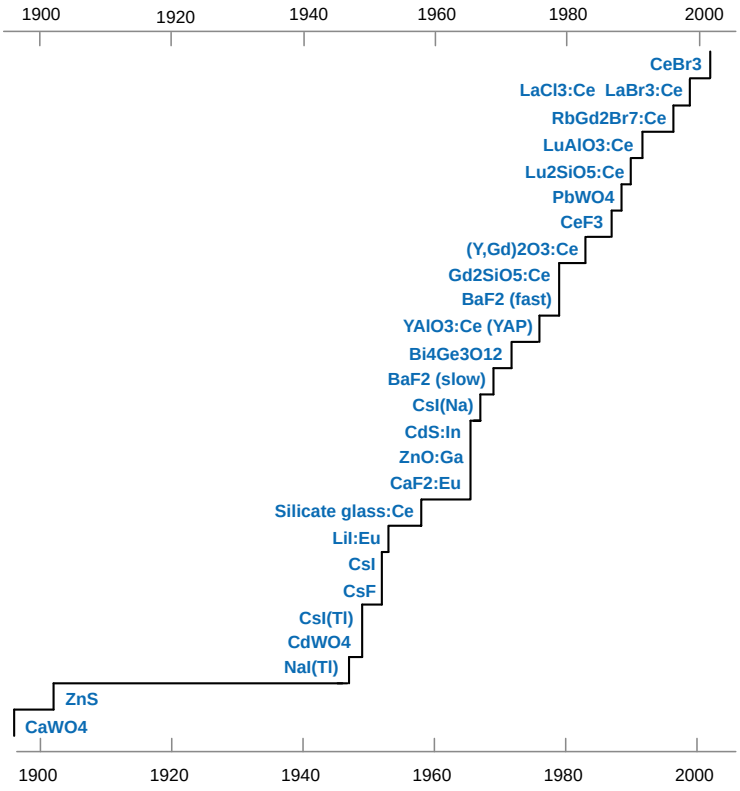

Figure 4.1: Time evolution of inorganic scintillators (taken from [90]).

4.1.1 Standard materials

The oldest inorganic scintillation materials are more than a century old. The first examples were ZnS and $CaWO_4$, which helped Röntgen to discover X-Rays. The real wide-spread (figure 4.1) came first with the discovery of excellent scintillation properties (table 4.1) of a very performing compound NaI(Tl). The material's light yield is still among the largest in this area, even today. Over time the manufacturing techniques improved and the price dropped. NaI(Tl) is still undoubtedly the most used material around.

The crystal is fast enough for most of applications (decay time of 250 µs). The only larger drawback of the NaI(Tl) is that it is hygroscopic and the afterglow of the material (found to be 0.5-5 % at 6 ms). Thus it always have to be incorporated into an air-tight enclosure to protect the crystal from humidity. The range of applications where NaI(Tl) still plays a dominant role on the market is remarkably large, starting with safety and monitoring applications, over medical applications and ending with the most up-to-date space technologies where these detectors are also still used.

Other standard wide-spread materials include CsI(Tl) from the fifties, another material with high output and emission wavelength close to optimum of diodes and photomultiplier tubes. Other variants of the basically same material include a very fast, but with low output yield, pure CsI and a popular CsI(Na). Materials CsF and BaF_2 are among the fastest available standard materials. The drawback of CsF is again its low output yield and thus bad resolution. The mentioned BaF_2 poses another problem, it has two physically different emissions, each with different intensity, decay time and emission wavelength. The so-called *fast component* of BaF_2 is with 600 ps one of the fastest observed among all inorganic scintillators so far. The second component is much slower compared to the fast component and produces higher output yield. There are ways of filtering out the *slow component*, keeping the fast one intact. One of them is doping the crystal with rare Earth materials [71], another way is to place an optical filter between the crystal and PMT [93] or use a special PMT with a CsTe photocathode [93]. But again, nothing is for free, the fast component that remains does not produce enough light to produce spectra of high resolutions. The best achieved resolutions at 662 keV are around 15-20 % [12].

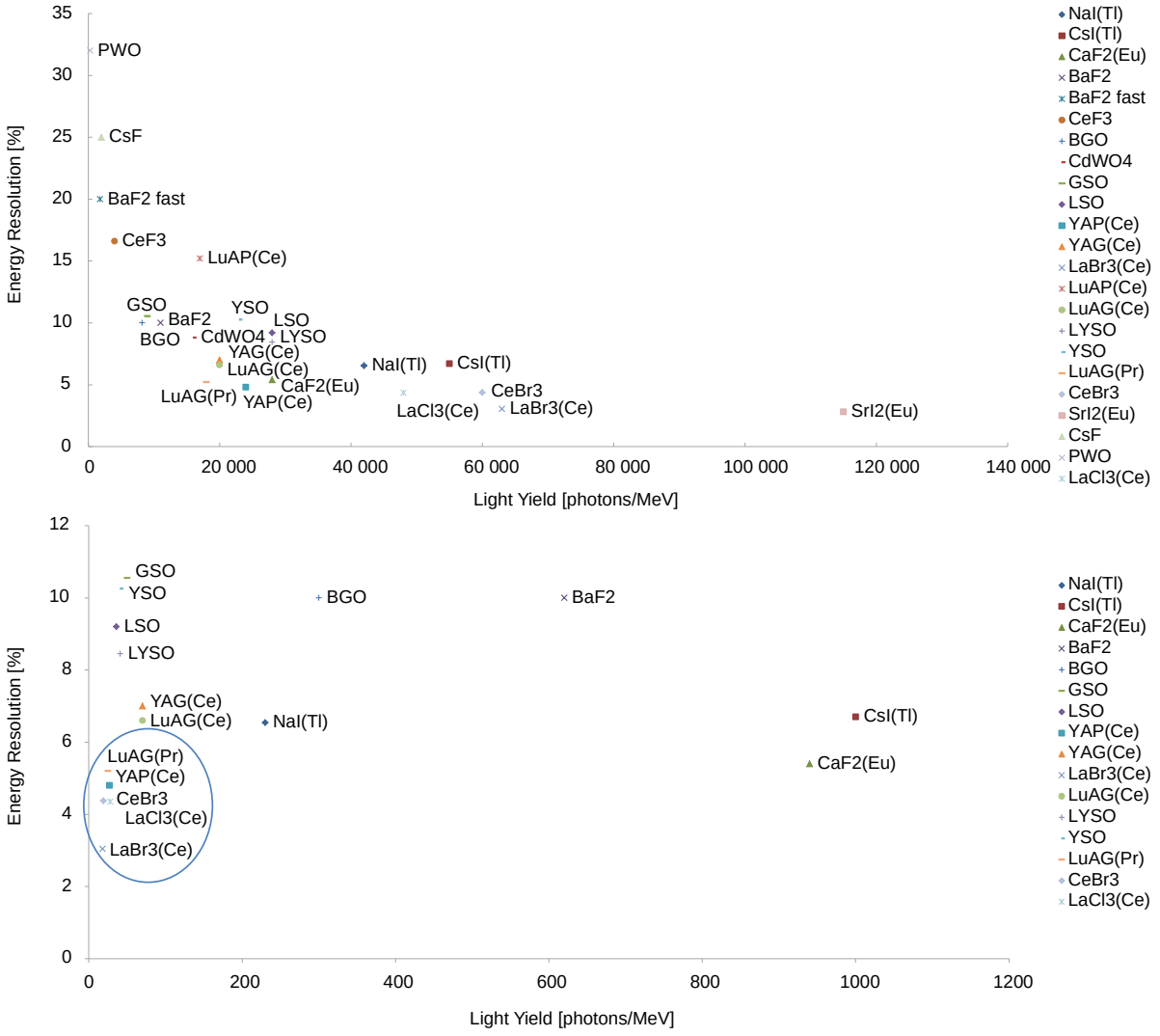

Figure 4.2: The upper plot shows a comparison of resolution (i. e. FWHM) and light yield of the scintillation materials listed in table 4.1. The exponential character of the data is caused by the underlying theoretical limit for scintillator read-out efficiency. The lower plot shows a comparison of the decay constant and resolution of the fastest scintillators, the best materials in terms of suitability for this thesis, are marked in the plot.

4.1.2 New materials

The new materials with high potential developed in the last 3 decades include high density PWO, LuAP, LSO and LYSO materials, which are all very fast and even faster materials like $LaBr_3(Ce)$ and similar. Unfortunately, most of the high-Z materials show very bad energy resolution (see table 4.1) and are thus not suitable for the application. More promising are $LaBr_3(Ce)$, $LaCl_3(Ce)$, YAP(Ce) and $CeBr_3$, which are all marked in the candidate plot in figure 4.2. There is one more candidate marked in the plot, LuAG(Pr), but that material is not commercially available at the moment. The other mentioned materials are available on the market and widely used, though. These materials will now be compared and discussed one by one.

4.1.2.1 $LaBr_3(Ce)$ and $LaCl_3(Ce)$

The most popular new crystals are lanthanum bromide $LaBr_3(Ce)$ and a slightly modified lanthanum chloride $LaCl_3(Ce)$. The crystals largest producer is a French company *Saint-Gobain* and sells them under brand names *BrilLance 380* and *BrilLance 350* respectively. The material is very fast, depending on the cerium (Ce) doping (usually 1-5 %) and total size of the crystal. Researchers claim the material not to be slower than 25 ns, the Saint-Gobain datasheet even lists the decay time as 16 ns only. Manufacturers of these materials recommend it for high-count applications with potential count rates in range of few MHz (*Saint-Gobain, Hellma*).

The Lanthanum component leads to non-negligible self-activity of the crystal. The intrinsic background spectrum posses lines corresponding to the decay of ^{138}La at energies under 1.5 MeV and to decay of ^{227}Ac for energies in the range of 1.5 MeV and 3 MeV. The lanthanum component can be seen in figure 4.3, where europium spectra are compared (see table 7.2 for emission energies of ^{152}Eu).

Thanks to its high light yield that even tops out that of NaI(Tl), the lanthanum bromide is by far the best scintillator in terms of energy resolution. At 662 keV the best achieved values are as low as 2.6 % at room temperature [2]. Other measurements shown in the table 4.1 confirm the excellent resolution obtained at room temperature. Some researchers report issues (gain stability and linearity) when coping with such large yields from larger crystals with standard photomultipliers [76].

$LaCl_3(Ce)$ is a slightly modified and cheaper material, with worse but not bad properties. Its energy resolution is above 4 % and its decay time constant is 28 ns as shown in the table. Overall, the characteristics are very similar to that of its sister $LaBr_3(Ce)$.

Both materials are radiation stable and their temperature stability is superior to that of NaI(Tl) [57]. The largest drawback of these material is that they are both hygroscopic and care must be taken in order to avoid contact with air and moisture. The material price is moderate, expensive when compared to NaI(Tl), due to its difficult manufacturing process of growing the crystal.

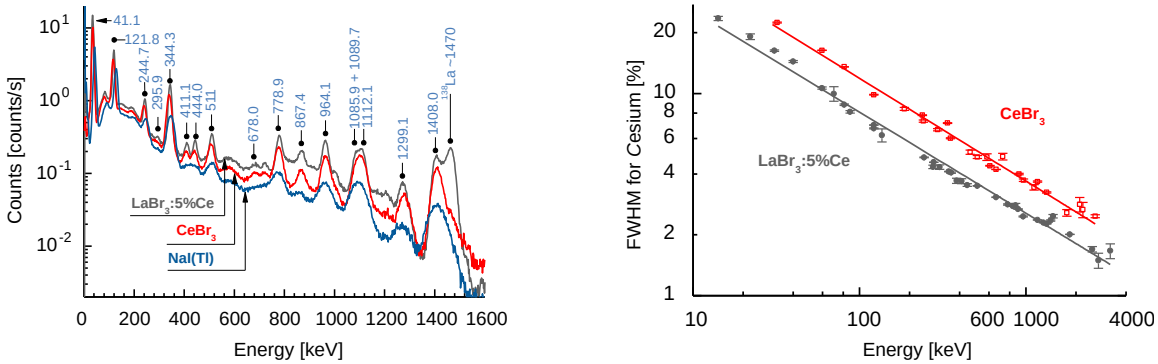

Figure 4.3: The left plot shows ^{152}Eu spectra measured with NaI(Tl), $LaBr_3(Ce)$ and $CeBr_3$ (2-inch crystals). The right one shows a comparison of $LaBr_3(Ce)$ and $CeBr_3$ in terms of their resolution. Both taken from [65].

4.1.2.2 $CeBr_3$

Cerium bromide is another material with excellent properties, very suitable for spectroscopic measurements. The price is comparable to that of $LaBr_3(Ce)$, the speed of the crystal as well (19 ns). Its energy resolution is one of the best achievable with inorganic scintillators, measured around 4-5 % (see table 4.1). Its perfect intrinsic characteristics exceed that of NaI(Tl) and $LaBr_3(Ce)$ and the gain stability was tested for temperature ranging from -20 to 50 °C [59].

The $CeBr_3$ has a very low intrinsic background compared to previously mentioned crystals, with counts similar to NaI(Tl). It is important to note that NaI(Tl) is still the cleanest solution in terms of intrinsic activity. A comparison is shown in paper [65]. However, some measurements for samples of $CeBr_3$ are contaminated with ^{227}Ac. Nowadays techniques exist to monitor and eliminate such undesired contamination, leading to crystals with no or very low ($< 0.02\,\mathrm{counts\,s^{-1}\,cm^{-3}}$) ^{227}Ac contamination (more details can be found in [65]).

No or minimum afterglow was observed for this material according to the patent [74]. The material is hygroscopic. A comparison with $LaBr_3$(Ce) and NaI(Tl) in terms of resolution and self-activity can be seen in figure 4.3.

4.1.2.3 YAP(Ce)

Another very interesting fast scintillation material is yttrium aluminum perovskite doped with cerium ($YAlO_3$(Ce)). Its decay time is as short as 27 ns [55], suitable for high count rates. In the same article, a negligible slow component of low light yield is reported, its light yield relative to the sum of both components was measured in several articles to be between 2-11 %.

One great advantage of the YAP(Ce) is that it is not hygroscopic. Its emission spectrum peak is promising as well, located near a maximum of the bi-alkali photomultiplier tube. Almost no afterglow is observed for this material (< 0.005 % at 6 ms) [7]. The material is temperature stable according to its manufacturer *Crytur* in the Czech Republic.

Regarding its resolution, several researches measured it under normal conditions with room temperature for cesium (Cs^{137}). The results are rather promising again, the energy resolution is found to be around 4-5 % (see table).

The price of all the presented new materials mentioned in this section is comparable.

Material	Density [g cm^{-3}]	Refr. Index [-]	Light Yield [phot.MeV^{-1}]	Decay τ [ns]	Em. Peak [nm]	Hygrosc. [-]	Afterglow [% after 6 ms]	FWHM Resolution [%, PMT & room temp.]	Resolution Sources [references]
NaI(Tl)	3.67	1.85	42 000	230	415	yes	<1	6.7, 6.4, 6.5, 6.6, 6.5	[75], [2], [82], [56], [25]
CsI(Tl)	4.51	1.79	55 000	1000	565	slightly	<2	6.6, 6.8	[56], [83]
CaF_2(Eu)	3.18	1.44	28 000	940	435	no	<0.3	5.4	[50]
BaF_2	4.89	1.49	11 000	620	310	no	-	10	[12]
BaF_2	4.89	1.49	1 800	0.6	210	no	-	20	[12]
CeF_3	6.16	1.68	4 000	29	300	no	-	17.0, 16.2	[42]
BGO	7.13	2.15	8 200	300	480	no	<0.005	8.5, 10.0, 11.5	[56], [52], [25]
$CdWO_4$	7.90	2.25	16 000	5000	540	no	-	8.8	[53]
GSO	6.71	1.85	9 000	50	440	no	<0.005	9.2, 11.9	[9]
LSO	7.35	1.82	28 000	36	420	no	-	8.4, 10.0	[9], [56]
YAP(Ce)	5.55	1.93	24 000	27	365	no	<0.005	5.7, 4.7, 4.4	[56], [64], [63],
$LaBr_3$(Ce)	5.29	1.80	63 000	18	380	yes	-	2.6, 3.0, 3.2, 3.2, 3.2, 3.1	[2], [82], [75], [82], [58], [25]
$LaCl_3$(Ce)	3.79	1.90	48 000	28	350	yes	-	4.2, 4.5	[2], [89]
LuAP(Ce)	8.30	1.95	17 000	18	365	no	-	15.2	[8]
LYSO	7.10	1.81	28 000	41	420	no	-	8.7, 8.2	[16], [89]
YSO	4.60	1.80	23 000	41	420	no	-	9.4, 11.1	[9]
LuAG(Pr)	6.68	1.84	18 000	25	310	no	-	5.2	[80]
$CeBr_3$	5.07	2.09	60 000	19	380	yes	-	4.2, 5.2, 3.8, 4.3	[21], [50], [65]
SrI_2(Eu)	4.55	2.05	115 000	1200	435	yes	-	2.8	[50]
CsF	4.64	1.48	2 000	3.5	390	yes	-	25	[54]
PWO	8.28	2.16	300	26	430	no	-	25, 32	[91]
Plastic	1	1.5	-	<2	<10 000	no	-	>15	[61]
CdZnTe	5.78	-	-	-	-	-	-	1.8, 2.0	[2], [82]

Table 4.1: Table of selected scintillation materials.

4.2 Organic scintillators

Organic scintillation materials are very popular for their low cost, but are practically not used in the spectrum measurement applications. The light yield is, when compared to inorganic scintillators, very low and the energy resolution thus very bad (around 15 % for 662 keV reported in [61] for NE102A and NE230, better for lower volumes). Only few papers measure its energy resolution, further confirming the fact that these materials are not used for this type of application. The main applications are radiotherapy, radiosurgery and other medical applications [11]. They are often used for neutron detection [44].

The organic scintillators (or sometimes called plastic due to the fact that these are actually plastic materials that exhibit the scintillation phenomena) are very fast (few ns max) and can be made into large-scaled scintillator blocks. The plastic scintillators, when compared to inorganic scintillators, have to be larger in order to detect incident radiation of higher energies, as their density is very low (see table 4.1).

4.3 Semiconductors

Semiconductor materials play an important role in radiation spectrometry. The nature of interacting with photons is widely used not only for interaction with high-energy photons like ionizing radiation, but also very popular for light detection and solar energy harvesting. In any case, the main limitation, but also a feature, is a particular material's band-gap width.

Band gap of a semiconductor directly affects reactions induced in the material caused by incident radiation. The lower the band gap is, the higher is the probability of a lightly-bound electron to be freed from its fixed configuration (to become a valence electron). This state transition over the band gap that poses a barrier is not only induced by the energy of incident radiation, but also by temperature. The barrier itself behaves in a probabilistic manner, due to the underlying quantum physics. With temperatures over 0 K, there will always be a probability that an electron is excited into the higher state over the band gap. This effect causes undesired noise and needs to be compensated. A simple compensation that is at hand is cooling. It is important to note, that this solution is current-consuming, expensive and almost always bulky, thinking of cryogenic cooling.

The energy of thermal noise is exponentially dependent on the temperature. The ratio of a probability between an electron being in the excited conduction band and an electron being in the valence band is described by the *Boltzmann distribution*

$$P(T) = e^{\frac{-\Delta E}{kT}}, \tag{4.1}$$

where k is the Boltzmann constant, ΔE the band gap and T the temperature in Kelvin. Table 4.2 shows calculated probabilities for different temperatures and materials in comparison with the valence electron density in the material.

	$P(-50°)$	$P(-30°)$	$P(-10°)$	$P(10°)$	$P(30°)$	$P(50°)$	$P(70°)$	ρ [mm^{-3}]
CdTe	1.48E^{-35}	1.56E^{-32}	5.76E^{-30}	9.27E^{-28}	7.66E^{-26}	3.68E^{-24}	1.13E^{-22}	-
Si	1.67E^{-26}	2.72E^{-24}	2.07E^{-22}	8.61E^{-21}	2.21E^{-19}	3.81E^{-18}	4.76E^{-17}	2.00E^{20}
Ge	2.37E^{-16}	6.44E^{-15}	1.07E^{-13}	1.20E^{-12}	9.81E^{-12}	6.23E^{-11}	3.20E^{-10}	1.78E^{20}

Table 4.2: Dependence of the electron excitation on temperature (in °C). The valence electron density for comparison is listed in the last column (used data from table 4.4 and [73] for calculation).

Furthermore, the band gap size itself is proportional to temperature, namely through the *Varshni equation*:

$$E_g(T) = E_g(0) - \frac{\alpha T^2}{\beta + T}, \tag{4.2}$$

where T is temperature in Kelvin and α, β are material specific coefficient. This equation was evaluated for a few points, showing the temperature influence in table 4.3. Thanks to its lower influence in comparison to the exponential thermal generation, this phenomenon can be neglected.

4.3.1 Low band-gap semiconductors

One of the most precise detector used for spectroscopy is based on *high purity germanium* (HPGe). Germanium features excellent energy resolution and is usually taken as a reference when conducting

	$E_g(-50°)$	$E_g(-30°)$	$E_g(-10°)$	$E_g(10°)$	$E_g(30°)$	$E_g(50°)$	$E_g(70°)$	$E_g(90°)$
CdTe	1.542	1.535	1.527	1.519	1.511	1.503	1.494	1.486
Si	1.141	1.137	1.132	1.127	1.122	1.117	1.111	1.106
Ge	0.692	0.685	0.677	0.670	0.662	0.654	0.646	0.638

Table 4.3: Dependence of the band gap on temperature (in degrees Celsius).

scientific experiments. Germanium detectors are rarely used as hand-held or portable spectrometers. Due to their narrow band gap (0.66 eV at room temperature and 0.75 eV for absolute zero [86]), they need cryogenic cooling in order to minimize thermal noise.

Another popular low band-gap semiconductor material is silicon. Silicon has a 1.17 eV band gap and thus also requires cooling. Silicon has outstanding properties in terms of its speed, its electron mobility is very fast. As already mentioned, silicon is mainly used for X-Ray spectroscopy in a high purity drifted form like SDD.

4.3.2 Room temperature semiconductors

There are several relatively new materials with larger band gap, high material density and low ionization potential. Such materials include commercially available or near-market GaAs, CdTe, CdZnTe, HgI_2 and TlBr [72]. Out of these, only CdTe and CdZnTe (shortly CZT) is commercially spread and available from various manufacturers. As apparent from the table 4.4, these two materials are very similar. It is however important to note the difference of speed of major and minor carriers, which is more than a factor of 10. Both crystals feature high density and acceptable band gaps (in terms of thermal noise) at room temperature. The materials are easy to manufacture in small sizes ($\leq 1\,\mathrm{cm}^3$), but very difficult to manufacture in larger scales. The material is also very expensive compared to scintillation materials.

Several modifications of a standard detector setup exist, including *Schottky detector*, *hemispheric detector* and other. These detector types are common for both cadmium telluride (CdTe) and cadmium zinc telluride (CdZnTe) and will be described below.

Material	Ge	Si	GaAs	CdTe	CdZnTe
Density [$\mathrm{g\,cm^{-3}}$]	5.33	2.33	5.32	6.20	5.78
Average Z	32	14	32	49	49
Ionization potential [eV]	2.9	3.6	4.3	4.4	4.6
Band gap [eV] (0 K)	0.75	1.17	1.52	1.61	1.67
Band gap [eV] (RT*)	0.66	1.12	1.42	1.51	1.6
Resistivity [$\Omega\,\mathrm{cm}$]	50	10^4	10^7	10^9	10^{10}
Electron mobility [$\mathrm{cm^2\,V^{-1}\,s^{-1}}$]	3900	1500	8500	800-1100	1000-1200
Hole mobility [$\mathrm{cm^2\,V^{-1}\,s^{-1}}$]	1900	450	400	80	100
Electron lifetime [µs]	-	-	-	1-3	1-3
Hole lifetime [µs]	-	-	-	1-2	0.1-0.8
Energy resolution [% FWHM @662 keV]	0.5	-	2	1-3	1-3

Table 4.4: Properties of semiconductor materials used for gamma spectroscopy (*Room Temperature), carrier mobility and lifetime represent typical values. Data were taken from [86], [19], [5], [88] and [45].

4.3.2.1 Charge trapping – low-energy tailing

The detection of ionizing radiation in semiconductors is based on generation of free electrons and holes and sensing this generated charge by applying strong electric field and thus making the charge move, producing a small, but measurable current. This current, when integrated by subsequent electronics, can express the charge amount collected and therefore the energy of an incident radiation. The charge transport itself, however, poses a problem in semiconductors, where charge trapping occurs and where speeds of the holes and electrons differ (see table 4.4). The limited speed of charge carriers, called *electron/hole mobility*, causes the collection to take time (in order of ns for small detectors up to hundreds of ns for large detectors for electrons and up to µs for holes) [68]. The charge collection time also depends on the depth where an interaction takes place, which is obviously deeper for high-energy gamma rays.

Another important parameter called *electron/hole lifetime* expresses the mean time of free electrons and holes before they recombine. Ideally, a very short mobility and very long lifetime is desired. In real semiconductor, however, the properties are limited and the mobility of electrons and holes differ. This is the case for CdZnTe as well as CdTe as can be seen in table 4.4. In order to suppress the influence, special detector geometries are used (discussed in section 4.3.2.2).

Compound detectors like CdZnTe are usually subject to charge trapping. In comparison to pure materials like HPGe or Si, compound detectors like CdZnTe, CdTe or HgI_2 have high density of defects of the crystal lattice which results in *charge trapping* [66]. This trapping then causes the collected charge (current integral) to be less than if no charge were trapped. Imperfect charge collection results in so called *low-energy tailing* or *hole tailing* in the spectrum (seen for example in figure 7.22). The largest influence is caused by hole trapping (often called *poor hole collection*) since hole carrier lifetime and is for CdZnTe typically smaller, than its collection time. For CdTe, the hole lifetime is typically longer (table 4.4), resulting in a slightly better, but still imperfect charge collection [66].

The properties related to charge lifetimes are not yet well under control from the manufacturing point of view. Although lower density of defects has been achieved by modern crystal growth techniques, charge collection properties still differ from ingot to ingot. In CdZnTe and CdTe detectors, Te is blamed to cause most of the undesired impurities [85]. Scientific research presents new methods for charge-loss correction as presented for example in [48].

4.3.2.2 Charge trapping – different geometries for charge collection

Several different layouts are being used for CdZnTe and CdTe detectors. The main difference is the design of electrodes creating electric field within the medium. The basic simple scheme of two electrodes with a semiconductor in-between is called a *planar detector*. Planar detectors collect charge induced by incoming radiation in an electric field with linear intensity. The main disadvantage of this simple design is the fact that linear electric field cannot cope with uneven electron/hole collection possibility. The 10 times higher electron mobility (table 4.4) favors for electrons to be collected.

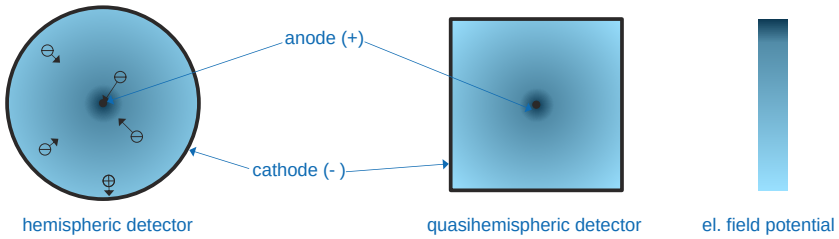

Figure 4.4: Schematic illustration of a hemispheric and quasi-hemispheric detector from the top (attraction forces for electrons and holes).

Logarithmic electric potential created by a hemispheric design (illustrated in figure 4.4) results in a so-called *single charge collection*. It favors the faster electrons as they are accelerated on the way to the central anode. Holes are slowed down in comparison to the planar detector, which results in higher probability of their recombination and trapping. This design results in better charge collection throughout the medium. Similar behavior is achieved in a detector with *coplanar geometry*, where electric field is again nonlinear.

The electron collection times using hemispheric detectors for small detectors (volume less than $100\,mm^3$) are less than 100 ns [6].

4.3.2.3 Charge trapping – polarization at high fluxes

The photon flux incident on a CdTe or CdZnTe detector shall not be unlimited. Several papers report a phenomenon called *lateral polarization* at photon fluxes in order of $MHz\,mm^{-2}$ [77]. The polarization is caused by trapped charges (both holes and electrons), where trapped holes contribute to the created space charge more than electrons. Such a build-up of space charge strongly influences the electric potential (bias) of the detector. The degraded non-linear field with weakened points is no longer capable of uniform transportation of induced charges to the electrodes as in the standard operation mode (low fluxes). The charge collection is thus imperfect, its efficiency drops with higher flux.

Complex models and studies try to model polarization in planar detectors ([10], [27]) yielding an important limitation characteristics of a detector called *critical flux*. In figure 4.5 importance of critical flux is shown, as a point beyond the flux should not be raised anymore because of a dramatic change in

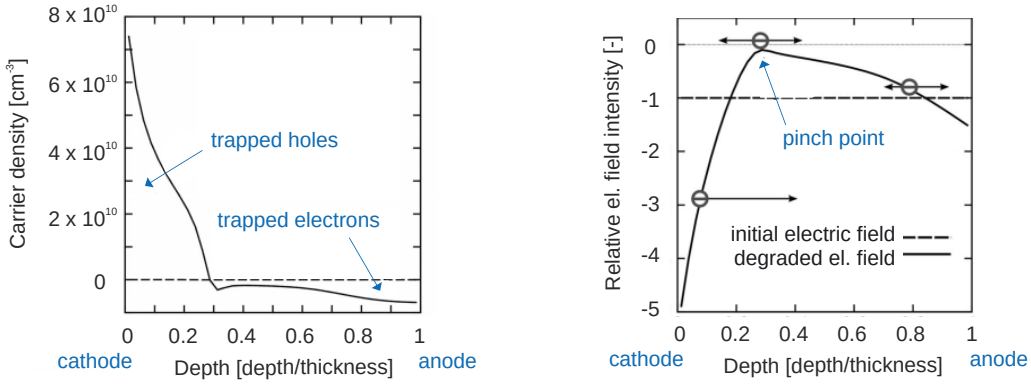

Figure 4.5: Polarization effect in a coplanar CZT detector at high fluxes. The left plot shows the trapped charge (electrons and holes) causing defects to the original electric field. The right plot is the degraded electric field itself, in the units relative to the original (low-flux) field intensity. Taken from [10].

output count rate "seen" by the detector. The whole spectrum shifts to lower energies as a consequence of polarization and it is thus necessary to avoid polarization in order not to lose the spectroscopic information. The severity of the effect (and the critical amount of flux) depends on the material, temperature and biasing electric potential. For hemispheric detectors no model or measurement has been found. It can be assumed, that thanks to the geometry and improved electron collection, polarization shall occur at higher fluxes compared to planar detectors.

Chapter 5
Monte-Carlo Simulations

To check and verify theory of gamma-ray interaction in detectors, numerical models are used. The problem of interaction of incoming photons with a train of events on the output (see section 3 for more details) is by its nature a statistical problem. It is interesting, that *Monte-Carlo methods*, a very popular tool of calculating integrals by the means of statistics (particles generated by a computer with a prescription law), directly apply to our model. In other words, whereas Monte-Carlo numerical methods are an indirect way to calculate integrals and other problems in mathematics, in the case of photon interaction and counting it is directly the model coming from the real world.

5.1 Theoretical background

Monte-Carlo methods use a large number of particles, randomly generated evaluation points called *particles* (individual photons in this case), to estimate the solution of a problem. Generated particles have to be statistically independent and identically distributed in a sense depending on the problem solved. In the case of gamma photons, isotropic or anisotropic rays under one deterministic angle are used for the simulation. The cloud of photons can either be generated at one point or identically distributed by the means of starting position at a space or subspace. The trajectory of generated photons is then calculated and those entering the detectors volume are further evaluated. This further evaluation considers the particle's energy and random numbers are used to decide which of the interaction mechanisms discussed above (in section 3.2) takes place, if any. Successive events are then simulated as well. At the end, a histogram of events at energies depending on the undergone interaction mechanism is shown as a result of the simulation. The number of initial particles (sample size) has to be large enough in order to increase statistical power of the test.

The key of all Monte-Carlo simulations is generation of random numbers. Ideally, a random number is purely stochastic and cannot be predicted by any means. A random number is generated from a statistical distribution and with growing sample size, this distribution is approximated by the sample set of the generated numbers. For generation of truly random numbers, hardware-circuits with stochastic behavior called *true random number generators* can be used [23]. In most cases, *pseudo-random* software-generated numbers are used. This is also the case in *Geant4*, a software suite developed in CERN, which I used for the simulations.

The most basic and commonly used pseudo-random generators are simply based on overflow (modulo operation) as shown by the standard *linear congruential generator* (LCG):

$$x_{n+1} = (Ax_n + B) \mod C,$$

where typical values of A, B, C are

$$\begin{aligned} A &= 1664525, \\ B &= 2^{32}, \\ C &= 1013904223 \end{aligned}$$

or similar with A large enough, B slightly smaller than the largest integer (depending on the architecture – 32-bit, 64-bit) and C is arbitrary (can be omitted). See [39] for the most popular values. The generated numbers can be than scaled by dividing by C to fit into the standard $(0, 1)$ interval.

The linear congruential algorithm is very efficient with minimal storage requirements (only the last generated value is needed).

Pseudo-random generators are periodic (although the period is large), efficient and provide repeatability for a given seed. They are therefore called with a prefix pseudo, standing for non-randomness in terms of its repeatability. The mentioned advantages make the pseudo-random generators very popular in the field of Monte-Carlo methods. Various techniques are used to improve LCG, many of such improved algorithms are available in the kernel of Geant4. The default generator is codenamed *HepJamesRandom* and uses results from an article of F. James [39]. The algorithm is a combination of a lagged Fibonacci sequence (with lags of 97 and 33, and operation "subtraction plus one, modulo one") and an "arithmetic sequence" (using subtraction). In comparison with the LCG, the algorithm is more memory-hungry (100 words versus 1 word for LCG), but its period is 2^{144} versus 2^{32} for LCG. See [39] for more details.

For other distributions *re-sampling methods* have to be used. However, my simulation used uniform distribution only. Re-sampling methods are therefore out of scope of this thesis and can be found in any standard book on statistics and random number generation.

5.2 Model

The model is built in the software package Geant4 from CERN. Geant4, as already mentioned, is a toolkit for the simulation of the passage of particles through matter. Its areas of application include high energy, nuclear and accelerator physics, as well as studies in medical and space science.

The model in Geant4 is built in a script by using special classes and functions. First, the outline of the matter itself is created, including its shape, dimensions and material properties. Materials can be defined based on its chemical compounds and then applied to any modeled element. One can also model surroundings of the main detector, such casing, walls, etc. In my case, bare $CeBr_3$ and CdZnTe crystal was modeled to keep the simulation simple and as fast as possible (length of the computation time).

5.3 Simulation results

Simulations were done for several combinations of sizes and materials including different geometries. Among the tested materials were the later selected $CeBr_3$ and CdTe (very similar to CdZnTe), then NaI(Tl) and $LaBr_3$. Symmetric geometries of detectors with 5 mm, 8 mm, 10 mm diameters as well as asymmetric 5 x 10 mm and 5 x 2.5 mm detectors were tested. The bare crystal was in some cases simulated with a simple thin aluminum housing encapsulating the detector.

The results of simulations for the materials and sizes later used in the project are shown in table 5.1. The table summarizes simulated parameters for different energies. The trend of deeper penetration and gamma-rays passing through the detector crystal can be seen at higher energies, where absorbed percentage of incoming particles scales down to few percent. Moreover, as seen in figure 2.3, gamma-rays with higher energy represent higher dose equivalent than low-energy particles. This is clearly visible on the estimated count rate listed in the table. In order to record a spectrum at $1\,\mathrm{Sv\,h^{-1}}$, a higher count rate is yielded for lower energies. In this thesis, ^{137}Cs 662 keV will always be used as a reference. On can directly see, though, that it is more difficult to obtain $1\,\mathrm{Sv\,h^{-1}}$ for 100 keV than for example 662 keV.

The presented count rates were estimated using the H*(10) fluence-to-dose conversion factors (see figure 2.3). That way a fluence incident on the detector (expressed in photons per unit area) area was calculated. The values had to be properly time-scaled to yield count rates in MHz. Unidirectional radiation incident on a known detector area was assumed and that way the final count rate was calculated. The area in case of an asymmetric crystal is not the same for all the direction and might therefore pose an inaccuracy in the estimation.

Another two parameters included in the table are the Peak-To-Total ratio and a ratio of peak area and Compton continuum, both expressed in percent. These values are, due to small sizes of the crystals, very low for energies over 1.5 MeV.

Material	Size	Energy [keV]	Absorbed [%]	Peak-To-Total [%]	Peak/Compt. area ratio [%]	Estim. count rate at 1 Sv h^{-1} [MHz]
$CeBr_3$	10 x 10 mm	30	99.87	99.71	34219.28	351.16
$CeBr_3$	10 x 10 mm	100	99.43	98.70	7586.92	452.78
$CeBr_3$	10 x 10 mm	300	48.51	52.96	112.59	74.86
$CeBr_3$	10 x 10 mm	600	32.24	20.51	25.81	26.03
$CeBr_3$	10 x 10 mm	800	28.22	14.28	16.66	17.90
$CeBr_3$	10 x 10 mm	1000	25.28	11.03	12.40	13.50
$CeBr_3$	10 x 10 mm	1500	21.05	7.05	7.59	8.35
$CeBr_3$	10 x 10 mm	2000	18.87	4.95	5.21	6.10
$CeBr_3$	10 x 10 mm	2500	17.60	3.66	3.80	-
$CeBr_3$	10 x 10 mm	3000	16.71	2.84	2.92	4.15
CdTe	5 x 2.5 mm	30	99.86	99.81	52317.64	43.89
CdTe	5 x 2.5 mm	70	99.69	99.22	12680.24	57.87
CdTe	5 x 2.5 mm	100	98.52	97.75	4350.10	56.08
CdTe	5 x 2.5 mm	200	59.55	77.88	352.08	17.23
CdTe	5 x 2.5 mm	400	28.29	34.54	52.77	4.13
CdTe	5 x 2.5 mm	600	21.34	17.76	21.60	2.15
CdTe	5 x 2.5 mm	800	18.10	11.28	12.71	1.43
CdTe	5 x 2.5 mm	1000	16.12	7.94	8.63	1.08
CdTe	5 x 2.5 mm	1500	13.20	4.01	4.18	0.65
CdTe	5 x 2.5 mm	2000	11.74	2.38	2.43	0.47
CdTe	5 x 2.5 mm	3000	10.67	0.87	0.87	0.33

Table 5.1: A list of parameters obtained from simulations in Geant4 (selected are only detectors relevant to the following experiments presented in this thesis).

5.4 Effects of the electronics

The simulation software Geant4 only simulates the core, i. e. the interaction of particles with matter. Therefore, the spectrum outputted from the simulation, always has an ultimately thin photopeak located exactly at the emission energy (662 keV for ^{137}Cs). This is however not the case in real measurement, where spectrum is blurred and flattened by electronic noise. The spectrum from Geant4 thus has "go through" this degradation system, which is simply done by convolving the spectrum with a function representing the noise. This is more discussed in section 7.1.1, where peak shapes are analyzed and described. In case of scintillators, a typical shape is Gaussian, whereas compound semiconductors usually exhibit an additional exponential tailing on the low-energy side of the photopeak.

A final convolved $CeBr_3$ spectrum of a 10 mm symmetric detector is presented in figure 5.1, where it is compared to real measurement. It must be noted, that it was not possible to perfectly simulate the detector including the source and the environment around. Counts at lower rates can thus come from backscattering, bremsstrahlung or florescence [62]. The simulated spectrum presented was convolved using a Gaussian function with an energy-variable FWHM

$$\mathrm{FWHM}(E) = \frac{160}{\sqrt{E}} \tag{5.1}$$

for energy E. This dependence was verified using several measurements in [65].

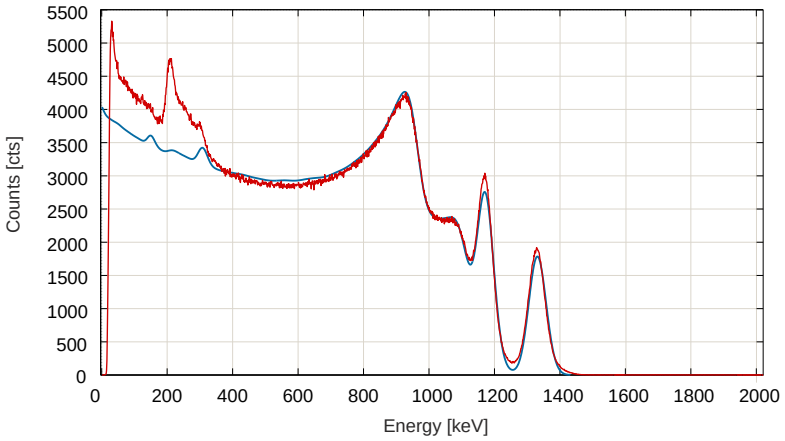

Figure 5.1: A comparison of the measured spectrum of ^{60}Co using the $CeBr_3$ detector and a simulated spectrum using Geant4, convolved using the FWHM relation from equation (5.1). The measured spectrum includes counts after a subtraction of the background.

.

Chapter 6
Experiment Design

6.1 Material selection

Considering important facts and limitations listed in section 4, fast scintillation materials with good resolution results (better than NaI(Tl)) were preferred. Additionally, no or little afterglow, stability, refractive index close to that of glass and high density were also important factors in decision making. From the price point of view, shaped NaI(Tl) crystals are 5-10 times cheaper than other popular scintillation materials. $LaBr_3$(Ce), $CeBr_3$ and YAP(Ce) crystals with PMT are at around the same price level – being still affordable, but not cheap. These new organic scintillation materials were also preferred, mostly thanks to their speed and resolution which is superior to that of NaI(Tl). On of the key plots for this purpose is in figure 4.2, where scintillation materials are compared.

Semiconductor technology offers even more options, but only a few are suitable for environmental monitoring. The detector shall not be bulky and power-consuming, cooling is not an option. Therefore, semiconductor detectors operating above room temperatures shall be used. As already mentioned in 4.3, this is decided by the material's key property – its band gap. Thus, materials suitable for our application include GaAs, CdTe and CdZnTe. All three materials have relatively high density (see table 4.4). All these materials suffer from a difference of hole and electron mobility, though, which influences quality of charge collection.

6.2 Detector size

The size of a detecting medium made of the materials discussed above (chapter 4) is a compromise between the spectrum quality (Peak-To-Total, Peak-To-Compton ratios) and ability to measure high doses. For larger sizes, the detector and its subsequent electronics is saturated by the amount of incoming pulses, overlapping each other and thus flattening or totally eliminating peaks in the spectrum. Small detectors, on the other hand, are not always commercially available (scintillation materials) and produce spectra of bad quality (assuming the range of 30 keV to 3 MeV).

As the simulations show (for more discussion about the size see chapter **??**), the "good" compromise is a detector of sizes larger than 5 mm, but smaller than 10 mm. That way, count rate produced by an incoming radiation in order of several tens of $mSv\,h^{-1}$ is in a sub-MHz range. The estimated count rates are shown in table 5.1. Such rates can still be processed and energy-analyzed in order to produce nice spectra.

The mentioned range of 30 keV to 3 MeV is a standard range recommended and often required in environmental radiation monitoring. Vast majority of the detectable nuclides, however, lie in lower part of this range (see plot 3.1). This is another important aspect justifying the suitability of small detector volumes for this type of application.

6.3 Available and affordable solutions

6.3.1 Commercially available CdTe and CdZnTe detectors

There are many tiny crystal solutions made from semiconductor materials available. However, it is actually a big manufacturing challenge to produce larger detectors, for example from CdZnTe. The market offers so-called pixelated crystal detectors (e. g. manufacturer ACRORAD in Japan), these are very small with a dimensions 5 x 5 mm, 10 x 10 mm, but usually very flat, with heights smaller than 1

mm. Such detectors are rather directional and not suitable for the purpose of environmental monitoring. The most suitable solutions offered on the market are small CZT detectors in either a planar geometry or a quasi-hemispheric geometry (discussed in section 4.3.2.2). These detectors are usually symmetric enough for the purpose of omni-directional radiation detection and their size is small enough. The most popular detectors of these types are: *Kromek CdZnTe GR1* (ready-to-use with MCA and all included), planar CdZnTe detector *SPEAR* from *EV Products* USA (5 x 5 x 5 mm^3 = 125 mm^3), *Eurorad* France with their small *SO8W* CdTe detector (quasi-hemispheric 65 mm^3 and other sizes), *Ritec* Latvia CdZnTe tiny detectors of different sizes (from 1 mm^3 to 1000 mm^3).

6.3.2 Commercially available scintillation detectors

In the field of scintillation detectors, not many "ready" solutions are commercially offered. The smallest photomultiplier tube from the world's famous manufacturer *Hamamatsu* has a diameter of 10 mm. Even though such PMT is available, scintillators of this size can only be manufactured upon request. Smaller sizes are practically impossible, the crystals has to be cut and only very few producers offer such custom designs. One of the few producers is in Netherlands, a company called *Scionix*, with a special small scintillation detector called a pen-type detector. Usually equipped with a 10 mm NaI(Tl) crystal, the company was able to reproduce the same solution with a $CeBr_3$ material, which they supply. Other interesting materials and custom designs on the market include: YAP(Ce) crystal with a minimum diameter of 8 mm can be manufactured by *Crytur* Czech Republic, $LaBr_3$(Ce) from Chinese suppliers (*Castech*, etc.) with a diameter of 10 mm (*Saint-Gobain* refuses to offer smaller sizes than 1 inch), YAP(Ce) and $LaBr_3$(Ce) of small sizes from a company *Oken* from Japan.

6.3.3 Selection of the detector

Thanks to the fact that current technology offers two suitable solutions for the task of spectrometric high dose measurement, it was decided to test one fast scintillation detector and one CdTe/CdZnTe detector. The material and size combination was considered based on simulations presented in chapter 5. Simulation results relevant for this selection are provided in table 5.1.

The choice of a scintillator was easier to decide and it resulted in a choice of the *Scionix* pen-type detector equipped with the promising $CeBr_3$ crystal. The complete package from *Scionix* included following:

- $CeBr_3$ crystal with a 10 mm diameter (785 mm),
- *Hamamatsu R1635* 10 mm PMT,
- aluminum casing incorporating the detector and the scintillator,
- *RG 174* cable with *LEMO 00* connectors.

The selection of a semiconductor detector was more complicated due to the fact that such detectors are available on the market from a number manufacturers. Although the CdTe material could yield somewhat better results, the offered volumes were too large. It was therefore decided to test a smaller detector with a quasi-hemispheric geometry (found to be performing better in section 4.3.2.2) from the company *Ritec* from Latvia. They produce different types of detectors encapsulated in aluminum or steel shielded casing. Of the available sizes (1.5, 6, 20, 60, 500, 1500 mm^3), we selected the 60 mm^3 detector *SDP 310/60* with a preamplifier built directly in the housing. There is another type of detector of the same volume without a preamplifier (*CZT/60*) and thanks to a loan agreement with the company Ritec, we were able to test both. Another preamplifier (*PA 101C*) was supplied to the second detector, so that the signal can be directly routed to MCA. The complete package of two detectors from *Ritec* included:

- detector CZT#1
  - CdZnTe quasi-hemispheric crystal 5 x 5 x 2.5 mm^3,
  - built-in preamplifier with a decay time of 75 µs;
- detector CZT#2
  - CdZnTe quasi-hemispheric crystal 5 x 5 x 2.5 mm^3,
  - standalone preamplifier *PA 101C* with a decay time of 50 µs.

Figure 6.1: The selected and tested tiny "pen" detectors. From the left: the $CeBr_3$ detector from *Scionix*, the CZT#1 detector from *Ritec* and the CZT#2 detector from *Ritec*.

6.4 Electronics

This part will now described the electronic components used to test the selected detectors. The detectors have to be supplied with high voltage and the measured spectra have to be read out using a combination of amplifiers and MCA.

6.4.1 Measurement chain

For all three detectors, the same base electronics was used. This was based on the *Envinet* SARA main hardware board. The board can be powered by a voltage in range of 8-17 V [69] and an MCA from a manufacturer *XIA* is integrated. There is also a convenient way of reading out the MCA over an included serial interface (RS232). SARA also offers internal storage of a spectrum, a feature that was not used in our case as the spectrum had always been read out using an external computer.

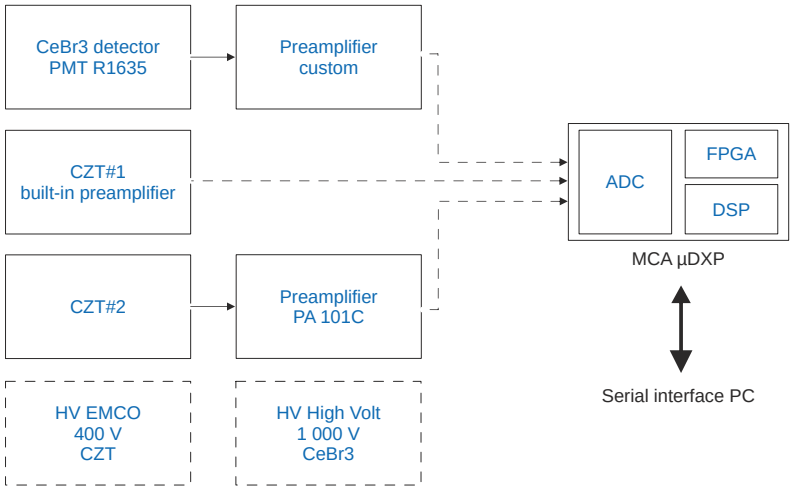

Figure 6.2: Block diagram of the measurement scheme.

The SARA board also posses an embedded HV module that can be set to output voltages ranging from 0 V to 1 kV. Two different modules were used in this case, a module named *C10* from *EMCO* and *HMA-1P1-12* from *HIGHVOLT*. Both modules operate with a maximal output power of 1 kW. Further information about the modules linearity and accuracy can be found on the manufacturer websites.

The SARA board was also equipped with digital MCAs from a company *XIA LLC*. The MCA is called *µDXP* and is as tiny as a credit card. Its power consumption is very low (500 mW) in comparison to similar products. Two options were available, either a 8 MHz version or a faster 16 MHz version with variable digital gain. For our purpose (high count rates), the faster 16 MHz µDXP with a sampling period of 62.5 ns was chosen with expectations that it might still not be fast enough for our application.

An important fact to note is that the µDXP input can only cope with voltages up to 5 V, but 3 V are recommended ([31]). Therefore, the preamplifier has to be designed in a way so that its output signal with event pulses does not exceed this limitation for the range of radiation events from 30 keV to 3 MeV.

A short overview of how µDXP works from a user point of view will now be presented. At first, a short list of the most important features and their meaning is provided (partially taken from [31]):

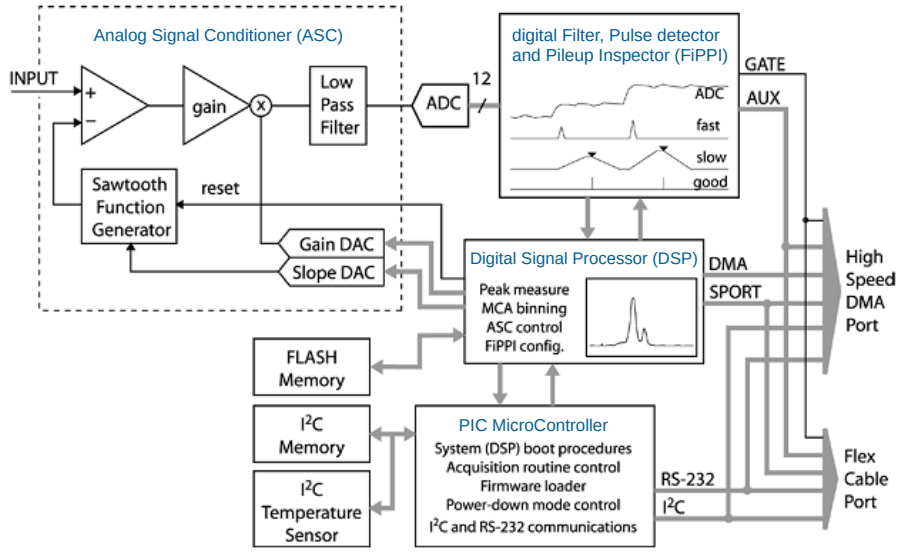

Figure 6.3: Block diagram of XIA's μDXP (taken from [31]).

- support of different preamplifiers (RC-type / reset-type) with different polarity and decay times (configurable with a bottom limit of 62.5 ns),
- multi-channel analysis of incoming pulses for up to 8196 channels with many configurable parameters (GENSET – number of bins, their width in channels, etc.),
- high throughput – *XIA* specifies it up to 328 000 counts s^{-1},
- digital trapezoidal filtering with programmable peaking times
- digitally controlled internal gain (pulse height amplification) of 32 dB and 16-bit precision,
- configurable pile-up inspection with a fast and slow filter (PARSET – configurable parameters),
- RS-232 interface and command set.

The μDXP contains three key hardware units: ADC, FPGA and DSP. The 12-bit ADC is used to sample the input signal (in our case at a 16 MHz rate). The DSP monitors the analog circuitry, manages spectrum scaling and binning, and carries out various high-level calculations. The FPGA is used for reconfigurable digital shaping, triggering, and pileup-rejection algorithms. An overview over its components is shown in figure 6.3. There are many tunable parameters of the μDXP that need to be correctly configured, the most important of them are listed in table 6.1. The table also shows values set in my case, in order to obtain a usable spectrum in the range of 30 keV to 3 MeV.

Parameter	CZT#1	CZT#2	$CeBr_3$
Base gain	1.5	2.3	1.0
Preamplifier	RC-type	RC-type	RC-type
Preamp. polarity	Negative	Positive	Negative
Preamp. decay time	100 µs	50 µs	various
Bin size	1 chn	1 chn	2 chns
Channels	8196	8196	8196
Trigger threshold	20	20	20
Peaking time	375 ns	375 ns	375 ns

Table 6.1: The most important parameters of the μDXP and values used.

There is a special measure of saturation of the pulse processor called *live time*. In comparison to *real time*, which is the time for which the measurement runs, live time expresses the time the μDXP is ready to detect input pulses. At higher count rates, μDXP cannot keep up with the exceptionally high rates (due to pulses being processed in FPGA, input out-of-ranges, etc.) and the live time is thus lower.

There are two types of pulse classification in μDXP. The first type are input pulses detected at the input, before processing and filtering them. These are called *fastpeaks* in the *XIA*'s datasheet, but let us call them input counts. The filtered counts occurring in spectrum do not have a name, so let us call them output counts. There are two very important parameters the μDXP provide along with the spectrum. First of them is the *input count rate* (ICR) and the second is *output count rate* (OCR). These are calculated in a following manner:

$$\mathrm{ICR} = \frac{\text{input counts}}{\text{livetime}}, \quad \mathrm{OCR} = \frac{\text{output counts}}{\text{realtime}}. \tag{6.1}$$

The input count rate is thus expected to be linear with rising dose rates up to higher values than the output count rate. The MCA provides all important parameters for calculating the OCR error and ICR can be corrected as well. This can be done using a model for ICR and OCR dependence on incident dose rate. This model is done based on a time-constant of the count rate called dead time. There are two types of dead times, one for the OCR correction and one for the ICR correction. I will further denote them as *input dead time* τ_i and *output dead time* τ_o. The dependence model is (assuming Poisson statistics [31])

$$\mathrm{ICR} = \mathrm{ICR}_{true} e^{-\mathrm{ICR}_{true}\tau_i}, \quad \mathrm{OCR} = \mathrm{ICR}_{true} e^{-\mathrm{ICR}_{true}\tau_o}. \tag{6.2}$$

It is not needed to use the equation to make first-order correction of the spectrum counts. Thanks to the fact that the μDXP provides both the measured ICR and OCR, the correction of counts can be done easily. For counts in a channel i, this is simply

$$N_{true,i} = \frac{\mathrm{ICR}}{\mathrm{OCR}} N_i. \tag{6.3}$$

That way, OCR correction is made by simply rescaling the spectrum. For more precise second-order corrections, the difference between the ICR and ICR_{true} has to be found. For that purpose, the model from (6.2) can be used. The unknown parameter that has to be found is the input dead time τ_i. The first equation in (6.2) can then be numerically inverted or the τ_i found using the model fit. When both the dead times are known, the models can be combined and a single correction model can be used with one dead time only.

The rescaling is done similar to the equation 6.3, but the calculated ICR_{true} is now used instead of the measured ICR. A short example of a calculation for values obtained in the case of one of the studied detectors will be presented in section 7.2.1.

The presented hardware including the SARA board with the μDXP was encapsulated in a plastic waterproof box, which was modified by drilling and assembling of 5 connectors: Fischer connector for power supply, SUB-D connector for the RS232 line, SHV connector for high voltage, BNC connector for signal and SUB-D connector for $\pm$12 V and ground. That way, all three detectors can be attached to the same board (although not at the same time). For the CdZnTe detectors, the HV module had to be swapped and a custom $\pm$12 V supply had to be turned on by a switch.

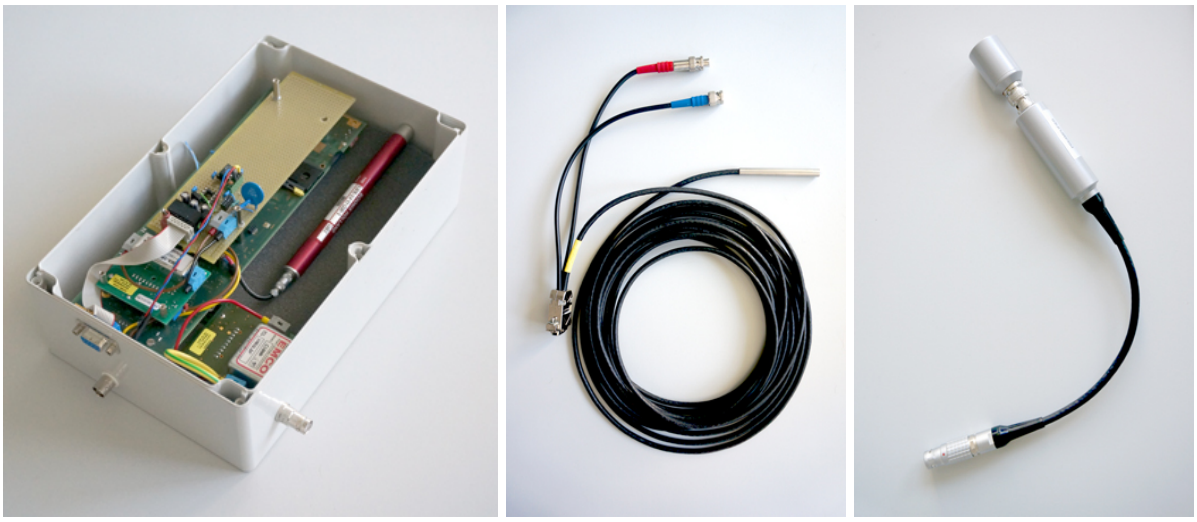

Figure 6.4: The electronics enclosed in a casing (the first picture) prepared for a connection of the three tested detectors (CZT#1 shown in the second picture and CZT#2 in the third).

6.4.2 Adjustments for the $CeBr_3$ detector

The $CeBr_3$ detector was supplied with a built-in voltage divider for dynodes of the photomultiplier tube. The total resistance is 3.63 MΩ, which is also the output impedance of the detector. The divider is the model *E1761-04* from *Hamamatsu* with a positive voltage design (negative voltage on the shielding and photocathode; positive on the anode, where the multiplied signal is collected). Its maximum voltage rating is 1500 V. However, our modules could only provide 1 kV, that is why the voltage of 1000 V was used (for all measurements).

The output signal at anode of the PMT is superposed to the high voltage input and has to be split up using a simple HV/Signal splitter, which is composed of one capacitor and one resistor. The splitter can be seen in figure 6.5 as a combination of a DC-blocking capacitor C4 and a HV resistor R3 (and R2). For stability, another capacitor C3 is added. A care must be taken where high voltage is present, and proper elements have to be selected (HV-rated capacitors).

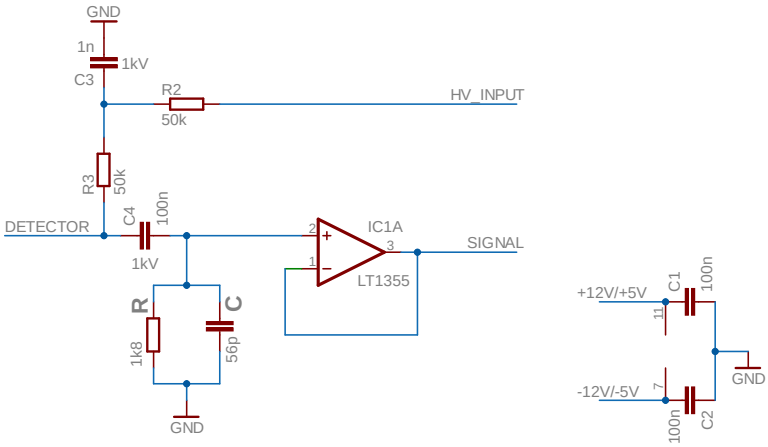

Figure 6.5: Preamplifier for the $CeBr_3$ detector signal collection. The main part is represented by the marked R and C.

The current-signal is collected and amplified using an active RC element (see figure 6.5). The output voltage amplitude of the signal and its decay time is set by the R and C shown in the schematic. Moreover, care must be taken not to choose too large capacitance in comparison to the splitter capacitor C4. And the resistors R2, R3 must be large, but not too large so that they influence the voltage (considering input resistance of the PMT voltage divider). The operational amplifier then drives the output of the preamplifier. The operational amplifier shall be fast enough, in this case a dual 12 MHz *LT1355* from *Linear Technology* was used with a slew rate of 400 V μs^{-1} and a relatively low supply current (1.25 mA per amplifier).

The signal output is then connected to the MCA input. Its typical amplitudes and decay times for a list of RC combinations are shown in table 6.2.

6.4.3 Adjustments for the CZT#1 detector

The CZT#1 detector has a built-in preamplifier and features three connectors. These were an SHV connector for high voltage supply, which was specified to 400 V, a D-SUB connector for preamplifier supply and a BNC connector for the output signal. The ±12 V supply was generated by a DC/DC converter *Traco TMR* on an external board mounted on the SARA board.

In order to make $CeBr_3$ and CZT detector swapping easier, two high voltage modules were used. The module from EMCO was programmed to 400 V and used for both the CZTs, whereas the second module was programmed to 1000 V for the higher voltage needed by PMT.

6.4.4 Adjustments for the CZT#2 detector

The CZT#2 was treated in a similar way as the first CZT detector. There was an external preamplifier from *Ritec* connected to the bare detector, but the input and output signals were compatible with the other detector. The bare detector also provided a possibility of attaching a custom preamplifier. This idea was abandoned after several attempts, mostly due to not being able to amplify the small generated charge (current) without noise. Even though I was able to obtain pulses from the detector, the signal was very noisy and could not serve any further. By inspection of the pulses, however, their short rise times

R Value	C Value	Measured Amplitude (Cs peak) [mV]	Measured Time Decay [ns]
1 kΩ	1 pF	-700	35
1 kΩ	33 pF	-480	75
1.8 kΩ	1 pF	-950	60
1.8 kΩ	3.3 pF	-900	50
1.8 kΩ	10 pF	-800	75
1.8 kΩ	33 pF	-510	102
10 kΩ	1 pF	-	270
10 kΩ	33 pF	-740	520
47 kΩ	33 pF	-750	2000
47 kΩ	220 pF	-210	6000
47 kΩ	1 nF	-50	18000
470 kΩ	1 pF	-1700	2000
470 kΩ	1 nF	-100	22000

Table 6.2: Tested RC networks for the $CeBr_3$ preamplifier.

of 10-20 ns were confirmed. Due to the noise sensitivity, a preamplifier for CZT detectors shall include a cascade of special low-noise operational amplifiers in a charge-sensing design.

6.5 Measurements – facts and limitations

Measuring irradiation of the detectors brought in several issues. The largest is the relativity of recorded counts in a spectrum. Whereas the standard crystals of larger diameters provide count numbers high enough counts in 5/10 minutes of measurement, small detectors tested in this thesis are unable to yield spectra with sufficient statistical significance. Therefore, the measurement time has to be extremely long or the irradiation has to be more intensive. It was not possible to move the irradiation levels with standard weak sources owned by *Envinet*, apart from placing them as close as possible to the detector medium. In order to get spectra with good resolution (high counts), the measurement had to run for several days. For the case of background-radiation measurements, the time had to be extremely long, more than a week.

Although facing the large measurement times, several spectra were measured with sources available in *Envinet*. Spectra for cesium, europium and background radiation were obtained that way.

Another important note to make is regarding statistical deviation of measurements provided in this thesis. The high dose rates obviously provide high recorded counts (several millions) and thus low statistical fluctuations. Therefore, measured data are presented without providing measurement deviations. The whole measurement chain is quite long and it is thus very difficult to investigate it in terms of measurement errors. That lead to concentrating on the nature of even counting only as the main source of measurement noise. A special care was thus taken to assure high number of counts in spectra used for further evaluation and data representation. This had to be mostly considered during the temperature tests, in which weak sources were used.

6.6 Measurement setup – radiation chamber

The radiation tests were done in a radiation facility in Munich. It is located in an institute for environment and health protection named *Helmholtz Zentrum*. Several radiation test benches are available in the Helmholtz center. The most important for the high radiation intensity test is a German secondary calibration chamber equipped with a Buchler device (*Buchler Gammakalibrator OB 20*) inside.

The radiation chamber is fully automated from the outside and well shielded by thick concrete walls. The radiation source (when activated – being outside of the lead container) is at a fixed position (see figure 6.7). The calibrated dose rate of either cesium ^{137}Cs or cobalt ^{60}Co gamma radiation is achieved by moving the detector mounted on a special trolley (see figure 6.6). The trolley is equipped with a hydraulic brake assuring it stays in its position. The position can be set with a millimeter precision.

Several sources of different radiation strength are available for both ^{60}Co and ^{137}Cs (see table 6.3). The maximum achievable dose rate for ^{137}Cs is thus around $10\,Sv\,h^{-1}$ when nearby the source (40-50 cm).

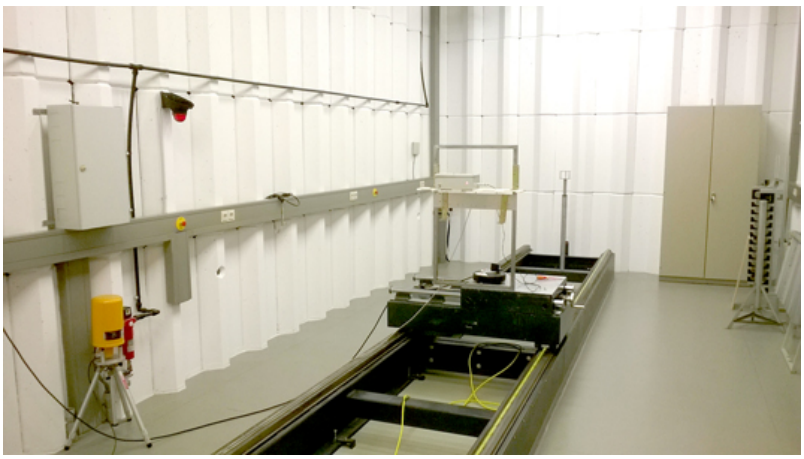

Figure 6.6: Gamma radiation calibration facility in Munich. The detector can be fixed onto a trolley shown in the picture.

For ^{60}Co it is approximately 100 mSv h^{-1}. It can also be seen from the table 6.3 that the sources provide roughly one decade measurement steps. This is convenient from a practical point of view, the user does not have to enter the room (chamber) every time and move the trolley in order to adjust the dose rate.

Nuclide	Source No.	Max. Dose Rate [µSv h^{-1}]*	Max. Dose Rate [mSv h^{-1}]*
^{137}Cs	1	1.89	0.00
^{137}Cs	2	20.49	0.02
^{137}Cs	3	194.42	0.19
^{137}Cs	4	1930.00	1.93
^{137}Cs	5	17390.00	17.39
^{137}Cs	6	185140.00	185.14
^{137}Cs	7	2276710.00	2276.71
^{60}Co	1	2.29	0.00
^{60}Co	2	19.98	0.02
^{60}Co	3	210.00	0.21
^{60}Co	4	2140.00	2.14
^{60}Co	5	22090.00	22.09

Table 6.3: Sources available in the Buchler radiation facility in Helmholtz Zentrum Munich, all data come from the local information sheet (*all values for the same distance of 100 cm).

Regarding the calibration of the Buchler facility, it is re-calibrated regularly, although no documentation is provided. However, according to the staff taking care of the facility, the best point where the dose rate is expected to be most precisely set by the means of radiation source strength and distance is at around 2 meters from the source. It is also clear, that although the radiation is collimated, it still results in a cone with small diameter at the source proximity and larger diameter at a larger distance from it.

For calculating dose rate at a given distance, a program developed specially for this workplace is used. It can either calculate distance for a given (required) dose rate or calculate dose rate from a distance. This can be done for every radiation source of the Buchler device (table 6.3).

6.7 Measurement setup – climatic chamber

All temperature tests focused on the detectors' temperature dependence and stability were done in a climatic chamber from a company *FEUTRON GmbH*. Various programs can be set up and used for different temperature cycles. The climatic chamber offers a wide range of temperatures and humidity combinations with a very good precision (see table 6.4).

The climatic chamber used also offers an option to pull cables through one of its walls. That enabled me to leave part of the electronics and computer outside at room temperature. Following measurements

Figure 6.7: The two pictures on the left show the source facility and placement of the detector onto a trolley in the radiation chamber in Munich. The right picture shows the climatic chamber used.

Property	Value
Temperature range	−75 to +180 °C
Climatic range	+10 to +95 °C
Temperature tolerance	±0.5 °C
Standard $\Delta T/\Delta t$	3 °C/min
Humidity range	10 to 98 % rel. hum.
Humidity tolerance	±3 % rel. hum.

Table 6.4: Technical specification of the climatic chamber from FEUTRON (taken from the manufacturer's website).

with different setups were used (values are in degrees Celsius):

- CZT#1 detector – detector with preamplifier inside
  - March 24-25: $0, -20, -40, -20, 0, +20, +40, +60$ *2h intervals*
  - March 27: $+60, +20$ *2h intervals, hot from previous test*
  - April 8-9: -40 (3h), $-30, -20, -10, +10, +20, +30, +40, +50, +60$ *2h intervals otherwise*
- CZT#2 detector – detector with preamplifier inside
  - March 25-26: $0, -20, -40$ (3h), $-20, 0, +20, +40$ (3h), $+60$ (3h) *2h intervals otherwise*
- $CeBr_3$ – detector with complete electronics inside
  - March 26-27: -40 (3h), $-20, 0, +20, +40$ (3h), $+60$ (3h) *2h intervals otherwise*

The long cable of CZT detectors supplied by *Ritec* allowed me to place the detectors inside, keeping the modified SARA board outside. That way only the detector and its preamplifier underwent temperature changes. For the $CeBr_3$ detector the situation was different and it was practically impossible to split preamplifier and detector and place them into the chamber alone. In this case, the whole case was placed inside the chamber, being read out by a computer outside. The humidity was left unset and unmonitored.

The intervals presented above contained periods of temperature changes of course and although the temperature capacity of the small detectors is small, it is not negligible. There was unfortunately no possibility to measure temperature inside the detectors, so another probe MIRA was placed inside the chamber as well. The MIRA is a probe of much larger dimensions, its temperature shall thus change more slowly than that of the tiny CZT or $CeBr_3$ detector. Temperature measured by MIRA in one of the tests is for illustration shown in figure 6.8. Another possibility to measure and check temperature is on the μDXP itself – this was used for $CeBr_3$ as in the case of other two detectors the SARA board with μDXP was kept outside of the chamber. The standard interval for which spectra were ignored was 30 minutes and thanks to the way of reading out the recorded data, it was possible to check if a steady state is achieved.

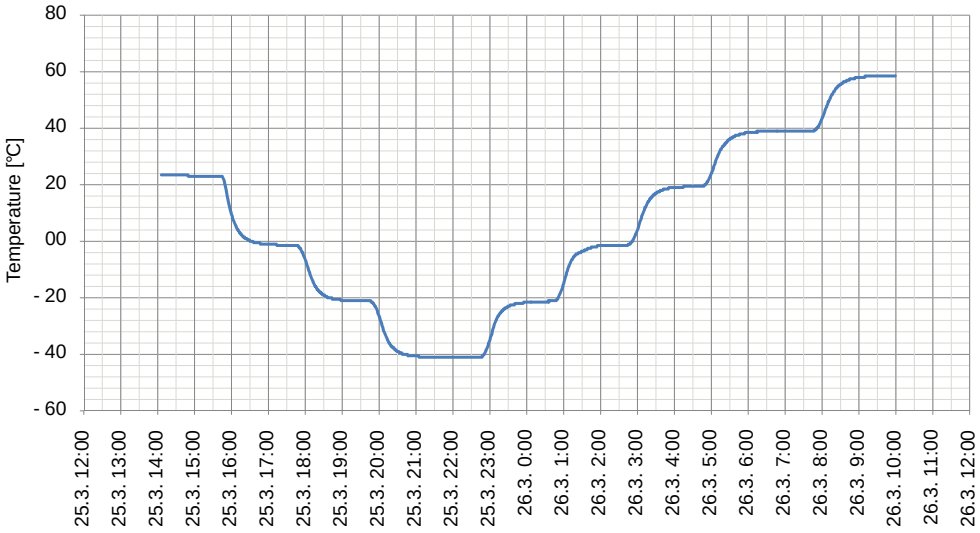

Figure 6.8: Temperature measured in the climatic chamber during one of the tests. This data comes from a gamma dose rate probe MIRA with a built-in temperature sensor.

The reading out of spectra was performed using the μDXP's serial interface and a PC with a serial port. A small program for communication using the μDXP's custom RS232 command set under Linux was written to automate the whole process. That way, 5-minute spectra were recorded in a cycle. This allowed for later possibility of checking whether the individual spectra change and if not, then summing the spectra together to obtain larger counts and thus higher statistical significance. Moreover, the program was used to obtain other basic information from the MCA like its temperature, input counts and filtered counts.

Unfortunately, some problems occurred with the communication and not all data were recorded successfully. Due to the fact that the measurements were scheduled overnight (cooling of the chamber is a very loud process), this caused loss of data for some measurements.

Chapter 7
Measurement Results

7.1 Spectrum quality

7.1.1 Shape and its fitting

The measured spectrum, in order to be useful, shall contain a number of counts that is large enough to be statistically significant. This can be accomplished by either high dose rates or long measurement times. After a spectrum is recorded, its analysis has to be done. This analysis mainly focuses on peak searching and fitting. The higher the peaks are relative to the background (Compton continuum, escape peaks and other noise), the easier it is to locate them. Ideally, we would like to see the peaks only and with the best resolution, meaning as thin as possible. As already mentioned, the properties of real detectors and subsequent electronics cause this ideal scenario not to be true.

In case of the $CeBr_3$ detector, the resulting shape is symmetric, of a Gaussian shape. Such a shape can easily be fitted using a custom-written script with the use of least squares minimization by fitting a function in the form

$$f(x) = ae^{-\frac{(x-x_p)^2}{2d^2}} + g(x), \tag{7.1}$$

where x_p is supposed to be the location of a peak, d its standard deviation, a its height and $g(x)$ is provided in case of a non-zero background. The function $g(x)$ can either be constant, linear or more complicated.

In case of the CdZnTe detector, a more complicated fit function has to be used, approximating the exponential tail on the low-energy side of the peak. Models presented in scientific papers discussing CZT shape fitting and publish used functions are usually based on physical background of the shape. The most frequent peak model is composed of three components: a short-term tail a long-term tail and a Gaussian part caused by the subsequent electronics [28]. It is very difficult to find a universal analytic function that would describe peak shape of all CZT detectors as reported in a technical description of a professional *Gamma Detector Response and Analysis Software (GADRAS)* [51]. Even in my case with 2 detectors only, their peak shapes differ dramatically. Whereas the CZT#2 detector's peak shape contains both the short and long low-energy tails, the CZT#1 seem to contain a single exponential tail only. The article [28] uses the same model, but omits the second component, which is mentioned as optional in [60]. This model (assuming no background counts) is analytically expressed as:

$$f(x) = f_0 \left(e^{-\alpha(x-x_p)^2} + T(x) \right), \tag{7.2}$$

where $T(x)$ is controlled by a binary parameter δ:

$$T(x) = \left(ae^{b(x-x_p)} + ce^{d(x-x_p)} \right) \left(1 - e^{-\beta(x-x_p)^2} \right) \delta, \tag{7.3}$$

where $f_0, x_p, \alpha, \beta, a, b, c, d$ are unknown constants. The second exponential function $ce^{d(x-x_p)}$ is optional and can be omitted. However, in some cases, it allow better fit for functions incorporating a broken exponential tail. A comparison of a two-component tail fit and a single-component fit of a measured CZT#2 ^{137}Cs peak is shown on the left of figure 7.1.

For the CZT#1 detector, a simple mixed function in the form

$$f(x) = \begin{cases} Ae^{a(x-x_p)} + Be^{b(x-x_p)^2} + c(x-x_e) & \text{if } x < x_p, \\ e^{b(x-x_p)^2} + c(x-x_e) & \text{if } x \geq x_p. \end{cases} \tag{7.4}$$

with fixed mixing coefficients $A = 0.7, B = 0.3$ was found to be working sufficiently in terms of goodness-of-fit (see figure 7.1). The function incorporates a linear component expressing the background counts under the peak. The same linear background model was also used for equations (7.2), (7.3).

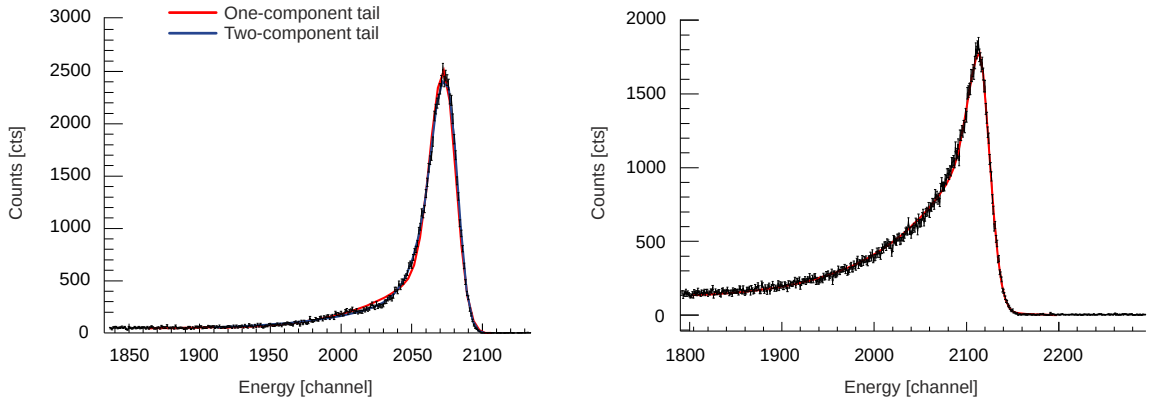

Figure 7.1: The left plot shows a fit of the ^{137}Cs peak of the CZT#2 detector – here two fits are shown, one with both exponential components and the other with on component in the low-energy tail. The right plot shows the ^{137}Cs peak of the CZT#1 detector, which had different shape. This shape was fitted using a function described by the equation (7.4).

7.1.2 Qualitative parameters

Several different parameters are used to characterize quality of a spectrum. A list of the most important ones is presented in section 3.8. Measurements results will be compared by the following three parameters characterizing peaks in the spectrum:

- Peak Area – total counts recorded in the peak,
- Peak Location – top of the peak location (mean for a Gaussian shape),
- FWHM – full width at half maximum of the peak (from a fit).

These qualitative parameters can be calculated in a number of ways either directly from the recorded spectrum or indirectly using a fit of it (mentioned in section 7.1.1).

In order to estimate peak area, the function in equation (7.1) has to be analytically treated to get FWHM, which is then

$$2\sqrt{2\ln 2}\,d = 2.3548\,d. \tag{7.5}$$

Such an ability to fit Gaussian peaks and estimate its parameters (from section **??**) is provided for example by an application called *Cambio* [46]. Cambio is a very good tool for peak fitting and provides many features such as calibration (calculating energy), peak parameter estimation including FWHM and others.

To verify the parameters obtained using Cambio, manual estimation of peak areas A was used. This is simply the sum of counts in what seems to be a peak area with a background subtracted from it. The background was linearly approximated by comparing values on the left and right of the peak. The exact formula for calculation is then

$$A = \sum_{x=x_s}^{x_e} y(x) - (x_s - x_e)\,\frac{1}{4e}\left(\sum_{x=x_s-e}^{x_s+e} y(x) - \sum_{x=x_e-e}^{x_e+e} y(x)\right), \tag{7.6}$$

where x_s and x_e are start (the leftmost) and end (the rightmost) channels of a peak, $y(x)$ is a number of counts recorded in channel x and e (a number of channels) serves for smoothing (averages taken instead of single points). This way of calculating area was compared with that of Cambio and the match is satisfactory (e. g. see figure 7.10).

Manual estimation from the recorded spectra was also used for the FWHM parameter. In this case, a peak maximum was estimated by an average of the top values, which was used to subtract the average background value in the interval of the peak. Then, a difference at half of this result (number of channels) was used to calculate FWHM in percent.

For evaluation and results presentation, manual estimations well as estimates calculated by Cambio were used. For CdZnTe peak shape with low-energy tailing the Cambio-calculated parameters were found to be incorrect, especially for the peak area estimate. The fitting of CZT peaks seems to be supported, although not working very well. It is satisfactory in terms of estimating parameters like peak location, width or trends in peak area or height. However, the absolute values are not correct, at least not for the peak area (figures 7.9 and 7.15 are demonstrating this effect).

7.2 Dose rate tests

A care was taken to measure in such steps that the whole dynamic range of the detector is covered, moreover that are close to each other to maximize gained information and to have good data for subsequent plots. On the other hand, the steps have to be distanced enough to reduce measurement time to minimum due to the limited access to the facility. At first, the dynamic range was scanned by testing different combinations of sources and distances. After the approximate upper limit of the dynamic range was found, a measurement schedule in a logarithmic sense was made. That way, approximately following decades were used:

- ^{137}Cs (distance 453 cm): 10 µSv h^{-1}, 100 µSv h^{-1}, 1 mSv h^{-1}, 10 mSv h^{-1}, 100 mSv h^{-1};
- ^{137}Cs (distance 311 cm): 20 µSv h^{-1}, 200 µSv h^{-1}, 2 mSv h^{-1}, 20 mSv h^{-1}, 200 mSv h^{-1};
- ^{137}Cs (distance 192 cm): 50 µSv h^{-1}, 500 µSv h^{-1}, 5 mSv h^{-1}, 50 mSv h^{-1}, 500 mSv h^{-1};
- ^{60}Co (distance 145 cm): 10 µSv h^{-1}, 100 µSv h^{-1}, 1 mSv h^{-1}, 10 mSv h^{-1}.

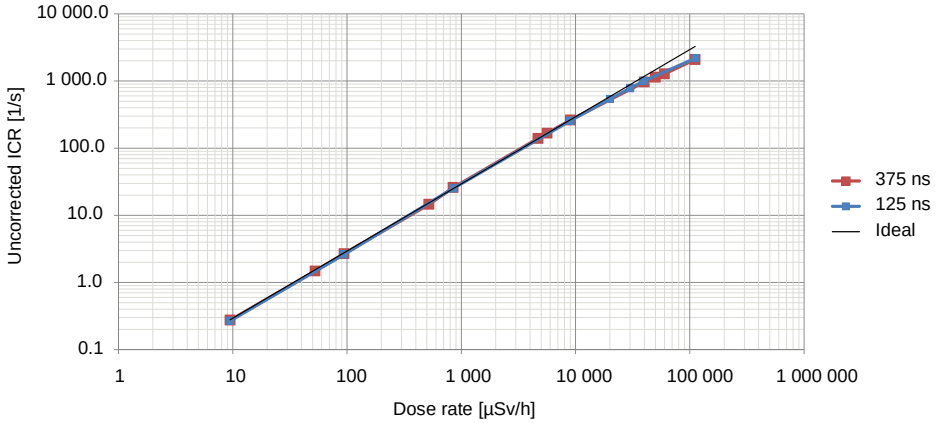

Figure 7.2: $CeBr_3$ detector. The plot shows input count rate of the detector (identified pulses before their filtering) for two preamplifiers (decay times in MCA set to 125 and 375 ns). Dead time influence of the detector can be seen at higher rates.

Later on, the upper dynamic range of the detector, where saturation in terms of pile-up and non-linearities take place, was measured more thoroughly to compensate for missing measurement points in this area. The ^{60}Co sources, however, were not strong enough to provide dose rate equivalents over 10 mSv h^{-1} with a sufficient accuracy. The highest possible dose rate equivalent for ^{60}Co was 100 mSv h^{-1} at a distance of 48 cm only!

The most important results of the measurements are shown in figures following in the text. An important thing to be noted is that all dose rate values are actually dose rate equivalents expressed in the H*(10) convention (defined in section 2.3).

7.2.1 Count rate

A dependence of the input count rate on the dose rate is shown for the $CeBr_3$ detector in figure 7.2 and for the CZT#1 detector in figure 7.3. The measurements are presented separately and an ideal case of a perfect detector is provided for comparison as well as comparison of different setups and measurements. The plot for the $CeBr_3$ (figure 7.3) shows very little difference for different decay times used (modified preamplifier and MCA settings). To summarize the definition from equation 6.1, the input count rate (ICR) is the number of detected input pulses (candidates for the spectrum) per second. These are then

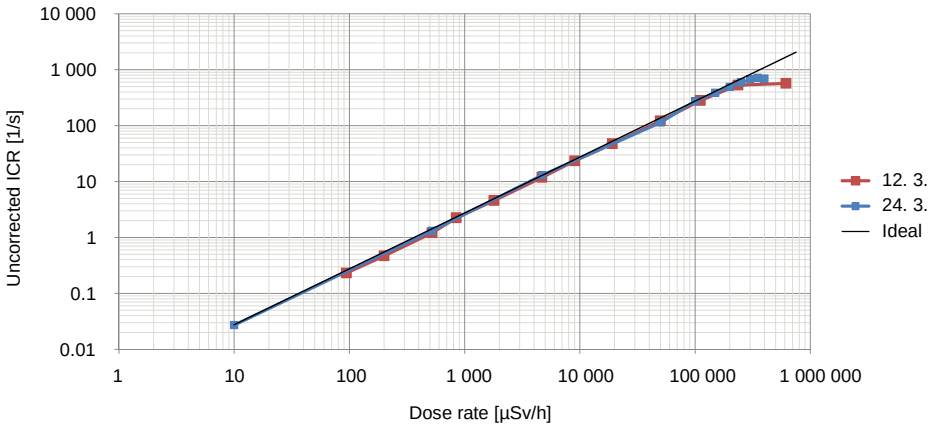

Figure 7.3: CZT#1 detector. The input count rate (detected peaks before their filtering) shall be linearly proportional to dose rate, but in reality, there is a deviation at higher dose rates due to the dead time effects of the MCA. Shown for two measurements conducted on different dates.

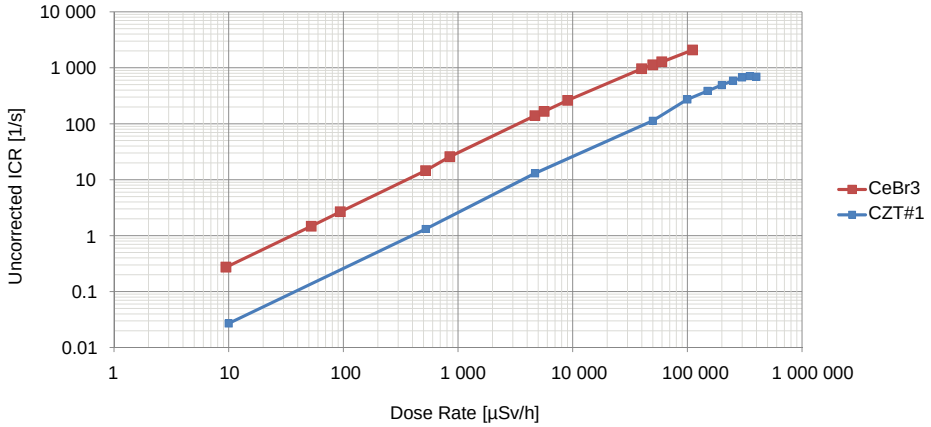

Figure 7.4: Comparison of the $CeBr_3$ and CZT#1 detector. The input count rate is near to linear except extremely high dose rates. The CZT#1 of smaller size has lower sensitivity and produces fewer counts in comparison to the $CeBr_3$ detector.

inspected and filtered, pile-up inspection is conducted, and the pulses left are then used for the final spectrum. The filtered pulses per second are then the output count rate (OCR).

A comparison of input count rates for the two detector types is shown in figure 7.4. As expected, the ICR of the smaller (in size) CZT#1 detector is smaller, than that of the $CeBr_3$ detector.

7.2.1.1 Correction

The OCR can be easily corrected thanks to the MCA features to compensate for piled-up pulses thrown away and similar actions occurring at higher dose rates. Moreover, for better precision and higher rates, ICR corrections have to be done as well. I will now show a correction example, where time constants related to the ICR/OCR model will be estimated for the $CeBr_3$ detector. Using the relations summarized in section 6.4.1 and the fact that the OCR model (in equation (6.1)) maximum found using elementary differentiation is

$$\mathrm{OCR}_{max} = \frac{1}{e\tau_o} = \frac{0.37}{\tau_o}, \tag{7.7}$$

it can be calculated, that the output dead time constant is equal to

$$\tau_o = 1.3\,\mu\mathrm{s}. \tag{7.8}$$

The input dead time constant is more difficult to calculate, since the model's maximum has not been reached in the measurements. In figure 7.2 only a little difference between the measured and true (ideal)

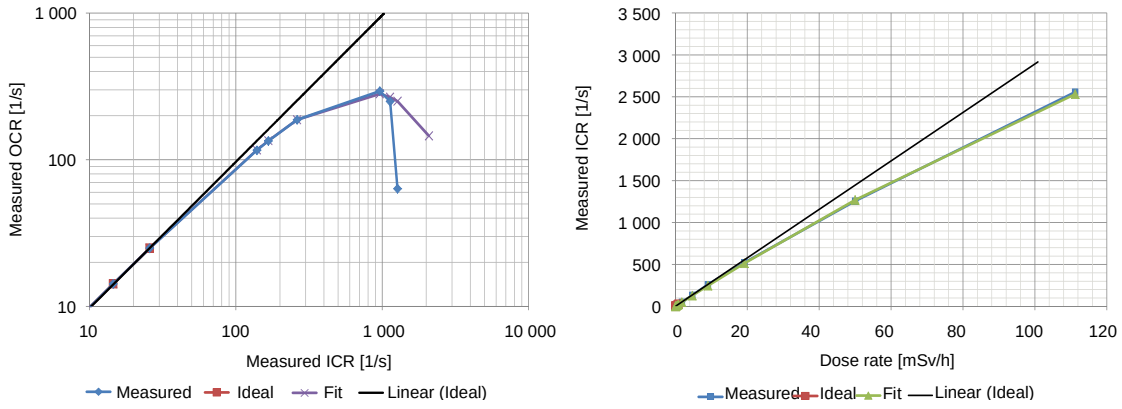

Figure 7.5: $CeBr_3$ detector. Models approximating the measured OCR (left) and ICR (right) dependence. This serves for dead-time corrections of the resulting spectrum.

ICR is seen. I obtained the constant τ_i using a fit in form of the model described by the equation (6.1). This fit, plotted in figure 7.5, yielded a time constant of

$$\tau_i = 4\,\text{ns}, \tag{7.9}$$

a very small value justifying the small difference in the true input count rate and the one measured by μDXP.

7.2.1.2 Comparison with simulations

The estimated values presented in table 5.1, where count rate was estimated using the H*(10) dose rate conversion factors and the simulated absorption probability at different energy levels. The estimated value for ^{137}Cs lies around 23 MHz for 1 Sv h^{-1}. For 10 mSv h^{-1}, the estimation can then be scaled to 235 kHz. The measured value for the same dose rate was 280 kHz. For the CZT#1, the estimate of 20 kHz is comparable with the measured 26 kHz. It must be noted, that the estimate is strongly dependent on the geometry of the detector and the area irradiated by the incident gamma-rays (see section 5.3 for more details).

7.2.2 Peak location

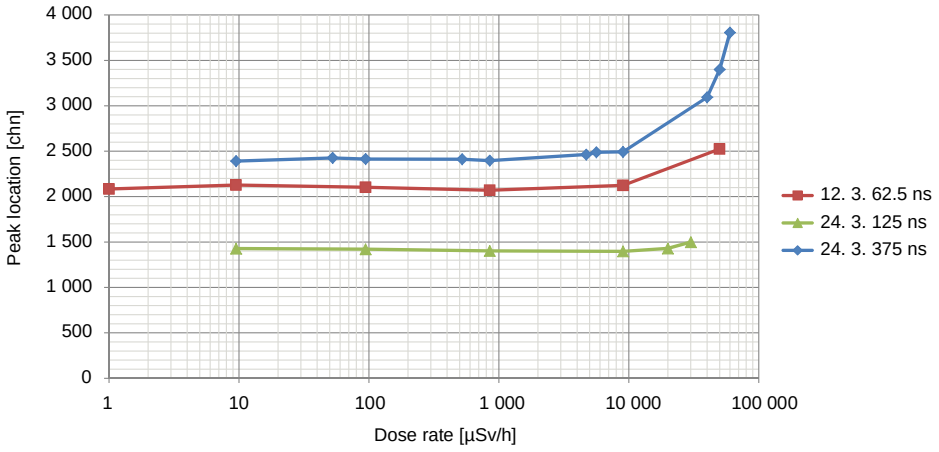

Figure 7.6: $CeBr_3$ detector. The peak location (its mean) shifts its position with increasing dose rate. The dependence is close to linear (please note that a logarithmic scale on the horizontal axis is used). Presented by three measurement, each with different setting of decay time in the MCA.

Another important result is how (not only) the ^{137}Cs peak shifts with increasing dose rate. This can be expressed as a channel where the location of peak mean takes place. For the $CeBr_3$ detector in figure 7.6, three different measurements with different settings are shown. The character of the dependence on dose rates is however same for all three. Using the logarithmic scale, a care must be taken not to misinterpret the results – the dependence is approximately linear, although it is exponential in the logarithmic sense.

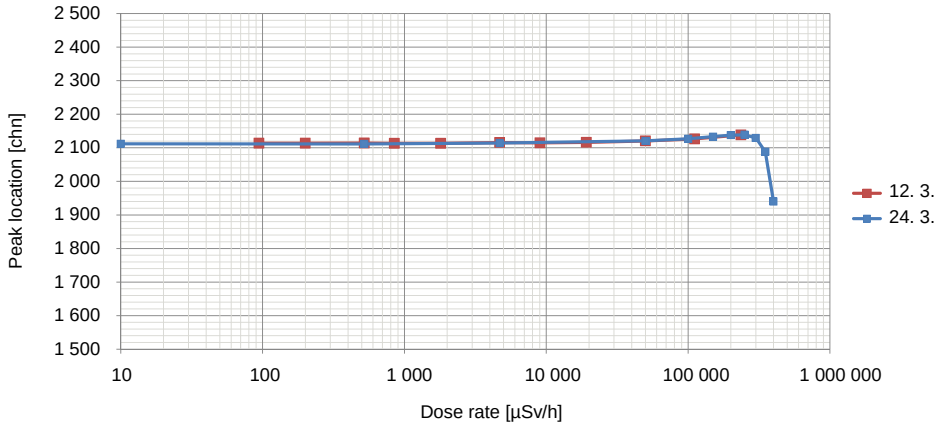

Figure 7.7: CZT#1 detector. The peak location of ^{137}Cs shifts with dose rate.

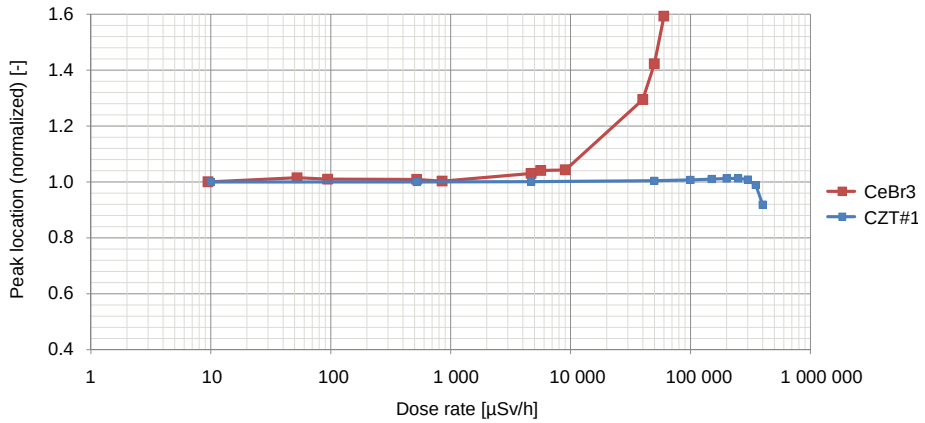

Figure 7.8: Comparison of the $CeBr_3$ and CZT#1 detector. The photopeak location shift is normalized to 1 at $10\,\mu Sv\,h^{-1}$. The peak shift in the detectors is very different, both by its direction and its relative amplitude.

Ideally, it should be a flat line independent from dose rate. The same property is plotted for the CZT#1 detector as shown in figure 7.7.

Different behavior of the two detector types is shown in figure 7.8, where ^{137}Cs peak locations are normalized. Whereas CZT stays on the same level (almost no shift) even when high count rates are reached, the $CeBr_3$ detector experiences large shift up to 50 %, and in the opposite direction than in the CZT case.

7.2.3 Resolution and peak sensitivity

Another very important parameter defining the spectrum quality is the peak sensitivity. Naturally, the number of counts in the peak (peak area) declines at high count rates. This is caused by non-linear phenomena occurring in the signal (pile-up, MCA limitations, high currents). The peaks get flattened and wider and a background "noise" is present. The peak is then superposed to this background (can be seen in figure 7.22). This background are actually mostly counts, that should belong to the peak area, but are unfortunately scattered all around. All these aspects make the peak lose its area in favor of the noise. Figure 7.10 shows such phenomenon for the $CeBr_3$ detector, where different preamplifiers and settings were used. As already mentioned in section 7.1.1, I experienced some issues with fitting spectra using the Cambio software, therefore a comparison of hand-fitted and Cambio-fitted peak areas are presented (see figure 7.9). Not a perfect match of these curves is observed, the CZT detector seem to experience fitting problems (where hand fits and custom script fits for peak areas were used).

Close to the sense of peak area, another important parameter FWHM (full width at half maximum) describing the peak width from the measurements is used. It is standardly measured for a ^{137}Cs peak at room temperature. Same as the area, the peak width increases with the dose rate.

In absolute values, the CZT yields much better resolutions in terms of FWHM. This is relative though,

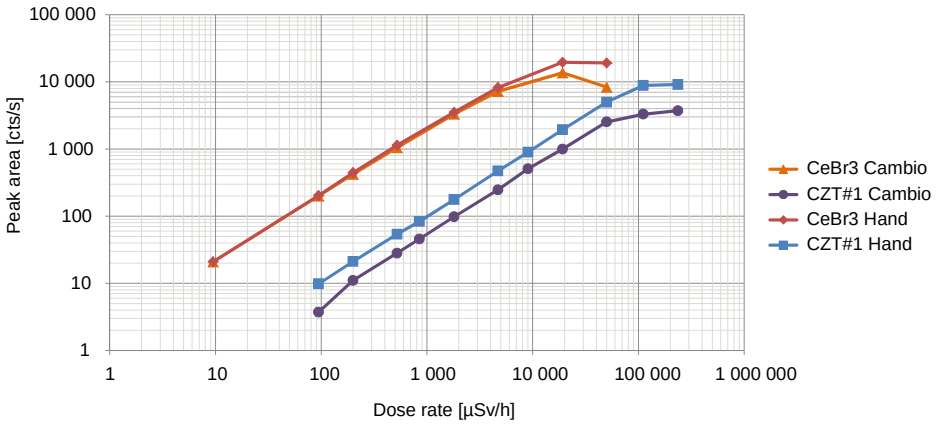

Figure 7.9: $CeBr_3$ and CZT#1 detector. Peak area per unit time dose rate dependence. Comparison of both detector types (smaller size results in smaller sensitivity). Comparison of hand and Cambio area calculation.

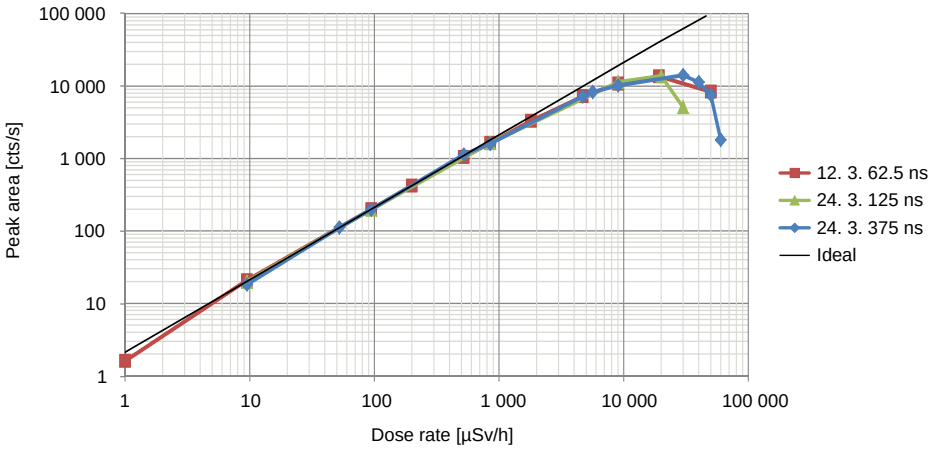

Figure 7.10: $CeBr_3$ detector. Peak area per unit time dose rate dependence. Peak area was calculated by Cambio. Comparison of measurements done on different dates and with different preamplifiers. Comparison with an ideal area (calculated from non-saturated values). The decay time shown is the decay time set in the MCA.

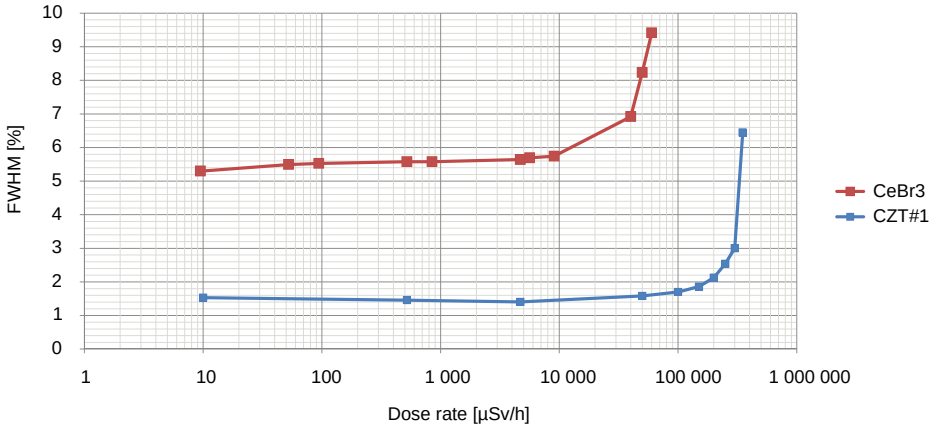

Figure 7.11: Comparison of the $CeBr_3$ and CZT#1 detector. The ^{137}Cs peak width changes with dose rate and, as the comparison show, the CZT#1 detector performs better in terms of relative widening and absolute values.

as it expresses the width at half maximum and significantly favors the CZT, which has a non-Gaussian distribution and it is wider at lower amplitudes. This low-energy tailing which widens the peak at its

bottom must not be neglected and therefore this difference in spectra shape needs to be taken into account (see their comparison in figure 7.3). Moreover, specific to the application of the spectrum, one shall realize how a spectrum for mixed nuclides would look like and if it is acceptable, to use the non-Gaussian shape information for peak identification.

In relative values, the CZT also performs better. The measured difference for the CZT#1 was found to be smaller in a wider range of dose rates than for the $CeBr_3$. A plot containing both can be seen in figure 7.11.

7.2.4 Discussion for $CeBr_3$

Thanks to the fact that the preamplifier for this detector was custom-made on a small additional circuit board, a test of different designs of the RC network could be done. Larger decay times result in lower achievable dose rates (upper limit of the dynamic range), but interestingly, too short pulses result in the same. This phenomenon seem to originate in the digital way of processing the signal. The MCA used was limited by a 16 MHz clock and according to its reference manual ([31]), the minimum pulse length of an input signal shall be 100 ns. The optimum was found around this value as well. For example, the decay time of 60 ns was performing almost the same (or only a slightly worse) as the decay time of 500 ns in terms of the highest achieved rates.

The highest achieved rates with an acceptable spectrum shape (for Cs^{137}) were around 50 mSv h^{-1}. At 60 mSv h^{-1}, the spectrum was too blurred with a very bad resolution.

7.2.5 Discussion for CdZnTe

The two CdZnTe detectors were found to be very different. This could be seen in the dose rate tests, where the CZT#2 detector could not withstand higher rates. In case of a cesium source, the detected peak broadens or even splits at higher rates (see figure 7.12). This phenomenon was observed for values over 50 mSv h^{-1}. For that reason, CZT#2 had been excluded from further discussion and comparison with other detectors.

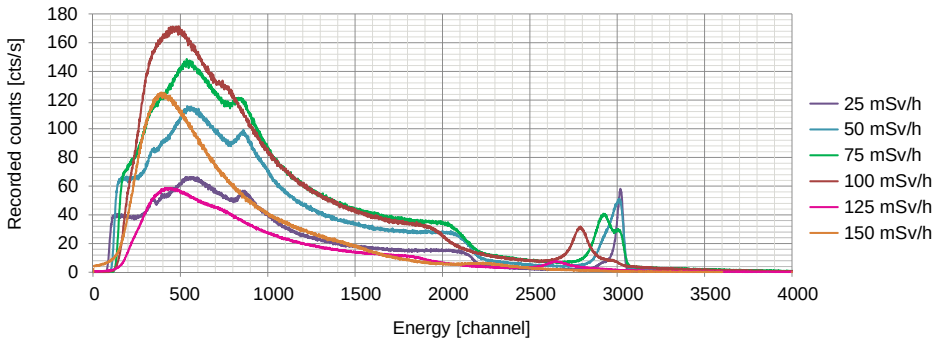

Figure 7.12: Dose rate dependence of energy spectrum measured for ^{137}Cs at higher rates. The spectrum is highly degraded for values over 50 mSv h^{-1}. The data come from 3-minute measurements with CZT#2.

The dose rate dependence even seemed not to be constant over time for the CZT#2 detector – the peak shape and thus resolution got worse by a longer radiation exposition. From the measurements it seems, that the detector works "correctly" only in the first few microseconds after its initial moment of irradiation. After this time, the spectrum gradually degrades and eventually, a steady-state spectrum similar to that shown in figure 7.13 are measured. This degradation of spectrometric performance is shown in figure 7.13, where spectra measured immediately after the source deployment and spectra measured after some time (10 seconds and more) are compared. Since this effect was observed ad-hoc, no accurate tools could be used to further analyze and precisely measure this phenomenon. The presented figure is therefore intended only for illustration purposes.

There were similar issues during temperature tests (see figure 7.19). The encountered issues might be related to charge trapping, and thus polarization induced by uncollected charge carriers (to be further discussed in section 7.3.5).

On the other hand, the CZT#1 detector performed overwhelmingly well. The observed ^{137}Cs peak was dominant for up to 350-400 mSv h^{-1} depending on the MCA settings and its filter settings. For dose rates between 350-500 mSv h^{-1}, the Cs^{137} peak presence was very sensitive to the MCA settings, but it still could be made recognizable. Even higher dose rates resulted in noise only. Further limitations could be incurred by too long decay times of the preamplifier and speed of the digital processor (16-megahertz μDXP). There was no sign of the phenomena observed in the second CZT detector.

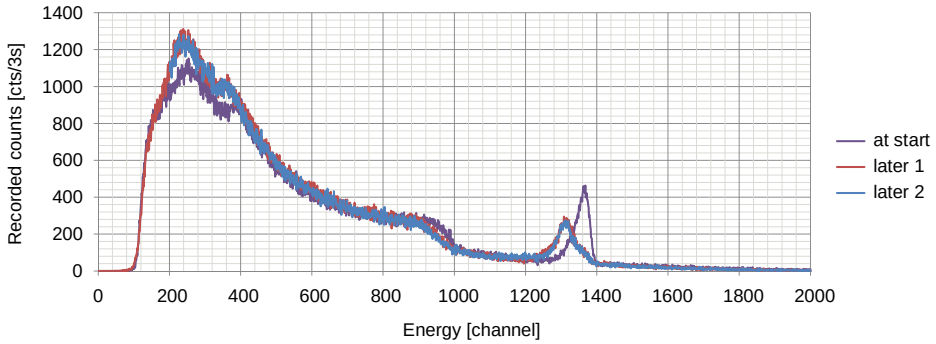

Figure 7.13: Time dependence measured for ^{137}Cs at a dose rate of 100 mSv h^{-1}. Similar behavior was observed for dose rates over 50 mSv h^{-1}. The measurement marked start was performed right after the source deployment, the other two then later on. The time was, however, not measured and the plot is thus presented for illustration only.

The preamplifier outputs for both the CZT#1 and CZT#2 detectors can be seen in figure 3.13, measured at a dose rate of 111 mSv h^{-1}. This dose rate already poses a strong pile-up, but in this case still in the dynamic range of the MCA input.

7.3 Temperature tests

7.3.1 Count rate and peak area

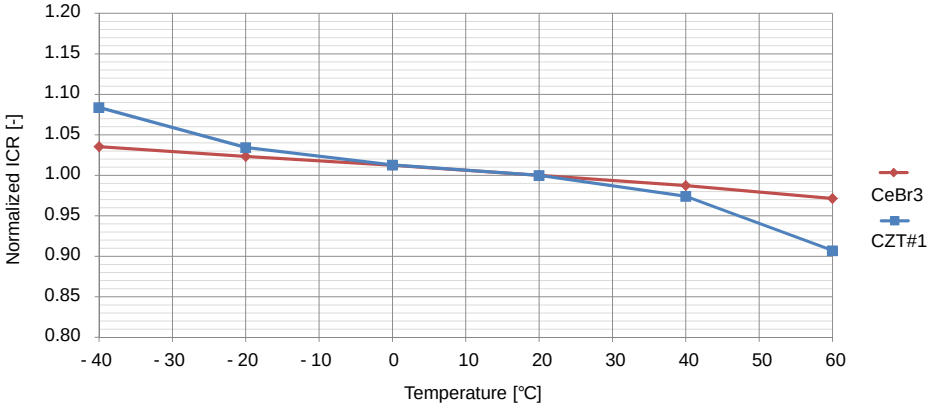

Figure 7.14: Comparison of the $CeBr_3$ and CZT#1 detector. The input count rate of the detectors changes with temperature. The data are normalized to 20 degrees Celsius. Statistical deviation is negligible thanks to the high amount of total counts ($> 5 \times 10^6$ for $CeBr_3$ and $> 2.4 \times 10^5$ for CZT#1) collected for each measurement point.

Temperate tests showed input count rate dependence of both detectors on the temperature. Reducing the temperature causes the input count rate to rise, whereas increasing the temperature results in slightly smaller number of recorded counts per second. The observed dependence is plotted in figure 7.14 for both the $CeBr_3$ and the CZT#1 detector. This effect naturally influences the whole number of collected counts (total area) as well as the counts present in the photopeak. The peak areas scaled by the coefficients of the ICR dependence were found to be constant for the whole range of measured temperatures. Although the peak area remained the same throughout the tests, its shape changed. This is presented in the next paragraph.

7.3.2 Peak width

As expected, the peak width tends to grow with rising temperature. A comparison of the two detector types is shown in figure 7.15. Whereas the $CeBr_3$ detector including its electronics follows a clear trend as its FWHM rises along the whole range from -40 to $+60$ degrees Celsius, the CZT#1 exhibits a different behavior. As expected, its temperature dependence is exponential (equation (4.1) in section

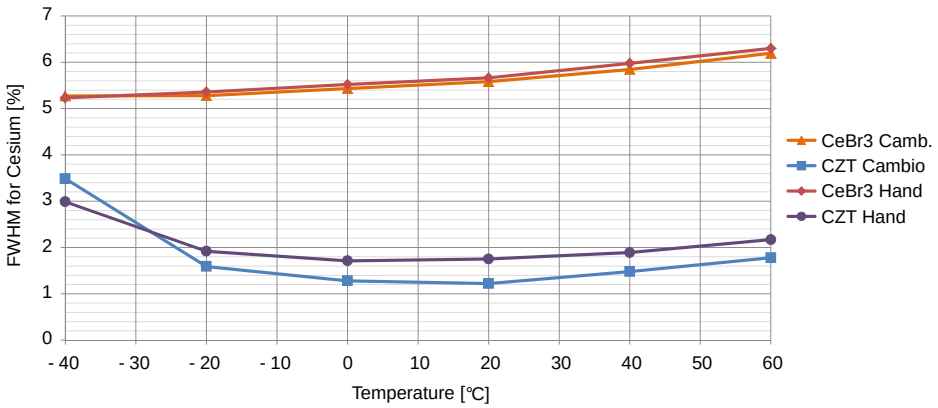

Figure 7.15: Comparison of the $CeBr_3$ and CZT#1 detector. The FWHM of the ^{137}Cs peak grows with raising temperature as expected. A slight difference in the FWHM value can be seen for hand estimate and Cambio function fit estimate.

4.3), but its influence on the resulting spectrum is not as apparent, as it was thought it would be. This surprise is followed by another one: the detector exhibits larger values of FWHM for lower temperatures. Moreover, the shape of the peaks is completely different, more of a Gaussian form (see figure 7.18, where comparison of CZT#1 spectra for different temperatures is shown). This effect will further be elaborated in the following sections.

There are two types of FWHM calculations I used. These are compared in the same figure 7.15 as well. The first type is using a Cambio fitted function and its "analytic" parameter estimate, the second type is using the raw data and calculating FWHM by its definition by hand. The results match quite well, only the CZT fit caused slightly different values as already discussed in sections 7.1.1 and 7.1.2.

7.3.3 Peak location

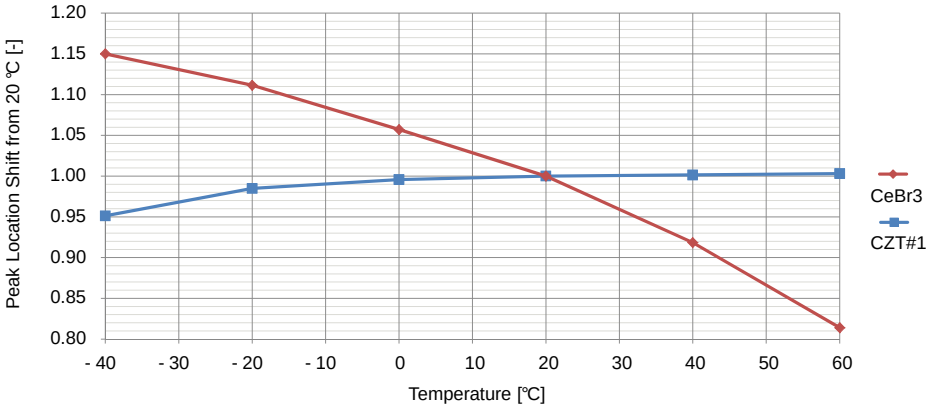

Figure 7.16: Comparison of the $CeBr_3$ and CZT#1 detector. The location of the ^{137}Cs peak's maximum shifts with varying temperature. The data come from spectra with sufficient number of counts ($> 5 \times 10^6$ for $CeBr_3$ and $> 2.4 \times 10^5$ for CZT#1).

Another important phenomenon that can be observed in the spectrum with varying temperature is its shift (in terms of energy scale). The whole spectrum either shrinks or expands towards higher energies. From the experiments made, spectra were collected and peak locations were estimated for ^{60}Co and ^{137}Cs using function peak fits in Cambio. Results presented are for cesium only, since it satisfactorily represents the whole spectrum shrinkage or expansion. These results are presented in the form of a normalized quantity expressed as a ratio between the peak location at a temperature t and at a reference temperature of 20 °C. The ratio is thus equal to 1 for 20 °C. The observed shift (can be seen in figure 7.16) is in the direction of lower energies (spectrum shrinks) for the $CeBr_3$ detector, whereas the semiconductor CdZnTe undergoes a peak shift in the opposite direction. With the CZT#1, the most evident shift is at lower temperatures under zero, where the relative peak shift goes down to -5 % for -40 degrees Celsius. For positive temperatures, the change is almost negligible. For the $CeBr_3$ detector, the peak shift is

larger (please note the experiment conditions described in part 6.7), around +15 % for −40 degrees and down to almost −20 % at +60 degrees Celsius.

7.3.4 Obtained spectra

As already discussed, the spectra under various temperatures change their shape in terms of its scale in both directions (energy and counts). For comparison, spectra measured at different temperatures are shown in figures 7.17 and 7.18. The spectra were obtained having ^{60}Co and ^{137}Cs sources in the detectors closest proximity. To generate as much particles (and therefore good statistic) as possible, all available sources were placed near the detector. Unfortunately, the size of the detector is too small and even though the strongest sources available were used, the experiment yielded only a few counts. This is evident in the case of CZT#1 spectra shown.

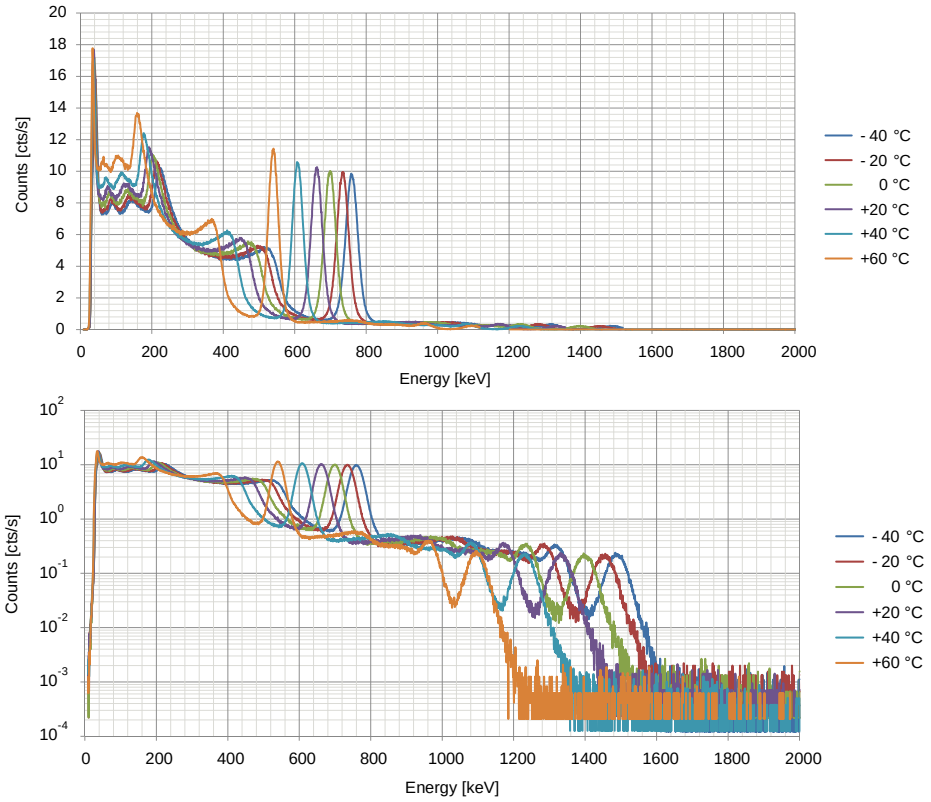

Figure 7.17: Comparison of the $CeBr_3$ spectra influenced by varying temperature. Lower plot provides the same, but in a logarithmic scale.

The energy was calibrated by hand in Excel using three peaks (of ^{137}Cs and ^{60}Co) and their energies: ^{137}Cs at 662 keV, ^{60}Co at 1.17 MeV and 1.33 MeV. This calibration was done for every spectrum relative to the spectrum obtained at 20 degrees Celsius, which was taken as reference. The presented spectra with a logarithmic scale (lower plots in figures 7.17 and 7.18) show weak cobalt peaks located at higher energies and provide a different point of view on the whole spectrum. The recorded counts per seconds shall not be taken as absolute since both $CeBr_3$ and CZT temperature test were done under different conditions in terms of the irradiation flux (position and strength of radioactive sources).

Unfortunately, the second CdZnTe detector CZT#2 yielded very degraded spectra at temperatures under 10 degrees Celsius. The cesium peak splits at these lower temperatures and its left part travels to the left as temperature decreases. For temperatures above this point, however, spectra with good quality were obtained. The comparison of spectra measured with cesium and cobalt at once is shown in figure 7.19. The cesium peak more or less preserved its original peak width measured at room temperature for all the positive temperatures +20 °C, +40 °C and +60 °C.

7.3.5 Comparison with other publications

Similar temperatures tests were done for example in publication [3], where 10 x 10 x 10 and 15 x 15 x 10 mm^3 CdZnTe detectors were tested under different temperatures and bias voltages. The temperature

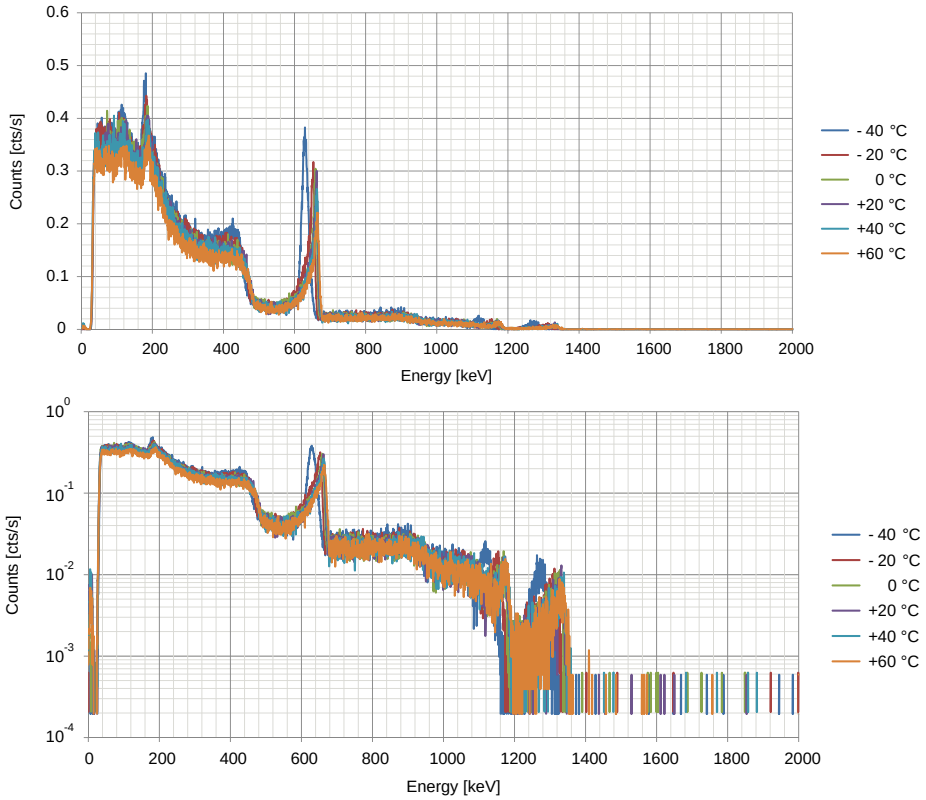

Figure 7.18: Comparison of the CZT#1 spectra influenced by varying temperature. Lower plot provides the same, but in a logarithmic scale.

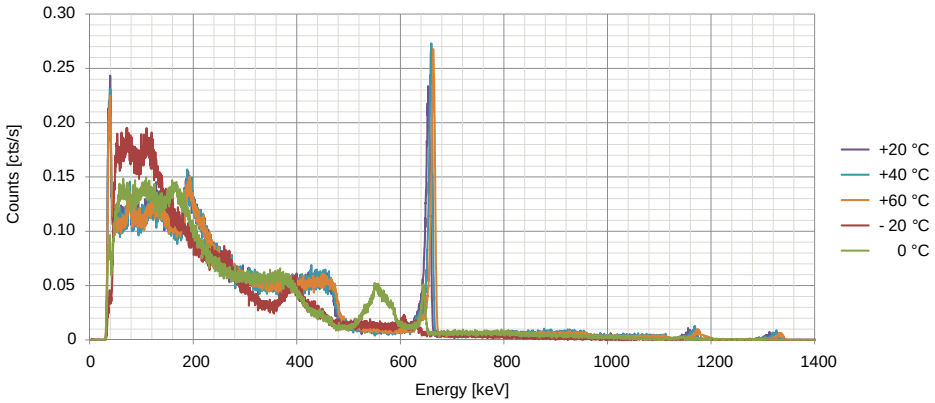

Figure 7.19: Comparison of the CZT#2 spectra influenced by varying temperature. Measured with ^{137}Cs and ^{60}Co.

range of −20 to +20 degrees Celsius was not as wide as in our case, though. The paper clearly shows a trend different from what we observed at temperatures under zero. The FWHM of ^{137}Cs peaks is further reduced at lower temperatures (1 % at −20 °C compared to 1.7 % at +20 °C). However, the authors also mentioned a spectrum degrading phenomenon occurring at temperatures below −30 °C – the resolution got worse depending on the incoming photon flux. Upon further inspections, this phenomenon is believed to be caused by imperfect charge collection resulting in polarization of the detector.

The company *Ritec* itself tested its CdZnTe detectors as well. The results are presented in [38]. This paper shows different behavior of same detector with same volume cut from different ingots. The paper by its measurements from −20 to +20 °C also confirms trends observed in our measurements, which includes charge collection issues at low temperatures and rising noise currents at higher temperatures.

Another temperature study of CdZnTe detectors can be found in a dissertation [18]. The measurements presented show a different behavior regarding peak shift (peak shifts to lower energies with rising temperature). The author, however, shows also an opposite behavior of the electronics. It seems that the small shift to higher energies is in our case caused by temperature dependence of the preamplifier.

Presented dependence of FWHM confirms the rising trend at higher temperatures, but lacks information about dependence under −10 °C.

The same dissertation [18] presents an interesting temperature study of an $LaBr_3$(Ce) detector, which is with its material properties close to our $CeBr_3$ detector. The peak shifts similarly as presented here to lower energies. The presented plot is very similar to our measurements, the peak location is found to be at +10 % at −20 °C (shift relative to +20 °C) and -10 % at +50 °C (compare with figure 7.16).

The $CeBr_3$ resolution temperature dependence shown in figure 7.15 is mainly caused by electronics. The material itself exhibits an opposite behavior as shown by several studies of a similar material $LaBr_3$(Ce). For $LaBr_3$(Ce) from the manufacturer Saint-Gobain the resolution is better for higher temperatures. It is however in order of few percent (+5 % at −40 °C down to −2 % at +60 °C measured in [36] again normalized to +20 °C), which is not measurable in our case, having the complete electronics inside the climatic chamber. Same results are provided in [18] as well, pointing out the temperature dependence of PMTs, which is opposite to that of the $LaBr_3$(Ce).

7.4 Background

Due to the small size of the detectors, the sensitivity to background radiation is very low. This background is usually subtracted from the measurements, so that better accuracy is achieved for nuclide-specific spectra.

In figure 7.20, a comparison of a background radiation in a room (concrete building) is shown. The first presented spectra were measured using a CZT#1 detector for 7 days, in total 236 thousand counts were recorded. The sensitivity to background radiation is thus 23 counts min^{-1} only. The second spectrum was obtained using the $CeBr_3$ detector and was measured for a shorted duration (24 hours). In total 207 thousand counts were recorded. Thanks to the larger volume, the sensitivity was slightly higher: 146 counts min^{-1}. Individual nuclides are hardly recognizable. Although, in the spectrum recorded using CdZnTe, photopeaks of naturally occurring ^{226}Ra can be seen (marked in the plot). These are the most probable emissions from the lead ^{214}Pb and bismuth ^{214}Bi daughters.

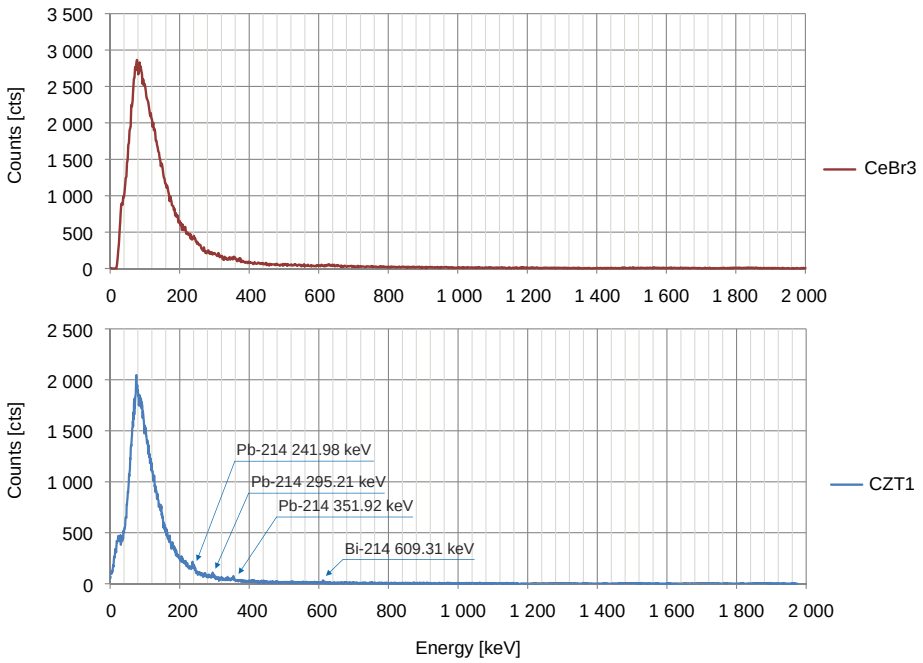

Figure 7.20: Background radiation measured in office (concrete building) using the $CeBr_3$ (24-hour spectrum) and CZT#1 (7-day spectrum) detectors.

7.5 Spectra comparison at low dose rates

Table 7.1 shows a comparison of the most important estimated parameters of the measured spectra for the detector types tested in the radiation chamber. These were defined in section 3.8. Not all of the parameters are easy to obtain due to bad statistics, background noise in the spectrum, large areas of

Parameter	^{137}Cs $CeBr_3$	^{137}Cs CZT#1	^{60}Co $CeBr_3$	^{60}Co CZT#1
FWHM [%]	5.9	1.4	3.9 / 3.7	1.2 / 1.1
Peak-To-Compton [-]	1.8	2.0	~ 1.5	~ 1.0
Peak-To-Total [%]	8*	4*	6.6	3.2
Peak Sensit. [counts $\mathrm{min}^{-1}/\mu\mathrm{Sv}\,\mathrm{h}^{-1}$]	125	6	24	0.5
Total Sensit. [counts $\mathrm{min}^{-1}/\mu\mathrm{Sv}\,\mathrm{h}^{-1}$]	1650	140	750	70

Table 7.1: Comparison of parameters describing spectrum quality for different detectors and sources. (parameters are defined in section 3.8). The Peak-To-Total values marked with * are distorted due to backscattering, fluorescence and bremsstrahlung from surrounding materials [62].

Compton continua and superposition of Compton continua and peaks. These effects were major issue for estimating parameters for spectra obtained for Co^{60}. The Peak-To-Compton ratio with its vague definition is also hard to measure. We did our best, however, to estimate the parameters as accurate as possible.

The table shows important aspects of the detector choice and energies measured. Gamma rays with higher energies do not get fully absorbed in the small-sized crystals, resulting in large Compton continuum. This is also related to peak sensitivity, which is then smaller. While the peak sensitivity expresses a number of counts recorded in the photopeak and thus scales down with the size of Compton continuum, the total sensitivity expresses the amount of particles detected in general, no matter what amount of energy they deposited. The total sensitivity thus does not scale down with size and/or energy as much as the peak sensitivity. This can be noticed in the table by looking at ratios of peak sensitivities. The ratio $CeBr_3$/CZT cesium is approx. 21 compared to $CeBr_3$/CZT cobalt, which is 48. $CeBr_3$ cesium/cobalt peak sensitivity ratio is approx. 5, whereas the same ratio for CZT is 12. Scattering coming from higher energies in combination with small volume causes scattered photons escape the medium volume, whereas larger volume has higher probability of making the scattered photons fully deposit their energy in favor of the photopeak. So both the detector size and particle energy have influence on counts in the peak. The same can be done for total sensitivities, where ratios only slightly differ: $CeBr_3$/CZT cesium ratio is approx. 12 and $CeBr_3$/CZT Cobalt approx. 11; for $CeBr_3$ cesium/cobalt total sensitivity it is slightly above 2 and exactly 2 for the last one.

It is quite non-trivial to hold up considering all the aspects, because it is not only the size and energy influencing the results, but also the non-linearity of the H*(10) dose rate equivalent itself as presented in figure 2.3. The same amount of dose equivalent can be produced by less amount of counts (events). Therefore publications and datasheets always try to use ^{137}Cs as reference.

7.5.1 Comparison with simulations

The Peak-To-Total values shown in table 7.1 can be compared with simulation results listed in table 5.1. The Peak-To-Total values for cobalt were measured with as free surroundings as possible (a naked ^{60}Co source was used). The measurements of cesium sources included counts coming from surrounding materials (backscattering, fluorescence and bremsstrahlung [62]) and are thus, as such, not very precise. Comparing these to simulations, the Peak-To-Total ratio for ^{137}Cs was expected to be approximately two times larger. The Peak-To-Total of more accurately measured ^{60}Co was found to be close to the values obtained using simulation.

7.5.2 Europium ^{152}Eu

A source containing Europium nuclides ^{152}Eu was used to demonstrate difference between the detector materials, mainly their resolution. Europium is a great alternative to single-photopeak spectrum obtained using the standard ^{137}Cs or two-photopeak spectrum of ^{60}Co. Europium has a relatively long decay chain, emitting gamma photons many time throughout its decay. Therefore, many lines in a spectrum are obtained. The individual gamma emissions with a probability larger than 1 % are listed in table 7.2. Practically all of the emissions can be recognized in a spectrum recorded by CZT. The $CeBr_3$, however, does not provide a resolution allowing to detect either lines close to each other or with low emission probabilities.

Recording of such spectrum, again, required longer measurement time due to detectors size. The data presented in figure 7.21, especially at higher energies, contain a lower number of counts. The data should also not be taken absolute, there are noise counts and counts coming from natural radiation background present.

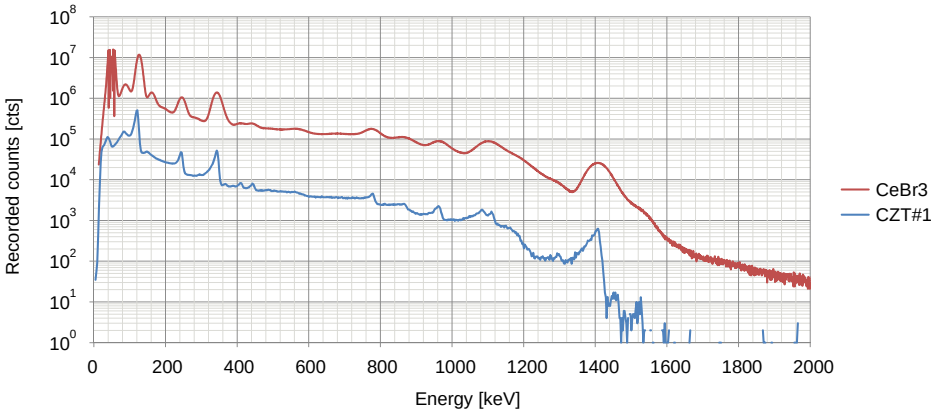

Figure 7.21: Comparison of the $CeBr_3$ and CZT#1 spectrum of Europium (^{152}Eu).

Energy [keV]	Emission probability [%]
122	28.6
245	7.6
344	26.5
411	2.2
444	2.8
779	12.9
867	4.3
964	14.6
1 086	10.2
1 090	1.7
1 112	13.7
1 213	1.4
1 299	1.6
1 408	21.0

Table 7.2: Gamma-ray emission of ^{152}Eu decay chain. Only energies with emission probability over 1 % are listed. Taken from [41].

7.5.3 Cesium ^{137}Cs

Cesium, with its single gamma emission line, is ideal for understanding underlying physics in the detectors. A spectrum measured at low dose rate (LD) is in figure 7.22 is compared to one measured at high dose rates (HD). The exact dose rate equivalents are listed in table 7.3.

Clearly, a big difference in a shape of the spectra is seen for CZT and $CeBr_3$. The Gaussian peak of the scintillator is typical, whereas for CZT peak extending to the left is present. This low-tailing is strongly dependent on the CdZnTe structure (trapping sites caused by Tellurium doping) and varies from ingot to ingot. The CZT#2 detector for example had a much smaller low-tailing effect (see for example figure 7.12) than the CZT#1. Otherwise, the resolution of CdZnTe crystal is superb, on the right side it declined very quickly, approximately with a rate of a Gaussian shape with 1% FWHM.

The LD spectra of both detectors look quite natural and correspond to physical models and simulations provided in chapter 5. For HD, saturation comes into play in terms of too many pulses occurring at the signal. The saturation is either by pulses piling up onto each other and escaping the measurable range of the MCA input or piling up in a way that they are thrown away by a pile-up inspection algorithm. The spectrum is not clean anymore and background noise coming from this kind of signal processing (inspection of pulses in time) is added to the spectrum. The photopeak sits then on top of this background and does no longer strictly end at its tail. Higher energies are occupied by pile-ups that went through and could not be software-recognized.

Even an additional phenomenon occurs at higher rates, the piled-up pulses are under the resolution of the μDXP, cannot be filtered out and are let to be added to the spectrum. These pulses of twice the original peak's amplitude produce a secondary peak in the spectrum (even tertiary peaks in the spectrum can be observed as a result of three pulses recorded at the same instant). This effect was observed in spectra of all tested detectors.

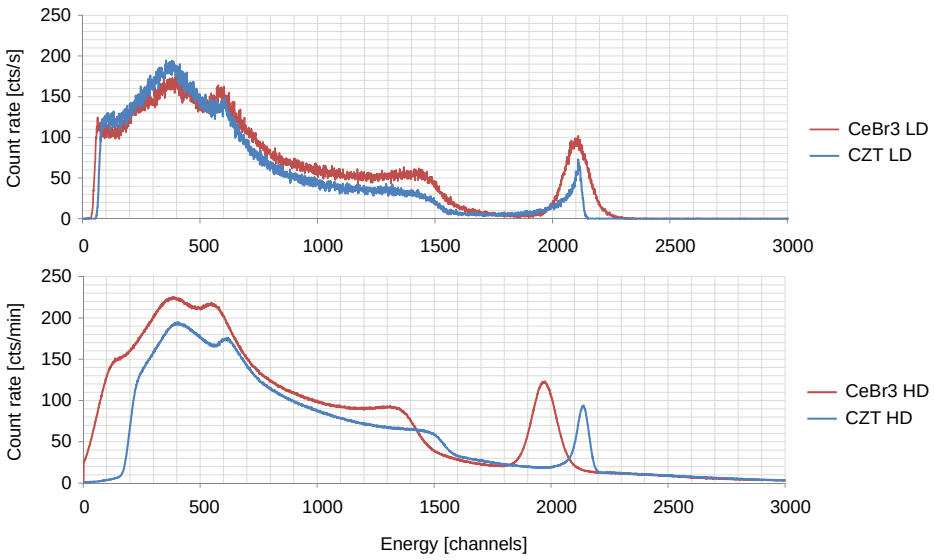

Figure 7.22: Comparison of the $CeBr_3$ and CZT#1 spectrum of cesium (Cs^{137}) at very high and very low dose rates (see table 7.3 for values). Please note that the spectra are scaled thanks for different time bases (1-minute and 1-second spectrum).

Detector	Low dose rate (LD)	High dose rate (HD)
	[µSv h^{-1}]	[µSv h^{-1}]
$CeBr_3$	94	19 183
CZT#1	849	235 894

Table 7.3: Dose rates for figure 7.22.

7.5.4 Cobalt ^{60}Co

For ^{60}Co, spectrum for HD and LD is shown as well (see figure 7.23) for data listed in table 7.4. Unfortunately, higher rates could not be generated and the higher achieved rate of 100 mSv h^{-1} was already too close to the source (Buchler) and the error in calibration might not be negligible. This amount of dose was, however, already too large for the $CeBr_3$ detector and no spectrum was collected as the output count rate dropped to very low values. Therefore 10 mSv h^{-1} was used for comparison, where pile-up noise is already present. For CZT#1, pile-up consequence is already evident in the spectrum at the dose rate of 100 mSv h^{-1}.

Calculating total peak area (sum of two peak areas) for ^{60}Co was a non-trivial task and several approximations had to be made. Values presented in table 7.1 might thus not be 100% correct, although they provide a sufficient measure of how the Co^{60} gamma radiation interacts with the crystal compared to Cs^{137}.

Although the energy of ^{60}Co is around 1.3 MeV only, its Compton continuum is already very large compared to the photopeaks area. This poses a limitation for the detector size discussed in 6.2. The CZT detector might already be too small for our application, where energies ranging from 30 keV to 3 MeV are assumed. Moreover, the tiny crystal lets most of the high-energy radiation pass through, resulting in a very bad values of both total and peak sensitivity. Listed in table 7.1, the peak sensitivity of ^{60}Co gammas incident on the CZT#1 is not even a count per second per µSv h^{-1}!

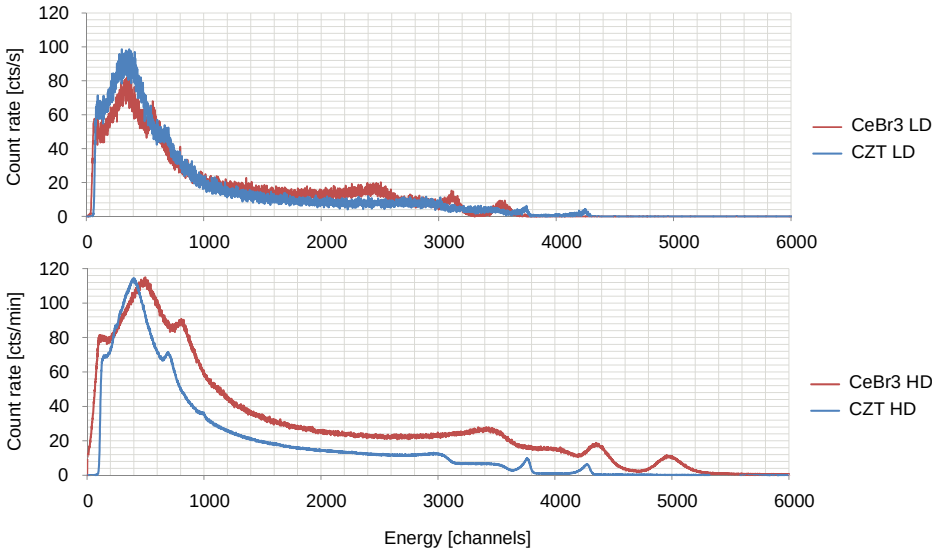

Figure 7.23: Comparison of the $CeBr_3$ and CZT#1 spectrum of cobalt (Co^{60}) at high and low dose rates (see table 7.4 for values). Please note that the spectra are scaled thanks for different time bases (1-minute and 1-second spectrum). For legibility purposes, the spectrum of HD $CeBr_3$ was multiplied by 4.

Detector	Low dose rate (LD)	High dose rate (HD)
	[μSv/h]	[μSv/h]
$CeBr_3$	100	10 000
CZT#1	1 000	100 000

Table 7.4: Dose rates for figure 7.23.

Chapter 8
Conclusion

The study of a HD spectrometer presented in this thesis shows that by a careful selection of the detection material as well as subsequent electronics, high dose rate spectrometric measurements can be achieved. Even though there are several limitations cause by material speed or insufficient electronics speed, measurable spectra of good values were acquired for dose rates equivalents (H*(10) norm) of up to 300 $\mathrm{mSv\,h^{-1}}$ in case of the tiny 60 $\mathrm{mm^3}$ CdZnTe detector and 40 $\mathrm{mSv\,h^{-1}}$ for the $CeBr_3$ detector (785 $\mathrm{mm^3}$). The achieved rates were further limited by the speed of the MCA (a 16-megahertz XIA's μDXP) and by the preamplifier design with slow decay time in the case of CdZnTe detectors (two were tested). As directly seen, the volume of the detector is the most influencing factor of the achievable dose rates.

The quality of measured spectra was compared in terms of the standard parameters used in gamma-ray spectroscopy and is presented in table 7.1. The Compton scattering phenomenon is dominant for larger energies (table 5.1) as predicted by the simulations.. It must be noted, however, that according to the list of important nuclides defined by an ANSI standard (of which all daughter nuclides are plotted in figure 3.1), the need of spectrometric information is mostly needed in for energies up to 1.5 MeV. Having taken that into account, then even though the Peak-To-Total and Peak-To-Compton ratios are degraded by the tiny size of the selected detectors, the nuclide identification is still possible for the vast majority of important nuclides environmental monitoring and safety monitoring is interested in. A further analysis of software identification shall be done in order to confirm the possibility of automating the recognition of nuclides. For that purpose, fitting of spectrum peaks might be interesting and was therefore discussed in section 7.1.1. The CdZnTe peak exhibits large low-energy exponential tailing effects that are caused by hole tailing. The $CeBr_3$ peak shape is a standard Gaussian function caused by PMT and subsequent electronics.

It was shown by the experiments made with both detectors, that high dose rate results in high count rates processed by the electronics which further results in degraded spectrum (flattening and raised background) in terms of pulse pile-up and other phenomena. The dose rate tests also show very good stability of peak location for both the materials, slightly favoring the CdZnTe detector (figure 7.8). As expected, the resolution gets worse at higher dose rates as well as the peak area. The achieved resolution was very good for CdZnTe detector (under 3 % for even extreme doses), far superior to that of $CeBr_3$.

The temperature tests showed some very good stability of both detectors and surprisingly good for the semiconductor CdZnTe detector with a relatively wide band gap. The resolution (FWHM) was found to be temperature stable and acceptable for both the $CeBr_3$ detector (5-6 %) and close to stable for the CdZnTe detector (2-3 %) as presented in figure 7.15. Almost no peak location shift was observed for the CdZnTe detector, whereas the $CeBr_3$ detector shifted by 30 % in the whole temperature range from $-40\,^{\circ}\mathrm{C}$ to $60\,^{\circ}\mathrm{C}$.

Both the HD and temperature tests showed substandard behavior of the second CdZnTe detector. Even though the detector performed better in terms of resolution and hole tailing at lower dose rates, the charge-trapping (believed to be the cause) degrading the spectrum made impossible to achieve dose rates above 100 $\mathrm{mSv\,h^{-1}}$. This degradation seemed to not only be influenced by the dose, but also by the time of exposition to it. The temperature tests showed similar peak degradation for temperatures under $-20\,^{\circ}\mathrm{C}$ for the CZT#1 detector and $0\,^{\circ}\mathrm{C}$ for the CZT#2 detector.

Thanks to the achieved high dose rates and its acceptable temperature dependence and other properties discussed in this work, the CdZnTe seems to be a powerful candidate for the environmental radiation monitoring at high doses. A care must be taken, not to further reduce the volume due to its low sensitivity to lower doses (which might pose a no-overlap problem when switching between low and high dose spectrometers) and its peak reduction in comparison to Compton continuum at higher energies (already visible in the presented ^{60}Co spectra). Moreover it must be checked, that a particular detector does not undergo a polarization, which is dependent on the internal structure (density of impurities). So far,

this is the largest issue with CdZnTe detectors as they differ from ingot to ingot and the problem with hole trapping is not very well under control yet from the manufacturing point of view. The discussion of long-term stability, which could not be tested due to the short time period for the thesis, is provided for example by the International Atomic Energy Agency (IAEA) for hemispheric detectors tested over a year [6] and other CdZnTe detectors in a 5-month test [81]. A long-term stability reported for CdZnTe detectors, their resistivity to shocks and vibrations (tested according to the ANSI standard testing protocol of vibration and mechanical shock testing for hand-held radiation detection instruments in [49] – temperature cycling from $-40\,°C$ to $60\,°C$ is tested in the same article) ANSI N42.34-2006, make them a good choice for deployment in environmental radiation detection.

Further improvement and development of the presented HD spectrometer is possible by raising the limits of the electronics. Future work shall concentrate on a use of faster MCAs and also optimize the preamplifier for both detector types (reduce decay time in case of the CdZnTe detectors and reduce FWHM in case of $CeBr_3$). Eventually, prototypes of such HD spectrometers shall be tested in harsh environment for a longer period of time to prove their suitability for environmental radiation monitoring.

Chapter 9
Appendices

9.1 Appendix A – Master thesis assignment

Attached is the official assignment from the Czech Technical University in Prague, Department of Control Engineering at the Faculty of Electrical Engineering from December 4, 2014. The thesis was partially prepared during an individual project preceding the master thesis. Although the assignment originates from the Department of Control Engineering, the thesis was prepared under a supervision of the Department of Measurement.

9.2 Appendix B – Measurements, simulations and other data

Data including all measurements, simulations from Geant4 with the use of MATLAB and ROOT, source codes, used circuits, research and other data closely related to this work are attached electronically on a CD. The thesis is also electronically available on the same CD in a root folder under a name *master_thesis_marek_hudec.pdf*.

Thesis
Bibliography

[1] International Atomic Energy Agency. The power reactor information system IAEA PRIS. `http://www.iaea.org/pris/`. online database, Accessed: May 2015.

[2] D. Alexiev, L. Mo, D. A. Prokopovich, M. L. Smith, and M. Matuchova. Comparison of $LaBr_3$:Ce and $LaCl_3$:Ce with NaI(Tl) and cadmium zinc telluride (CZT) detectors. *Nuclear Science, IEEE Transactions on*, 55(3):1174–1177, June 2008.

[3] M. Amman, J. S. Lee, and P. N. Luke. Temperature study of CdZnTe coplanar-grid detectors. *Nuclear Science, IEEE Transactions on*, 53(5):3035–3040, 2006.

[4] J. Annex. Exposures and effects of the Chernobyl accident. *Sources and Effects of Ionizing Radiation: The United Nations Scientific Committee on the Effects of Atomic Radiation UNSCEAR*, pages 451–566, 2000.

[5] G. Ariño-Estrada, M. Chmeissani, G. de Lorenzo, M. Kolstein, C. Puigdengoles, J. García, and E. Cabruja. Measurement of mobility and lifetime of electrons and holes in a Schottky CdTe diode. *Journal of Instrumentation*, 9(12):C12032, 2014.

[6] R. Arlt, V. Gryshchuk, and P. Sumah. Gamma spectrometric characterization of various CdTe and CdZnTe detectors. *Nuclear Instruments and Methods in Physics Research Section A: Accelerators, Spectrometers, Detectors and Associated Equipment*, 428(1):127–137, 1999.

[7] S. Baccaro, K. Blažek, F. De Notaristefani, P. Malý, J. A. Mareš, R. Pani, R. Pellegrini, and A. Soluri. Scintillation properties of YAP:Ce. *Nuclear Instruments and Methods in Physics Research Section A: Accelerators, Spectrometers, Detectors and Associated Equipment*, 361(1):209–215, 1995.

[8] M. Balcerzyk, M. Moszyński, Z. Galazka, M. Kapusta, A. Syntfeld, and J. L. Lefaucheur. Perspectives for high resolution and high light output LuAP:Ce crystals. In *Nuclear Science Symposium Conference Record, 2004 IEEE*, volume 2, pages 986–992 Vol. 2, Oct 2004.

[9] M. Balcerzyk, M. Moszyński, M. Kapusta, D. Wolski, J. Pawelke, and C. L. Melcher. YSO, LSO, GSO and LGSO. a study of energy resolution and nonproportionality. *Nuclear Science, IEEE Transactions on*, 47(4):1319–1323, Aug 2000.

[10] D. S. Bale and C. Szeles. Nature of polarization in wide-bandgap semiconductor detectors under high-flux irradiation: Application to semi-insulating $Cd_{1-x}Zn_xTe$. *Physical Review B*, 77(3):035205, 2008.

[11] A. S. Beddar. Plastic scintillation dosimetry and its application to radiotherapy. *Radiation measurements*, 41:S124–S133, 2006.

[12] S. C. Bedi, W. Tröger, and T. Butz. Improving the energy resolution of BaF_2 scintillators by cooling. *Hyperfine Interactions*, 136-137(3-8):161–164, 2001.

[13] M. Bolić and V. Drndarević. Digital gamma-ray spectroscopy based on FPGA technology. *Nuclear Instruments and Methods in Physics Research Section A: Accelerators, Spectrometers, Detectors and Associated Equipment*, 482(3):761–766, 2002.

[14] A. Brambilla, P. Ouvrier-Buffet, J. Rinkel, G. Gonon, C. Boudou, and L. Verger. CdTe linear pixel X-ray detector with enhanced spectrometric performance for high flux X-ray imaging. *Nuclear Science, IEEE Transactions on*, 59(4):1552–1558, 2012.

[15] U. Büttner. *Fukushima Daiichi: 11. März 2011; Unfallablauf, radiologische Folgen.* Gesellschaft für Anlagen-und Reaktorsicherheit (GRS), 2014.

[16] W. Chewpraditkul, L. Swiderski, M. Moszyński, T. Szczesniak, A. Syntfeld-Kazuch, C. Wanarak, and P. Limsuwan. Scintillation properties of LuAG:Ce, YAG:Ce and LYSO:Ce crystals for gamma-ray detection. *Nuclear Science, IEEE Transactions on*, 56(6):3800–3805, Dec 2009.

[17] D.J. Corvan, G. Sarri, and M. Zepf. Design of a compact spectrometer for high-flux MeV gamma-ray beams. *Review of Scientific Instruments*, 85(6):065119–065119–7, Jun 2014.

[18] M. Dambacher. Entwicklung eines digitalen Detektorsystems zur spektroskopischen Überwachung der Umweltradioaktivität auf Basis von (Cd,Zn)Te Detektoren. *Dissertation University Freiburg*, 2012.

[19] S. Del Sordo, L. Abbene, E. Caroli, A. M. Mancini, A. Zappettini, and P. Ubertini. Progress in the development of CdTe and CdZnTe semiconductor radiation detectors for astrophysical and medical applications. *Sensors*, 9(5):3491–3526, 2009.

[20] V. Drndarević, P. Ryge, and T. Gozani. Digital signal processing for high rate gamma-ray spectroscopy. *Nuclear Instruments and Methods in Physics Research Section A: Accelerators, Spectrometers, Detectors and Associated Equipment*, 277(2):532–536, 1989.

[21] W. Drozdowski, P. Dorenbos, A. J. J. Bos, G. Bizarri, A. Owens, and F. G. A. Quarati. $CeBr_3$ scintillator development for possible use in space missions. *Nuclear Science, IEEE Transactions on*, 55(3):1391–1396, June 2008.

[22] S. A. Dyer. *Wiley survey of instrumentation and measurement.* John Wiley & Sons, 2004.

[23] D. E. Eastlake, J. I Schiller, and S. Crocker. Randomness requirements for security. In *BCP 106, RFC 4086*. Citeseer, 2005.

[24] C. Fiorini, A. Gola, M. Zanchi, A. Longoni, P. Lechner, H. Soltau, and L. Struder. Gamma-ray spectroscopy with $LaBr_3$:Ce scintillator readout by a silicon drift detector. In *Nuclear Science Symposium Conference Record, 2005 IEEE*, volume 1, pages 230–234. IEEE, 2005.

[25] M. Gierlik, J. Iwanowska, T. Kozlowski, M. Moszyński, L. Swiderski, and T. Szczesniak. The comparison of large scintillators for high energy gamma-rays detection. In *Nuclear Science Symposium Conference Record (NSS/MIC), 2010 IEEE*, pages 501–505, Oct 2010.

[26] F. S. Goulding. Pulse-shaping in low-noise nuclear amplifiers: A physical approach to noise analysis. *Nuclear Instruments and Methods*, 100(3):493–504, 1972.

[27] R. Grill, E. Belas, J. Franc, M. Bugár, S. Uxa, P. Moravec, and P. Hoschl. Polarization study of defect structure of CdTe radiation detectors. *Nuclear Science, IEEE Transactions on*, 58(6):3172–3181, 2011.

[28] R. Gunnink and R. Arlt. Methods for evaluating and analyzing CdTe and CdZnTe spectra. *Nuclear Instruments and Methods in Physics Research Section A: Accelerators, Spectrometers, Detectors and Associated Equipment*, 458(1):196–205, 2001.

[29] KK Hamamatsu Photonics. Photomultiplier tubes: Basics and applications. *Edition 3a*, 2006.

[30] KK Hamamatsu Photonics. Si photodiodes. *Opto-semiconductor handbook: Chapter 2*, 2014.

[31] J. Harris. microDXP digital X-ray processor technical reference manual. `http://www.xia.com/Manuals/microDXP_Technical_Reference_Manual.pdf`, August 6 2009. datasheet, Accessed: May 2015.

[32] J. H. Hubbell and S. M. Seltzer. Tables of X-ray mass attenuation coefficients and mass energy-absorption coefficients. *National Institute of Standards and Technology*, 1996.

[33] ICRP. Conversion coefficients for use in radiological protection against external radiation., 1996.

[34] ICRP. Annex B. basis of dosimetric quantities used in radiological protection., 2007.

[35] IEEE. IEEE standard test procedures for germanium gamma-ray detectors. *ANSI/IEEE Std 325-1986*, 1987.

[36] A. Iltis, M. R. Mayhugh, P. Menge, C. M. Rozsa, O. Selles, and V. Solovyev. Lanthanum halide scintillators: Properties and applications. *Nuclear Instruments and Methods in Physics Research Section A: Accelerators, Spectrometers, Detectors and Associated Equipment*, 563(2):359–363, 2006.

[37] V. Ivanov, L. Aleksejeva, P. Dorogov, and Loutchanski A. Miniature CdZnTe detectors for application in high intensity radiation fields, 2008.

[38] V. Ivanov, P. Dorogov, A. Loutchansky, L. Aleksejeva, and E. Mozchaev. Further development of hemispherical CdZnTe detectors for safeguards applications. *Energy*, 600(800):1000, 1999.

[39] F. James. A review of pseudorandom number generators. *Computer Physics Communications*, 60(3):329–344, 1990.

[40] M. Jönsson. Collimation technique for HPGe-detector gamma spectrometry in intense radiation fields, 2010.

[41] Korea Atomic Energy Research Institute (KAERI). Table of nuclides ATOM. `http://atom.kaeri.re.kr`, 2012. online database, Accessed: May 2015.

[42] W. Klamra, P. Sibczynski, M. Moszyński, and V. Kozlov. Study of undoped CeF_3 scintillators at room and liquid nitrogen temperature. In *Nuclear Science Symposium and Medical Imaging Conference (NSS/MIC), 2012 IEEE*, pages 315–317, Oct 2012.

[43] G. F. Knoll. *Radiation detection and measurement*. John Wiley & Sons, 2010.

[44] G. F. Knoll, T. F. Knoll, and T. M. Henderson. Light collection in scintillation detector composites for neutron detection. *Nuclear Science, IEEE Transactions on*, 35(1):872–875, 1988.

[45] L. A. Kosyachenko, E. Diequez, T. Aoki, C. P. Lambropoulos, V. A. Gnatyuk, M. Fiederle, S. V. Melnychuk, O. L. Maslyanchuk, O. F. Sklyarchuk, O. V. Sklyarchuk, et al. Special features of conductivity of semi-intrinsic CdTe and CdZnTe single crystals used in X- and γ-ray detectors. In *SPIE Optical Engineering+ Applications*, pages 78051I–78051I. International Society for Optics and Photonics, 2010.

[46] G. Lasche. Cambio overview (viewgraph presentation). Technical report, Sandia National Laboratories, 2012.

[47] P. Lechner, S. Eckbauer, R. Hartmann, S. Krisch, D. Hauff, R. Richter, H. Soltau, L. Strüder, C. Fiorini, E. Gatti, et al. Silicon drift detectors for high resolution room temperature X-ray spectroscopy. *Nuclear Instruments and Methods in Physics Research Section A: Accelerators, Spectrometers, Detectors and Associated Equipment*, 377(2):346–351, 1996.

[48] O. Limousin. New trends in CdTe and CdZnTe detectors for X- and gamma-ray applications. *Nuclear Instruments and Methods in Physics Research Section A: Accelerators, Spectrometers, Detectors and Associated Equipment*, 504(1):24–37, 2003.

[49] P. H. Lu, P. Gomolchuk, H. Chen, D. Beitz, and A. W. Grosser. Ruggedization of CdZnTe detectors and detector assemblies for radiation detection applications. *Nuclear Instruments and Methods in Physics Research Section A: Accelerators, Spectrometers, Detectors and Associated Equipment*, 2015.

[50] Hellma Materials. Radiation detection materials, 2014.

[51] D. J. Mitchell, L. Harding, G. G. Thoreson, and S. M. Horne. Gadras detector response function. *Sandia National Laboratories, SAND*, 19465:2014, 2014.

[52] M. Moszyński, M. Balcerzyk, W. Czarnacki, M. Kapusta, W. Klamra, A. Syntfeld, and M. Szawlowski. Intrinsic energy resolution and light yield nonproportionality of BGO. *Nuclear Science, IEEE Transactions on*, 51(3):1074–1079, June 2004.

[53] M. Moszyński, M. Balcerzyk, M. Kapusta, A. Syntfeld, D. Wolski, G. Pausch, J. Stein, and P. Schotanus. $CdWO_4$ crystal in gamma-ray spectrometry. *Nuclear Science, IEEE Transactions on*, 52(6):3124–3128, Dec 2005.

[54] M. Moszyński, C. Gresset, J. Vacher, and R. Odru. Properties of CsF, a fast inorganic scintillator in energy and time spectroscopy. *Nuclear Instruments and Methods*, 179(2):271–276, 1981.

[55] M. Moszyński, M. Kapusta, D. Wolski, W. Klamra, and B. Cederwall. Properties of the YAP:Ce scintillator. *Nuclear Instruments and Methods in Physics Research Section A: Accelerators, Spectrometers, Detectors and Associated Equipment*, 404(1):157–165, 1998.

[56] M. Moszyński, M. Kapusta, D. Wolski, M. Szawlowski, and W. Klamra. Energy resolution of scintillation detectors with large area avalanche photodiodes and photomultipliers light readout. In *Nuclear Science Symposium, 1997. IEEE*, pages 206–211 vol.1, Nov 1997.

[57] M. Moszyński, A. Nassalski, A. Syntfeld-Kazuch, T. Szczesniak, W. Czarnacki, D. Wolski, G. Pausch, and J. Stein. Temperature dependences of $LaBr_3$(Ce), $LaCl_3$(Ce) and NaI(Tl) scintillators. *Nuclear Instruments and Methods in Physics Research Section A: Accelerators, Spectrometers, Detectors and Associated Equipment*, 568(2):739–751, 2006.

[58] M. Moszyński, L. Swiderski, T. Szczesniak, A. Nassalski, A. Syntfeld-Kazuch, W. Czarnacki, G. Pausch, J. Stein, P. Lavoute, F. Lherbert, and F. Kniest. Study of $LaBr_3$ crystals coupled to photomultipliers and avalanche photodiodes. *Nuclear Science, IEEE Transactions on*, 55(3):1774–1780, June 2008.

[59] D. Nakazawa, P. Schotanus, and F. Bronson. Characterization and evaluation of temperature-stabilized large volume $CeBr_3$ detectors. In *Nuclear Science Symposium and Medical Imaging Conference (NSS/MIC), 2013 IEEE*, pages 1–3. IEEE, 2013.

[60] M. N. Namboodiri, A. D. Lavietes, and J. H. McQuaid. Gamma-ray peak shapes from cadmium zinc telluride detectors. Technical report, Lawrence Livermore National Lab., CA (United States), 1996.

[61] A. A. Naqvi, F. Z. Khiari, A. Coban, A. Aksoy, and A. M. Al-Jalal. Pulse height resolution of organic scintillators for monoenergetic gamma rays. In *Nuclear Science Symposium and Medical Imaging Conference, 1992., Conference Record of the 1992 IEEE*, pages 4–6 vol.1, Oct 1992.

[62] J. E. Parks. The Compton effect – Compton scattering and gamma ray spectroscopy. *Department of Physics, University of Tennessee, Knoxville, TN*, 2009.

[63] A. Phunpueok, W. Chewpraditkul, P. Limsuwan, and C. Wanarak. Luminescence and scintillation properties of Ce-doped YAP and LuYAP crystals. *Advanced Materials Research*, 199:1789–1795, 2011.

[64] A. Phunpueok, W. Chewpraditkul, P. Limsuwan, and C. Wanarak. Scintillation response of $YAlO_3$:Ce and $Lu_{0.7}Y_{0.3}AlO_3$:Ce single crystal scintillators. *Nuclear Instruments and Methods in Physics Research Section B: Beam Interactions with Materials and Atoms*, 286:76–79, 2012.

[65] F. G. A. Quarati, P. Dorenbos, J. van der Biezen, A. Owens, M. Selle, L. Parthier, and P. Schotanus. Scintillation and detection characteristics of high-sensitivity $CeBr_3$ gamma-ray spectrometers. *Nuclear Instruments and Methods in Physics Research Section A: Accelerators, Spectrometers, Detectors and Associated Equipment*, 729:596–604, 2013.

[66] Amptek Inc. Redus, R. Charge trapping in XR-100T-CdTe cadmium telluride detectors application note. `http://www.amptek.com/charge-trapping-in-xr-100t-cdte-cadmium-telluride-detectors-application-note/`, 2007. online, Accessed: May 2015.

[67] Amptek Inc. Redus, R. Digital pulse processors, theory of operation. *Amptec application note AN-DPP-001*, 2009. online, Accessed: May 2015.

[68] R. H. Redus, J. A. Pantazis, T. J. Pantazis, A. C. Huber, and B. J. Cross. Characterization of CdTe detectors for quantitative X-ray spectroscopy. *Nuclear Science, IEEE Transactions on*, 56(4):2524–2532, 2009.

[69] S. Reinhardt. SARA – spectroscopic gamma detector IGS7/8/9xx. `http://envinet.com/deutsch/component/phocadownload/category/26-sara-air?download=71:datasheet-sara-detector`, April 10 2015. datasheet, Accessed May 2015.

[70] L. Rusell. Introduction to amplifiers. 2012.

[71] P. Schotanus, P. Dorenbos, C. W. E. Van Eijk, and H. J. Lamfers. Suppression of the slow scintillation light output of BaF_2 crystals by La^{3+} doping. *Nuclear Instruments and Methods in Physics Research Section A: Accelerators, Spectrometers, Detectors and Associated Equipment*, 281(1):162–166, 1989.

[72] P. J. Sellin and J. Vaitkus. New materials for radiation hard semiconductor dectectors. *Nuclear Instruments and Methods in Physics Research Section A: Accelerators, Spectrometers, Detectors and Associated Equipment*, 557(2):479–489, 2006.

[73] V. Semiconductor. General properties of Si, Ge, SiGe, SiO_2 and Si_3N_4. *accessed Last Accessed: March*, 10:2012, 2012.

[74] K. S. Shah. $CeBr_3$ scintillator, July 29 2008. US Patent 7,405,404.

[75] K. S. Shah, J. Glodo, M. Klugerman, W. M. Higgins, T. Gupta, and P. Wong. High energy resolution scintillation spectrometers. *Nuclear Science, IEEE Transactions on*, 51(5):2395–2399, Oct 2004.

[76] K. S. Shah, J. Glodo, M. Klugerman, W. W. Moses, S. E. Derenzo, and M. J. Weber. $LaBr_3$:Ce scintillators for gamma-ray spectroscopy. *Nuclear Science, IEEE Transactions on*, 50(6):2410–2413, 2003.

[77] S. A. Soldner, D. S. Bale, and C. Szeles. Dynamic lateral polarization in CdZnTe under high flux X-ray irradiation. *Nuclear Science, IEEE Transactions on*, 54(5):1723–1727, 2007.

[78] ANSI Standard. N42. 34. *Performance Criteria for Hand-held Instruments for the Detection and Identification of Radionuclides*, 2003.

[79] L. Strüder, P. Lechner, and P. Leutenegger. Silicon drift detector–the key to new experiments. *Naturwissenschaften*, 85(11):539–543, 1998.

[80] L. Swiderski, M. Moszyński, A. Nassalski, A. Syntfeld-Kazuch, T. Szczesniak, K. Kamada, K. Tsutsumi, Y. Usuki, T. Yanagida, A. Yoshikawa, and W. Chewpraditkul. Scintillation properties of praseodymium doped LuAG scintillator compared to cerium doped LuAG, LSO and LaBr. In *Nuclear Science Symposium Conference Record, 2008. NSS '08. IEEE*, pages 2840–2846, Oct 2008.

[81] M. Swoboda. Evaluierung von CdZnTe Detektoren in Hinblick auf deren Einsatz in tragbaren Isotopenidentifikationsgeräten, 2003.

[82] A. Syntfeld, R. Arlt, V. Gostilo, A. Loupilov, M. Moszyński, A. Nassalski, M. Swoboda, and D. Wolski. Comparison of a $LaBr_3$(Ce) scintillation detector with a large volume CdZnTe detector. *Nuclear Science, IEEE Transactions on*, 53(6):3938–3943, Dec 2006.

[83] A. Syntfeld-Kazuch, L. Swiderski, W. Czarnacki, M. Gierlik, W. Klamra, M. Moszyński, and P. Schotanus. Non-proportionality and energy resolution of CsI(Tl). *Nuclear Science, IEEE Transactions on*, 54(5):1836–1841, Oct 2007.

[84] C. Szeles, S. A. Soldner, S. Vydrin, J. Graves, and D. S. Bale. CdZnTe semiconductor detectors for spectroscopic X-ray imaging. *Nuclear Science, IEEE Transactions on*, 55(1):572–582, 2008.

[85] Csaba Szeles. CdZnTe and CdTe materials for X-ray and gamma ray radiation detector applications. *Physica status solidi (b)*, 241(3):783–790, 2004.

[86] M. C. Tamargo. *II-VI semiconductor materials and their applications*, volume 12. CRC Press, 2002.

[87] H. H. Tan. A statistical model of the photomultiplier gain process with applications to optical pulse detection. *The Telecommunications and Data Acquisition Progress Report 42-68, January and February 1982*, pages 55–67, 1982.

[88] L. Verger, M. Boitel, M. C. Gentet, R. Hamelin, C. Mestais, F. Mongellaz, J. Rustique, and G. Sanchez. Characterization of CdTe and CdZnTe detectors for gamma-ray imaging applications. *Nuclear Instruments and Methods in Physics Research Section A: Accelerators, Spectrometers, Detectors and Associated Equipment*, 458(1):297–309, 2001.

[89] C. Wanarak and W. Chewpraditkul. Comparison of $Lu_{1.8}Y_{0.2}SiO_5$:Ce and $LaCl_3$:Ce scintillators in gamma-ray spectrometry. *KMUTT Research and Development Journal*, 33(4):253–262, 2011.

[90] M. J. Weber. Inorganic scintillators: today and tomorrow. *Journal of Luminescence*, 100(1):35–45, 2002.

[91] A. Wilms. Scintillator studies. Technical report, GSI Helmholtzzentrum fur Schwerionenforschung GmbH. The PANDA Collaboration.

[92] W. H. Wong and H. Li. A scintillation detector signal processing technique with active pileup prevention for extending scintillation count rates. *Nuclear Science, IEEE Transactions on*, 45(3):838–842, 1998.

[93] C. L. Woody, P. W. Levy, and J. A. Kierstead. Slow component suppression and radiation damage in doped BaF_2 crystals. *Nuclear Science, IEEE Transactions on*, 36(1):536–542, 1989.

Czech Technical University in Prague
Faculty of Electrical Engineering

Department of Control Engineering

DIPLOMA THESIS ASSIGNMENT

Student: **Bc. Marek Hudec**

Study programme: Cybernetics and Robotics
Specialisation: Systems and Control

Title of Diploma Thesis: **Spectroscopic High Gamma Dose Rate Detector**

Guidelines:

1. Explore and compare current techniques and materials used for gamma-ray detection in the energy range of 30 keV to 3 MeV. Focus on detection principles that allow measurement of high dose rates.
2. Choose the most suitable spectroscopic detector for environmental radiation monitoring with the following aspects: its ability to measure high fluxes (preferably dose rates H*(10) up to 1 Sv/h), long-term stability (>10 years), temperature range of -40 to 60 °C, acceptable energy resolution (spectrum not worse than that of NaI(Tl)), low consumption, mechanical stability, no cooling, maintenance-free.
3. Design and set up a measurement system including a mechanical and electrical layout and conduct measurements of it based on the requirements: temperature tests, intrinsic background measurement, radiation tests at different fluxes and energies, mechanical tests.
4. Analyze and discuss the solution and its readiness for deployment in long-term environmental monitoring.

Bibliography/Sources:

[1] J. Gerndt, Detektory ionizujícího záření, ČVUT, 2011, ISBN 978-80-01-04710-1
[2] J.Šeda, Dozimetrie ionizujícího záření, SNTL, 1983
[3] G. F. Knoll, Radiation Detection and Measurement 4th Edition, Wiley, 2010

Diploma Thesis Supervisor: doc.Ing. Antonín Platil, Ph.D.

Valid until the summer semester 2015/2016

L.S.

Prof. Ing. Michael Šebek, DrSc.
Head of Department

prof. Ing. Pavel Ripka, CSc.
Dean

Prague, December 4, 2014